Fracture Mechanics Based Fatigue and Fracture Toughness Evaluation of SLM Ti-6Al-4V

Nur Mohamed Dhansay

This thesis is submitted for the degree of Master of Science

In the Department of Mechanical Engineering

University of Cape Town

May 2015

Plagiarism Declaration

1. I know that plagiarism is wrong. Plagiarism is to use another's work and pretend that it is one's own.
2. Each significant contribution to, and quotation in, this assignment from the work(s) of the people has been attributed, and has been cited and referenced.
3. This assignment is my own work.
4. I have not allowed, and will not allow anyone to copy my work with the intention of passing it off as his or her own work.

Nur Mohamed Dhansay

Student Number

Date

Abstract

The focus of this research project was to determine experimentally the fatigue and fracture toughness characteristic, from a fracture mechanics perspective, of Ti-6Al-4V titanium alloy manufactured by Selective Laser Melting (SLM). Three build orientations are considered where a fatigue crack is grown parallel and two are grown perpendicular to the build orientation. The project then endeavours to generate a fracture mechanics based Paris equation from the fatigue crack growth rate results and together with the fracture toughness, fatigue life predictions may be determined based on crack propagation lifetimes.

SLM is an Additive Manufacturing (AM) technique whereby an object is fabricated in a layerwise manner via the use of lasers, directly from a 3D CAD model. This process allows for the manufacture of complex designs in its net or near net shape form, which is not possible with conventional manufacturing techniques. There are minimal amounts of material wastage and it potentially eliminates post manufacture machining and processing costs. Ti-6Al-4V is used in many applications where high strength at low density is required at moderate temperatures. Corrosion resistance qualities of the alloy are also considered for many applications. Some of the applications where this alloy is used include turbine engine components, aircraft structural components, aerospace fasteners, high-performance automotive parts, marine applications, medical implant devices and sports equipment. Due to the large use of the alloy in industry and with the potential benefits of manufacturing by SLM, there is a great need for investigating SLM Ti-6Al-4V as a viable alternative to conventional casting, forging and machining.

There is limited literature covering the fatigue crack growth rate and fracture toughness of SLM Ti-6Al-4V and the effect of build orientation on these characteristics. However, it is clear, from the limited available literature that fatigue crack growth rate behaviour is affected by build orientation, and so this project investigates the effect of these orientations, and aims to contribute to understanding why these orientation effects occur. Since there is even less literature available on the fracture toughness of SLM Ti-6Al-4V with respect to build orientation, this project also endeavours to characterise orientation effects on fracture toughness, if any, and compares these with those of conventionally manufacture Ti-6Al-4V.

The fatigue crack growth rate and fracture toughness testing both made use of compact tension specimens. Tests were conducted on flat (crack growth perpendicular to build orientation), vertical (crack growth parallel to build direction), and edge (crack growth perpendicular to build orientation) orientated specimens. Testing of the specimens conformed to the procedures listed in the ASTM E647 and E399 standards for fatigue crack growth rate and fracture toughness testing respectively. These specimens required some limited post machining and post heat-treatment to alleviate the residual stresses which presents itself in the material due to the manufacturing process. A duplex anneal heat treatment was used where the specimen is treated at 950°C for an hour, air cooled and then treated at 700°C for 2 hours followed by air cooling.

The fatigue crack growth rate behaviour of SLM Ti-6Al-4V which has undergone a duplex anneal heat treatment behaves similar to that of wrought Ti-6Al-4V. A noticeable variation in crack growth rate behaviour is observed with the various build orientations in which the Flat orientated specimen exhibits the most stable crack growth behaviour of the orientations. The fracture toughness behaviour of SLM Ti-6Al-4V lies within the range of wrought material as well, but not in the same manner as the fatigue crack growth rate specimens. The SLM duplex annealed Ti-6Al-4V has an approximately 32% greater fracture toughness than wrought recrystallization annealed Ti-6Al-4V and approximately 16% inferior fracture toughness than the wrought β-anneal Ti-6Al-4V. Furthermore, the fracture toughness results did not show any significant amount of variation as a function of build orientation, in contrast to the fatigue crack growth rate behaviour.

The fracture mechanics parameters of fatigue behaviour (Paris curve) and fracture toughness show strong correlation between SLM manufactured and conventional Ti-6Al-4V. It is thus reasonable for the alloy to be produced using the SLM process as their properties are entirely acceptable, if the material is free from defects, and residual stress.

Acknowledgements

All praise belongs to Allah, the Lord of the worlds. The Most gracious, The Most Merciful.

The Author would like to thank the individuals who have helped him along with this MSc dissertation. A special mention needs to be made of the following groups and people:

- To the authors parents: Dawood and Nurjehan Dhansay for their support and understanding;
- To Professor Robert Tait for the support, guidance and assistance for the successful completion of the project;
- To Dr Thorsten Becker for the support, guidance and assistance for the successful completion of the project;
- To Dr Glen Snedden from CSIR for the financial support
- To the authors friends, particularly Victoria Cain for her advice and willingness to help out;
- To the CME staff
- To the workshop staff for helping out with the post manufacture machining of specimens

The author would also like to thank the staff of the Mechanical Engineering Department at UCT with the facilitating of this project.

Dedication

In the name of Allah, The Most Gracious, The Most Merciful:

"Recite in the name of your Lord who created. Created man from a clinging substance. Recite, and your lord is the most Generous. Who taught by the pen. Taught man that which he knew not."
[Quran 96:1-5]

"The Prophet Muhammad (peace be upon him) said: "God, His angels and all those in Heavens and on Earth, even ants in their hills and fish in the water, call down blessings on those who instruct others in beneficial knowledge."
[Al-Tirmidhi, Hadith 422]

The Prophet Muhammad (peace be upon him) said: "If anyone travels on a road in search of knowledge, God will cause him to travel on one of the roads of Paradise. The angels will lower their wings in their great pleasure with one who seeks knowledge. The inhabitants of the heavens and the Earth and (even) the fish in the deep waters will ask forgiveness for the learned man. The superiority of the learned over the devout is like that of the moon, on the night when it is full, over the rest of the stars. The learned are the heirs of the Prophets, and the Prophets leave (no monetary inheritance), they leave only knowledge, and he who takes it takes an abundant portion.
[Sunan of Abu-Dawood, Hadith 1631]

Table of Contents

List of Figures

List of Tables

Nomenclature

a	nominal crack length
a_i	Initial crack length
a_{crit}	Critical crack length
b	Uncracked length of specimen
B	Specimen thickness
C	y-intercept of Paris curve
E	Youngs modulus of elasticity
K	Stress intensity
K_{IC}	Plane strain fracture toughness
M	slope of Paris curve
N	Number of cycles
P	Applied load
P_{max}	Maximum fatigue load
P_{min}	Minimum fatigue load
R	Fatigue force ratio
SLM	Selective Laser Melting
UTS	Ultimate tensile strength
W	Effective width
Y	Compliance factor
ΔK	Cyclic stress intensity
ΔK_{th}	Threshold stress intensity
$\Delta\sigma$	Difference in maximum and minimum stress
σ	Stress
σ_y	yield strength

Chapter 1 – Introduction

This thesis concerns an investigation into the fatigue crack growth rate behaviour and fracture toughness performance of Selective Laser Melted Ti-6Al-4V titanium alloy with respect to three build orientations. This project then endeavours to generate a fracture mechanics based Paris equation from the fatigue crack growth rate results and combined with the fracture toughness, fatigue life predictions may be determined based on crack propagation, for particular levels of cyclic stresses.

Selective Laser Melting (SLM) is an additive manufacturing (AM) technique whereby parts are produced in a layerwise fashion, consolidated via lasers, directly from a 3D CAD model. This allows for designs to be produced to net shape or near net shape, requiring minimal amounts of post manufacture machining. The attraction of SLM lies in its capability of producing complex design shapes which are not possible with conventional manufacturing techniques. In addition there is minimal amounts of material wastage, which potentially eliminates post manufacture machining and reduces processing costs. Industries such as the aerospace, automotive and biomedical, amongst others, stand to benefit greatly as the titanium alloy, Ti-6Al-4V, is a largely used alloy in these industries, as well as many others. With the potential benefits of manufacturing by SLM, there is a great need to investigate SLM Ti-6Al-4V's physical properties as a viable alternative to conventional casting, forging and machining.

This research is a continuation of earlier work conducted by Knowles [1], where residual stress measurement and relief was conducted in order to obtain optimised heat treatments. The optimised heat treatments would produce a stress free or near stress free SLM Ti-6Al-4V product so that "the generation of thermal residual stresses may not be a substantial impediment to the successful implementation of this technique" [1]. The available literature does not cover the fatigue crack growth rate of SLM Ti-6Al-4V and the effect of build orientation extensively. However, it is clear from the available literature that fatigue crack growth rate behaviour is affected by build orientation. This project then investigates these orientations, one of which has not been investigated before, and aims to contribute to the understanding of why these orientation effects occur. Furthermore, there is even less literature which neither investigates the fracture toughness of SLM Ti-6Al-4V which has not been stress relieved nor is the build orientation specified. Thus this project tries to fill certain gaps within literature which is required in order for SLM products, particularly SLM Ti-6Al-4V in this case, to become eventually a viable alternative to conventional manufacturing within certain industries for specific applications.

The investigation of this project has taken place at the Centre for Materials Engineering laboratory at University of Cape Town in South Africa. The titanium alloy, SLM Ti-6Al-4V, was obtained from the Centre for Rapid Prototyping and Manufacturing at the Central University of Technology situated in Bloemfontein South Africa. The project has spanned over the last two years in which a Master of Science student in Materials Engineering conducted experimentations, explained in detail in this thesis, using testing equipment and systems provided by the Centre for Materials Engineering.

1.1 Prototyping to Manufacturing

Over the history of AM, most of the AM technologies have largely been used for the production of conceptual and functional prototypes, also known as Rapid Prototyping (RP), due to the shortened production development steps [2]. With advances in RP technologies and improved quality of printed products, there has been a recent growth in the manufacturing of end-use parts (AM) [2], [3]. A variety of applications in many different industries stand to benefit from AM production over existing methods of production. Production by AM have many benefits such as [4]:

- No tooling is required – reducing production time and expense
- Low volume productions are feasible and economical
- Possibility to change design quickly
- Product optimization for function
- Economical custom products
- Simpler supply chains – Shorter lead times, lower inventory
- Design customization

One such example is the aerospace industry that uses a buy-to-fly ratio which describes the cost of raw material required to produce a finished part. Certain titanium aerospace parts are machined down from a solid billet, removing up to 90% of the raw material which has no further use on the aircraft [3]. AM would only use the required amount of material to produce the part and in that way drastically improve the buy-to-fly ratio.

The capability of custom and complex designs allows for improved functionality and optimization. Smooth internal pathways for hydraulic oil in a gearbox, for example, can now be printed rather than drilled out leaving 90° bends [3]. The SLM manufactured gearbox facilitates faster gear changes as well as decreasing the gearbox weight [3].

With a list of benefits for producing parts via AM, many industries stand to benefit over the existing methods of production. Due to these benefits and the interest from industry, a large effort is focussed on researching the products of AM as a viable option to conventional manufacturing methods. Although there are many benefits to manufacturing via SLM, drawbacks of this process include large thermal stresses, porosities, unfused powder particles and impurities in the build chamber amongst others. All of these lead to deterioration of the mechanical properties of the material by acting as stress raisers and areas of weakness. It is research projects such as these, which focus on common engineering material produced by AM techniques, that investigate the mechanical properties, which will lead to improved performances. In addition, it is hoped an enhanced understanding will lead to improved microstructure and reduce deficiencies so that eventually AM products may be used for end-use parts in industry.

A recent study on fatigue crack growth rate with respect to two build orientations of SLM Ti-6Al-4V shows that with sufficient stress relieving heat treatment, SLM Ti-6Al-4V behaves similarly to conventionally manufactured Ti-6Al-4V [5]. The build orientation aspect of the study was not adequately addressed and so further investigation into the build orientation effects on fatigue crack growth rate behaviour as well as an extra build orientation is required for a deeper understanding of this behaviour. This being said, there are many parameters when dealing with manufacturing by SLM, and so orientation effects may arise from a combination of reasons. Work carried out on conducting fracture toughness testing was in the as-built condition and proved to have inferior fracture toughness properties to that of conventionally manufactured Ti-6Al-4V [6]. This is not a true reflection of the fracture toughness properties of SLM Ti-6Al-4V as it has not been stress relieved adequately and so investigation of the fracture toughness of SLM Ti-6Al-4V in a stress relieved condition is required. Furthermore, since there is anisotropic behaviour observed in the fatigue crack growth rate behaviour [7], it is in order to ask if this behaviour extend to the fracture toughness behaviour. Generally, conventionally manufactured Ti-6Al-4V can be divided into wrought and cast material where cast material is used for applications in which higher ultimate tensile strength and yield strength are required [8]. Although Leuders et al [5] mention that SLM Ti-6Al-4V, when stress relieved, behaves similarly to conventionally manufactured Ti-6Al-4V, they do not explicitly mention which conventional manufacturing method the SLM Ti-6Al-4V comparison is being made to. This may limit the use of SLM Ti-6Al-4V in industry depending on which manufacturing method it is similar to. It is believed that further investigation into these points will provide insight on whether or not SLM Ti-6Al-4V will be recognised as a viable alternative for conventional manufacturing purposes.

1.2 Additive Manufacturing in South Africa

In 1991, approximately 10 years after the international communities had started its activities in additive manufacturing, South Africa had obtained its first AM system owned by a private company which was followed by the Council for Scientific and Industrial Research (CSIR) obtaining two Stratasys FDM 1500 systems in 1994 [9]. By 1998, seven machines were available in South Africa which were separately owned by CSIR and the Central University of Technology (CUT) [9].

By 1999, the Rapid Product Development Association of South Africa (RAPDASA) was formed as a representative association for those involved in rapid product development (RPD) in research organizations as well as industrial companies [9]. Aimed at encouraging the development and use of RPD technologies in South Africa, RAPDASA started an annual conference in 2000 for researchers and practitioners to share their research and benefit from international world of RPP [9]. These annual conferences have proven to be beneficial towards the RPD within South Africa as networking, international collaborative projects and partnerships have all stemmed from the RAPDASA conferences [9].

Terry Wohlers [10] forecasted that 2003 would be the year 3D printers would have a large growth spurt, which held true for South Africa as 35% of local installed systems were 3D printers [9]. By 2006, there were 90 installed systems in South Africa with a continuous positive growth, particularly in recent years due to the availability of lower cost machines which had increased [9]. An article compiled by Campell, De Beer and Pei [11] whose analysis goes up to 2008 shows that 48% of all South African universities have AM facilities in which research is being pursued.

Although having a late start, a large amount of knowledge was available to South Africa through international studies, vendor's literature etc. which quickly helped identify relevant AM application areas [9]. Initial acquisitions came from industrial investments and Technology and Human Resources for Industry Programme (THRIP) and later as applications were proven, more systems were purchased with university, National Research Foundation (NRF) funding and by relevant industries [9]. Due to the nature of AM, a great amount of support has been given to the South African industry and academia. It was RAPDASA and relevant funding institutions i.e. CSIR, NRF, and THRIP etc. which have played an instrumental role in what may possibly become one of the biggest industrial revolutions on the African continent [9].

1.3 Objectives

The objectives of the research are:

- To perform and evaluate fatigue crack growth rate testing on SLM Ti-6Al-4V with respect to build orientation of specimens that have undergone a sufficient stress relieving heat treatment (so that residual manufacturing stresses are close to zero).
- To perform and evaluate fracture toughness testing on SLM Ti-6Al-4V with respect to build orientation of specimens that have undergone a sufficient stress relieving heat treatment.
- To highlight any differences in fatigue crack growth rate and fracture toughness behaviour due to build orientation, and attempt to correlate it with microstructure.
- To compare the fatigue crack growth rate and fracture toughness results of SLM Ti-6Al-4V with that of conventionally manufactured Ti-6Al-4V.

This will bring the research focused on additive manufacturing ever closer to becoming a viable option to conventional manufactured material.

1.4 Details of Thesis Format

The thesis proceeds in an orderly fashion, starting with the background literature relevant to this research project in Chapter 2. It briefly describes the properties of titanium which lead into the specific titanium alloy, Ti-6Al-4V. The chapter also includes a history of AM and a few of the technologies available today. The analysis method of fracture mechanics used in this project is also elaborated.

Previous studies on SLM Ti-6Al-4V specific to fatigue crack growth rate and fracture toughness are analysed in Chapter 3. This also includes the work of Knowles [1] on residual stress measurement and relieving.

Chapter 4 introduces the experimental procedures of the project and the equipment used to obtain results. These include the fatigue crack growth rate testing and fracture toughness testing. The chapter also includes the methods used to obtain specimen density and some microscopy work.

The results obtained from all experimentation are presented in Chapter 5 and information that may be drawn from the results is discussed in Chapter 6. The project is finally concluded in Chapter 7.

Chapter 2 – Background

This chapter aims to describe the information that relates to this project with the aim to lay the foundation for the understanding of this dissertation. A brief introduction on titanium alloys is given which is followed by information on the alloy used in this project i.e. Ti-6Al-4V. The chapter also introduces additive manufacturing along with a historical perspective on its developments. The necessary background knowledge to fracture mechanics is introduced and elaborates on the LEFM methods used for analysing experimental data which will be required for further reading of this dissertation.

2.1 Titanium

Titanium ranks as the 9th most abundant element and the 4th most abundant structural metal, exceeded by aluminium, iron and magnesium [12]. The problem faced with titanium is that it is seldom found in high concentrations and never in a pure state which leads to the high costs of the metal. The DuPont company was the first to produce titanium commercially in 1948 [12].

2.1.1 A Brief History

The discovery of titanium dates as far back as 1791, where a British mineralogist, William Gregor, examined magnetic sand from the local river. The sand had its iron content removed and was then treated with hydrochloric acid to be left with an impure oxide of the new element, titanium oxide [12].

An independent Berlin chemist, Martin Heinrich Klaproth, had also isolated titanium oxide four years later from a Hungarian mineral. Klaproth looked at Greek mythology to provide the name Titanium. Titans were detained in captivity by their father in the earth’s crust, similar to the hard extract ore and hence the name Titanium [12].

Over a century later, in 1910, Mathew Albert was able to isolate the metal by heating titanium tetrachloride ($TiCl_4$) with sodium in a steel bomb. It was only in 1932 when the “father of the titanium industry”, Wilhem Justin Kroll, produced significant quantities of titanium by combining $TiCl_4$ with calcium. Kroll demonstrated that if the reducing agent is changed from calcium to magnesium which is used to reduce $TiCl_4$, titanium could be extracted commercially. This method is still the most used method of extracting titanium and is known as “Kroll process” [12].

2.1.2 Properties

The advantage of using titanium is that it has a high strength-to-weight ratio. This allows for titanium to be used in industries such as the aerospace industry where it can be used over other heavier metals such as steels [13]. A great portion of its application has come in military use (aircraft and turbine engines) whereas in recent years, many types of sporting equipment have also been added to its list of applications [8].

Titanium offers many significant properties which are the basis for its widespread use.
Properties such as [8]:

- Low density
- Alloying of the metal to improve tensile strength
- Cost is comparable to that of super alloys
- Exceptionally corrosion resistant (biomedically as well)
- May be forged, wrought or cast
- Available in a wide variety of types and forms

Furthermore, titanium is biologically compatible with the human body and has inherent applications in the biomedical industry. Despite the favourable properties of titanium and its alloys, due to the high costs involved in the process of obtaining titanium in its pure state, titanium materials are often limited to applications where high performance is required [14].

2.1.3 Structure

Titanium has two elemental crystal structures, where each structure is only stable within certain temperature ranges [12][8]. The ability of transforming from one crystal structure to another is called allotropic transformation with the corresponding temperature being called the transus temperature [12]. The common terms used for the crystal structures are known as alpha and beta phase, where alpha refers to hexagonal close packed (HCP) and beta refers to body centred cubic (BCC). This can be seen in Figure 2-1 below. Titanium undergoes the allotropic phase transformation from HCP (α phase) to BCC (β phase) at 882.5°C [15]. This temperature is strongly influenced by the purity of the metal (presence of interstitial and substitutional elements) [15].

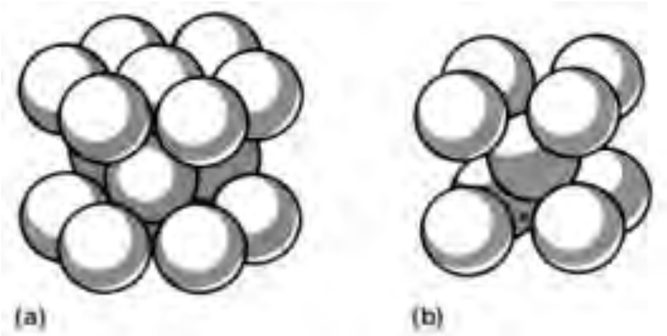

Figure 2-1: Appearance of crystal structures of titanium at the atomic level. (a) Hexagonal close packed. (b) Body centred cubic [8]

The generally accepted categories for titanium alloys are α, α+β, β [12] [15].Alloying elements which increase the β-transus temperature are known as α-stabilizers, while β-stabilizers reduce the β-transus temperature [12]. The α and β-stabilizers have different effects on certain properties of titanium, as can be seen in Figure 2-2.

An α-stabilizer typically used is aluminium, which contributes to oxidation resistance at high temperatures. The mechanical properties of titanium α-alloys generally cannot be improved by heat treatments as the alloy is in a single phase, however, heat treatments which alter grain size may influence the mechanical properties. β-alloys have high strength due to the BCC structure of the β-phase as well as greater formability compared to that of the HCP structured alloys [8].

Adding certain amounts of specific β-alloys to α-alloys, allows for the resultant alloy to be heat treated in a temperature range where the alloy is categorised as α+β (two phase). This allows for structure refinement and by permitting some β-phase to be retained at lower temperatures, enables optimum control of the microstructure during transformations. The α+β alloy have an excellent combination of strength and ductility and are stronger than both α and β alloys [8].

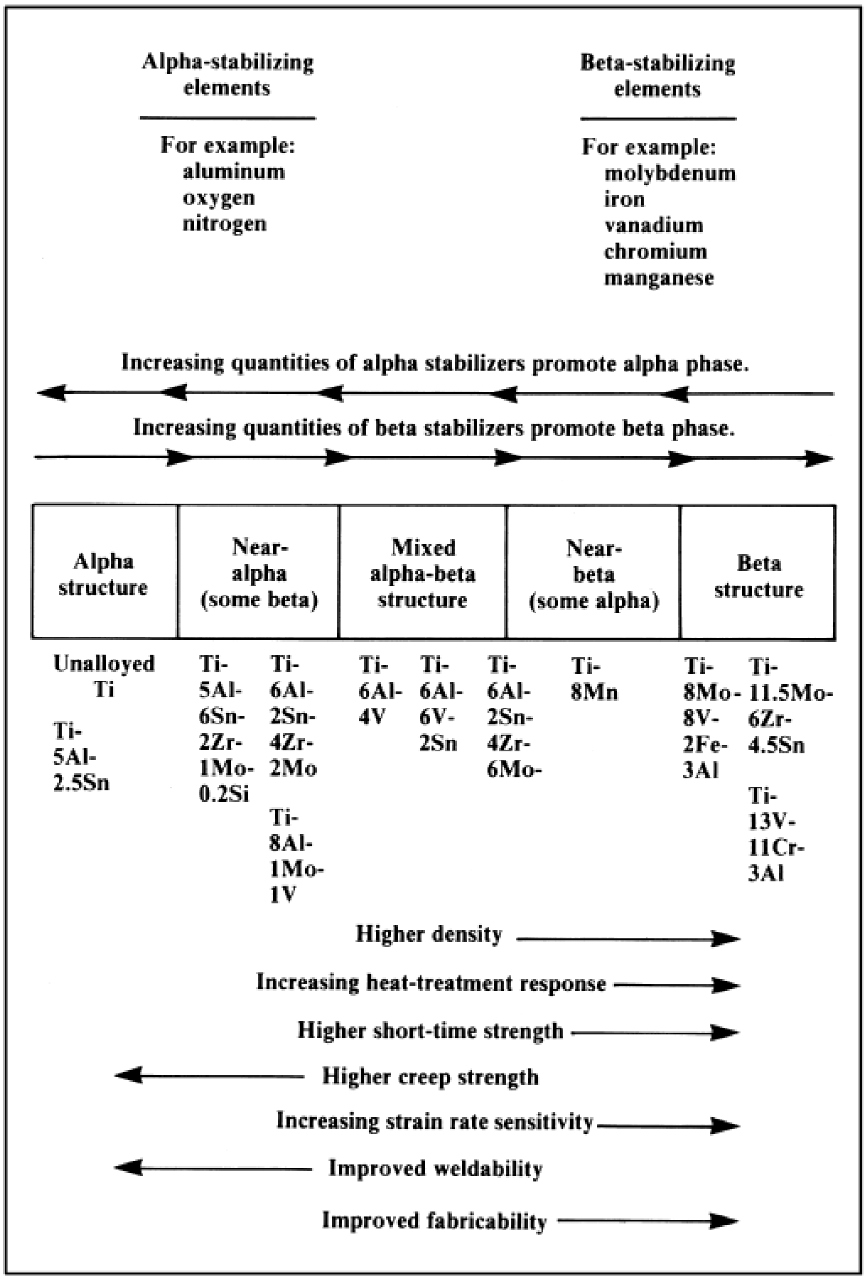

Figure 2-2: Schematic showing effects of alloying elements on structure and some selected properties. [8]

2.2 Ti-6Al-4V

Ti-6Al-4V is the most widely used titanium alloy and accounts for approximately 45% of the worlds shipped titanium alloys [13], [8]. It has replaced heavier, less serviceable and less cost effective material and has the best all round performance for many engineering applications [16]. This particular alloy is classified as an α+β alloy and is used in many significant industries such as the aerospace, biomedical, automotive and marine industries amongst many others. This section reviews Ti-6Al-4V with respect to its microstructure, conventional manufacturing processes and industrial applications. The chemical composition and mechanical properties of Ti-6Al-4V are given in Table 2-1and Table 2-2.

Table 2-1: Chemical composition if Ti-6Al-4V [16]

	Ti-6Al-4V (Typical)	**Ti-6Al-4V (Cast Material)**	**Ti-6Al-4V (Wrought Material)**
Aluminium	6%	5.5-6.75%	5.5-6.75%
Vanadium	4%	3.5-4.5%	3.5-4.5%
Carbon	0.03%	< 0.1%	< 0.08%
Iron	0.1%	< 0.3%	< 0.3%
Oxygen	0.15%	< 0.2%	< 0.2%
Nitrogen	0.01%	< 0.05%	< 0.05%
Hydrogen	0.003%	< 0.015%	< 0.015%
Titanium	Balance	Balance	Balance

Table 2-2: Mechanical properties of Ti-6Al-4V [16]

	Ti-6Al-4V **(Typical)**	**Ti-6Al-4V** **(Cast Material)**	**Ti-6Al-4V** **(Wrought Material)**
Yield Strength	950 MPa	758 MPa	860 MPa
Ultimate Tensile Strength	1020 MPa	860 MPa	930 MPa
Elongation	14%	> 8%	> 10%
Reduction of Area	40%	> 14%	> 25%

The variations in properties shown in Table 2-2 are for illustration purposes, where properties may vary significantly depending on the production method and microstructure. The cast and wrought materials composition and mechanical properties are according to the ASTM F1108 (cast material) and ASTM F1472 (wrought material) respectively.

2.2.1 Microscopy

There are three distinct microstructures in the α+β alloys which can be obtained by various heat treatment methods [17]. These structures are: fully lamellar, fully equiaxed and bi-modal as shown from left to right respectively in Figure 2-3.

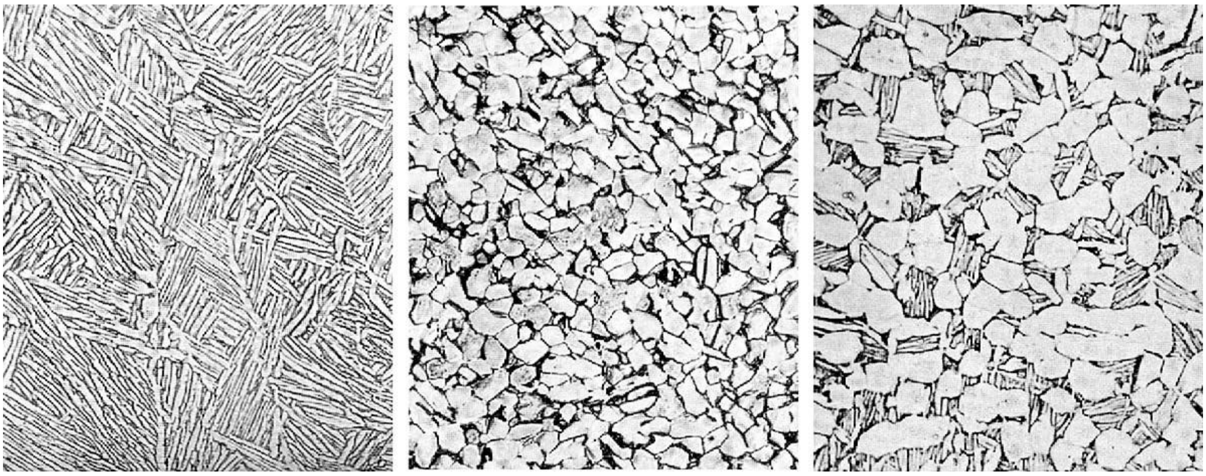

Figure 2-3: Three distinct microstructures of Ti-6Al-4V [18]

Since Ti-6Al-4V has these distinctly different microstructures, it shows that the alloy is sensitive to heat treatments which allows for property manipulation. This is due to the

Vanadium content (β-stabiliser) which facilitates heat treatment capabilities. Being an α+β alloy, phase diagrams have been developed to help understand the quantitative relationship between the phases, this is illustrated in Figure 2-4.

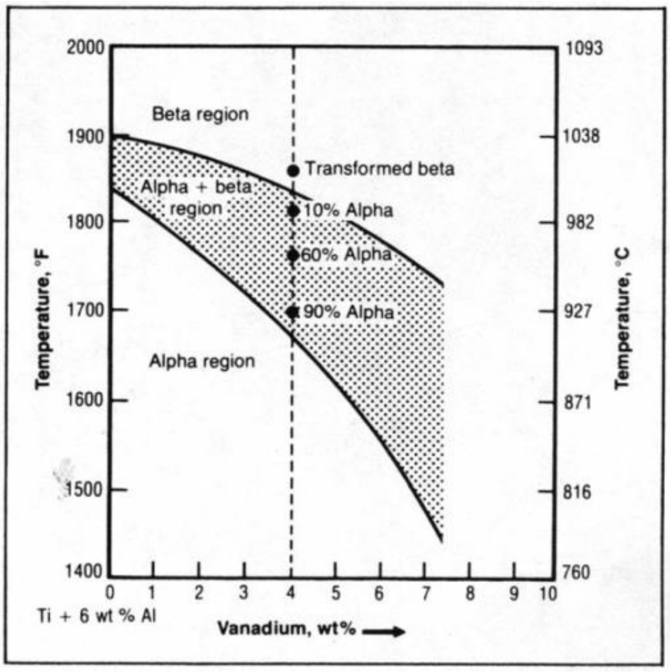

Figure 2-4: Phase Diagram of Ti-6Al and V [19]

Fully Lamellar

Fully lamellar structures have a weave-like pattern and are often referred to as a basket-weave structure. The structure can be coarse or fine with greater amounts of α phase than β phase within the boundaries. The microstructure is obtained through an annealing treatment within the β phase region, usually kept between 30-50°C above the β transus temperature to maintain control over grain size and an aging process between 700-800°C [17], [18]. The most significant effect on the microstructure is the cooling rates as this determines the size of α lamellae, the α colony size and the thickness of α layers at the β grain boundaries [17]. The effect of cooling rates can be seen in Figure 2-5

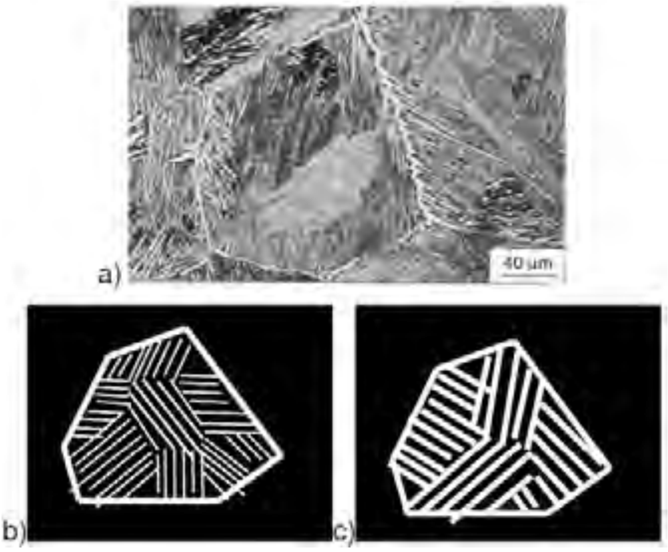

Figure 2-5: Common α-β microstructure exhibiting α-lamella in β-matrix, b) Diagram of increased cooling rate with finer and shorter α-lamella, c) Diagram of decreased cooling rate with longer thicker α-lamella [20]

Fully lamellar structures obtained from above the β transus temperature results in higher fracture toughness and resistance to stress corrosion [8]. This structure does however result in a great loss in ductility and strength [17]. To obtain an optimised balance between ductility, fracture toughness, creep and stress rupture resistance, it is usually solution treated below the β transus [8].

Fully Equiaxed

Fully equiaxed structures contain crystals which have their α phase axes approximately the same length. The equiaxed α is surrounded by β phase at grain boundary “triple points”, seen in Figure 2-6. This structure requires a lamellar “starting” structure with an important recrystallization annealing process below the β transus which determines the volume fraction of equiaxed primary α surrounded by retained β phase [17]. Annealing temperatures and cooling rates also affect the equiaxed structures similarly to the lamellar structures. The fully equiaxed structure results in high strength and ductility, but with relatively low fracture toughness.

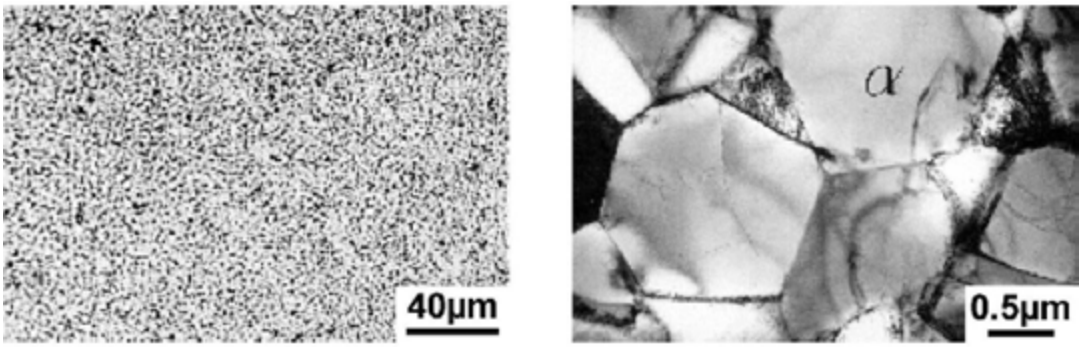

Figure 2-6: Fine grained, fully equiaxed microstructure [17]

Bi-Modal

Bi-modal structures contain equiaxed primary α phase grains with a colony type lamellar matrix of alternating α and β plates (basket-weaves) within small β phase grains [21]. This is illustrated in Figure 2-7. These structures require a recrystallization anneal in the high α+β phase, approximately between 900-950°C, with an air cooling and aging below 700°C [18],[21]. The annealing temperatures determine the volume fraction of primary α phase and the β grain size while the cooling rates determine the width of the α lamellar [17]. This structure may result in higher strength and ductility compared to the previous two structures [17].

Figure 2-7: Bi-modal microstructure recrystallized at 950°C [17]

2.2.2 Conventional Production

The relatively high cost involved in obtaining titanium before it is manufactured into a component is a driving force to produce titanium components using a near-net-shape forming method [12]. Forming methods play a role in the microstructure and properties of the alloy, therefore a cost optimized processing route is carefully selected for the product to be placed into its final shape [12]. This section covers wrought (forging/milling from ingots), casting and powder metallurgy production methods.

Wrought

Wrought titanium alloy accounts for 70% of the titanium alloy market [22]. Since the alloy is forged or milled into a final product, it has to initially undergo a few melt cycles to increase purity [8], [22]. Factors which are considered to be critical in the manufacture of wrought titanium alloys include: alloying, the melting process used in ingot processing, mechanical working history, heat treatment temperatures and cooling rates, and aging temperature [22]. Wrought titanium alloys, including Ti-6Al-4V, are largely forged into simple shapes, such as sheets and plates used in the aerospace industry [8]. Forging makes use of dies to produce a shape in which there are two main approaches: forging above and forging below the β transus temperature [8]. The mill and forging processes are described by the flow chart in Figure 2-8. Wrought products have the advantage of being thermomechanically treated into a final shape to produce desired properties compared to the limited tailoring of properties associated with casting and powder metallurgy [22].

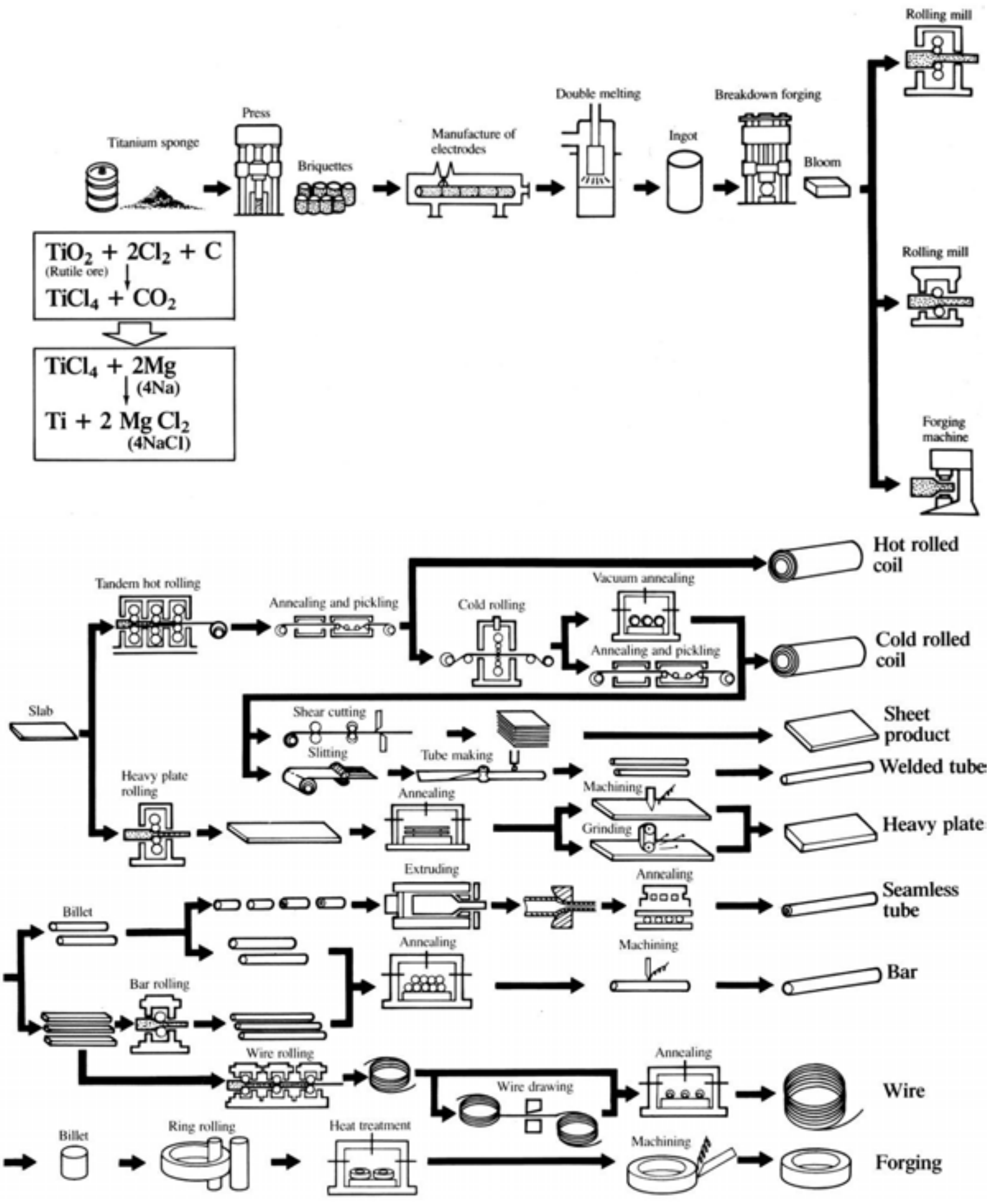

Figure 2-8: Flow chart of mill products and final wrought forms [8]

Castings

Casting is a fabrication method in which molten metal is poured into a mould to produce a desired near-net-shape component. Due to the near-net-shape capabilities, cast products can be of complex shapes, require low amounts of post machining and therefore offers cost saving potential when fabricating titanium alloys under such methods [12]. Ti-6Al-4V is the dominant titanium alloy produced by casting methods which is mainly used for aerospace and marine applications [8]. Approximately 90% of all cast titanium is Ti-6Al-4V where the remaining 10% is mostly commercially pure titanium [8]. The challenge with casting titanium products is that at elevated temperatures, it becomes highly reactive to atmosphere and the casting mould which deteriorates mechanical properties [12], [8]. Due to these challenges, castings take place in a vacuum and a water-cooled crucible is usually used [12]. Of the different forms of casting, investment casting allows for close tolerances, thinner walls, smaller draft angles and better surface finishes [12]. If the cast has very thin walls, centrifugal casting is required to fill the mould [12]. Figure 2-9 describes the investment casting process. This is of interest in the aerospace industry where thin and complex shapes are required. The advantage of casting over wrought is cost savings, reduced lead time to component delivery and the ability of produce near-net-shapes [8]. There is, however, a penalty with casting compared to forged parts with respect to the strength and ductility of a component [12]. Porosity is an inevitable outcome with casting [12]. To reduce this effect and improve mechanical properties, parts are hot isostatically pressed (HIP) at 900°C for 2 hours in argon at a pressure of 105MPa [12], [8].

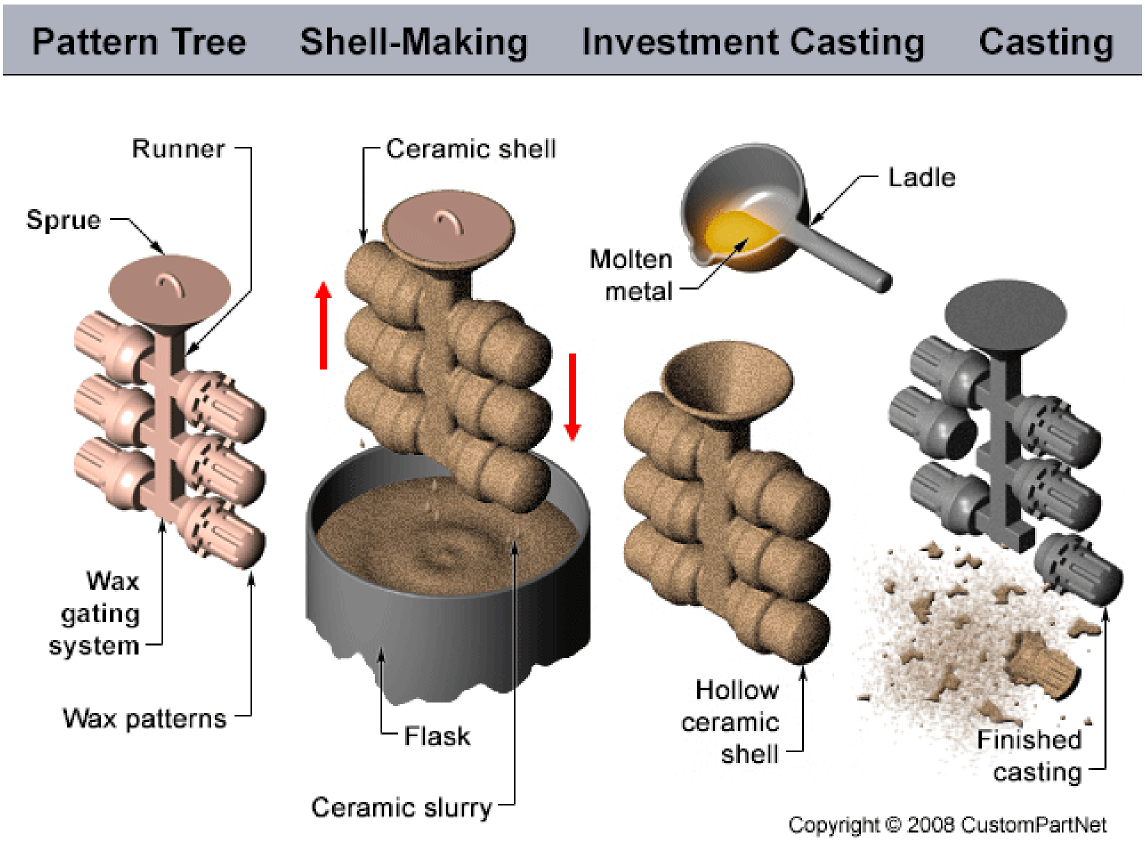

Figure 2-9: Investment casting process [23]

Powder Metallurgy

Powder metallurgy (PM), as with casting, produces near-net-shape components in the drive to reduce the cost of manufacturing titanium parts. Powder metallurgy produces a part by compacting powdered metal. There are several compacting methods such as: Mechanical die pressing (CP) plus vacuum sintering, cold isostatic pressing (CIP) plus vacuum sintering, vacuum hot pressing (VHP), HIP, and CIP plus vacuum sintering plus HIP (CHIP) [8]. Some of these pressing methods, such as HIP, VHP and CHIP are capable of producing fully dense parts [8]. However, it is the HIP process which is the most common method for producing critical parts [8]. A typical process for the consolidation of Ti-6Al-4V is a HIP process conducted between 1-3 hours at approximately 920-970°C at a pressure of about 2000 bar [12]. Generally PM produces parts that are mechanically superior to that of cast and similar to the wrought counterparts [12]. Some of the powder production processes are: rotating-electrode process (REP), plasma rotating-electrode process, hydride/dehydride (HDH) process and gas atomization (GA) process [8]. The GA, REP and PREP methods produces spherical powder which helps with flow and packing density [8].

3.1.3 Application

Ti-6Al-4V is the most commonly used titanium alloy in the market. Initially, the alloy was specifically developed for aerospace applications but in later years non-aerospace application, such as automotive and medical etc., has arisen [12]. There are many benefits offered by titanium alloys which make its use so widespread today [8]. This section will cover industrial applications of Ti-6Al-4V in the aerospace and automotive industry.

Aerospace

Ti-6Al-4V has been largely associated with the aerospace industry over competing metals, due to its excellent strength-to-weight ratio, corrosion resistance, higher yield and fatigue strength [17]. There are various applications for this alloy in the aerospace industry such as airframe skins, structural components and gas turbine engine components [12],[8] ,[17]. However, the larger portion of the alloys application is in the gas turbine engine [12]. Fan blades and disks are used at moderately low temperatures which allows them to be manufactured from Ti-6Al-4V [12]. The limiting temperature for Ti-6Al-4V is approximately 300°C which means the alloy may be used up to the first 5 stages of the low pressure compressor and the front stages of the high pressure compressor [12], [17]. There are large oscillatory stresses experienced by the fan and compressor blades which will cause fatigue damage. The blades undergo a recrystallization to form a bi-modal microstructure which has greater fatigue strength than other microstructures [17].

Figure 2-10 depicts some aircraft components manufactured from Ti-6Al-4V. In non-rotating engine components, Ti-6Al-4V can be used for casings, ducts, frames, stators, manifolds amongst others [17]. Selection criteria for these components look at properties such as stiffness, ratio of yield stress to density, temperature capabilities and resistance to burn [17]. Fatigue is of no real concern, except for when vibrations occur [17].

Figure 2-10: a) Forged Ti-6Al-4V fan blades (larger blade approximately 1m), b) Cast Ti-6Al-4V wing attachment for the F22 military aircraft [17]

Automotive

Since the 1950's, the automotive industry had interests in titanium and its alloys due to the high strength, low weight, elastic energy absorption capacity and excellent corrosion resistance [17]. Due to the high price of titanium and its alloys, the material was used more in motor racing than in commercial use [17]. However, due to demands of safety and efficiency, there was a greater willingness for the implementation of the expensive material for commercial use [17]. Not only is it the cost of the material which may be expensive, but also the cost of component manufacture which needs to be taken into account. Thus Ti-6Al-4V is used more in the high performance vehicles [17]. Figure 2-11 and Table 2-3 lists the potential applications for titanium in automotive production.

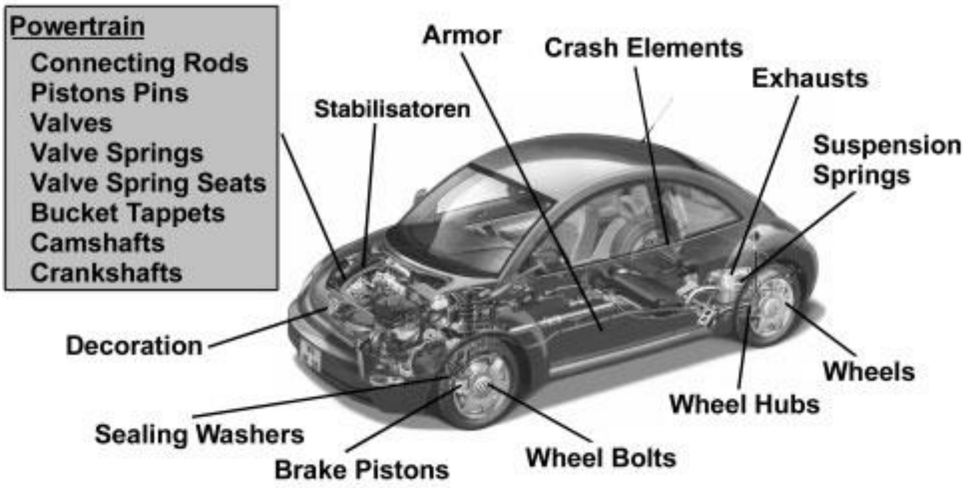

Figure 2-11: Examples of possible automotive applications of titanium[17]

Table 2-3: Standard components manufactured from Ti-6Al-4V[11], [17]**.**

Component	**Manufacturer**	**Model**
Connection rods	Ferrari	All 12-cylinder engines
Wheel rim screws	Porsche	Sport wheel option
Connecting rods	Porsche	GT3
Valves	Toyota	Altezza 6 cylinder engine
Turbo charger wheel	Daimler	Truck diesel
Wheel rim screws	BMW	M-Techn. Option
Wheel rim screws	Volkswagen	Sport package GTI
Valves	Nissan	Infiniti Q45

2.3 Additive Manufacturing

Additive manufacturing is a collection of fabrication techniques whereby an object is produced layer-by-layer, in which material is added rather than commonly subtracted to produce the object [24],[25]. Processes such as selective laser melting/sintering, fused deposition modelling, laminated object manufacturing are all part of the additive manufacturing techniques [24]. The selective laser melting/sintering method uses a layer of powder, typically 20-150µm thick, which is spread over a build-up area where a focused laser beam guided by galvano mirrors melts a selected area which is interpreted from a CAD model [24],[26] .

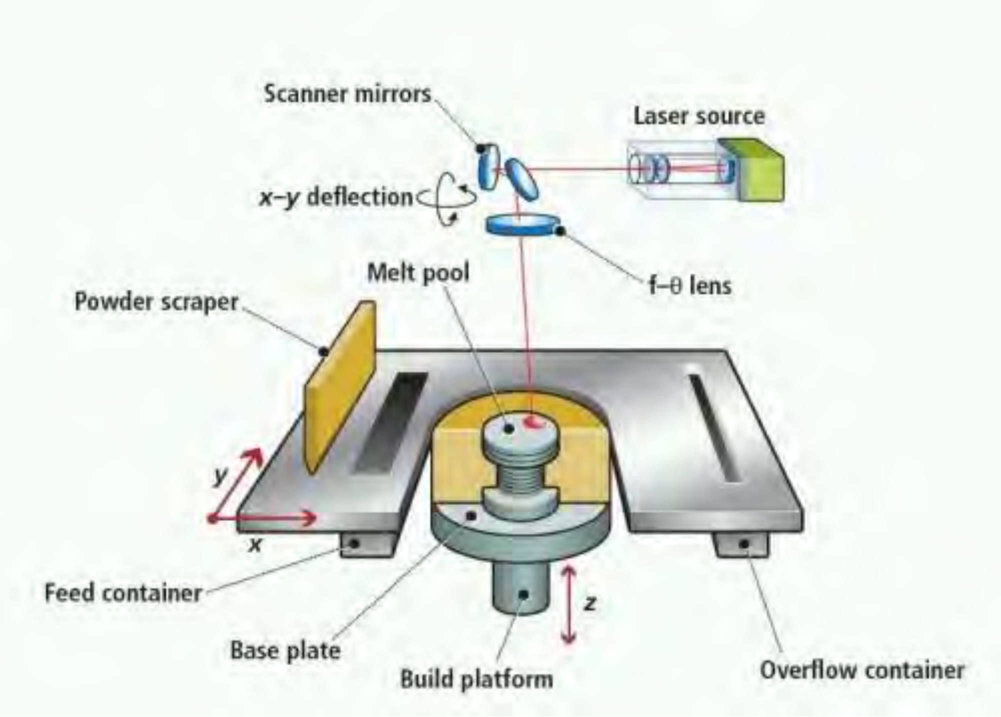

Figure 2-12: Illustration of a typical additive manufacturing process [27].

2.3.1 History

The modern idea of additive manufacturing can be traced back to over 40 years, although earlier topographic and photosculpture techniques which share a great deal in common with additive manufacturing are over 100 years old [28], [29].

Topographical techniques, such as that proposed by Blanther[30] in 1890 whereby topographical contour lines on a series of wax plates are impressed, cut and stacked to produce a mould of a topographical relief map, were of the first processes which may be related to additive manufacturing [28]. This produces both a positive and negative three-dimensional surface, and after smoothing the surfaces, a paper map can be pressed between the two to produce a raised relief map [28], [29]. This is shown in Figure 2-13. Subsequent methods include the use of cardboard and glue by Zang [31], inscribed transparent plates by Gaskin [32] as well as the use of photo hardening material by Matsubara [33], [28], [34]. By 1979, DiMatteo [35] recognized the potential of these methods to fabricate surfaces that are particularly difficult to produce using standard machining operations [28].

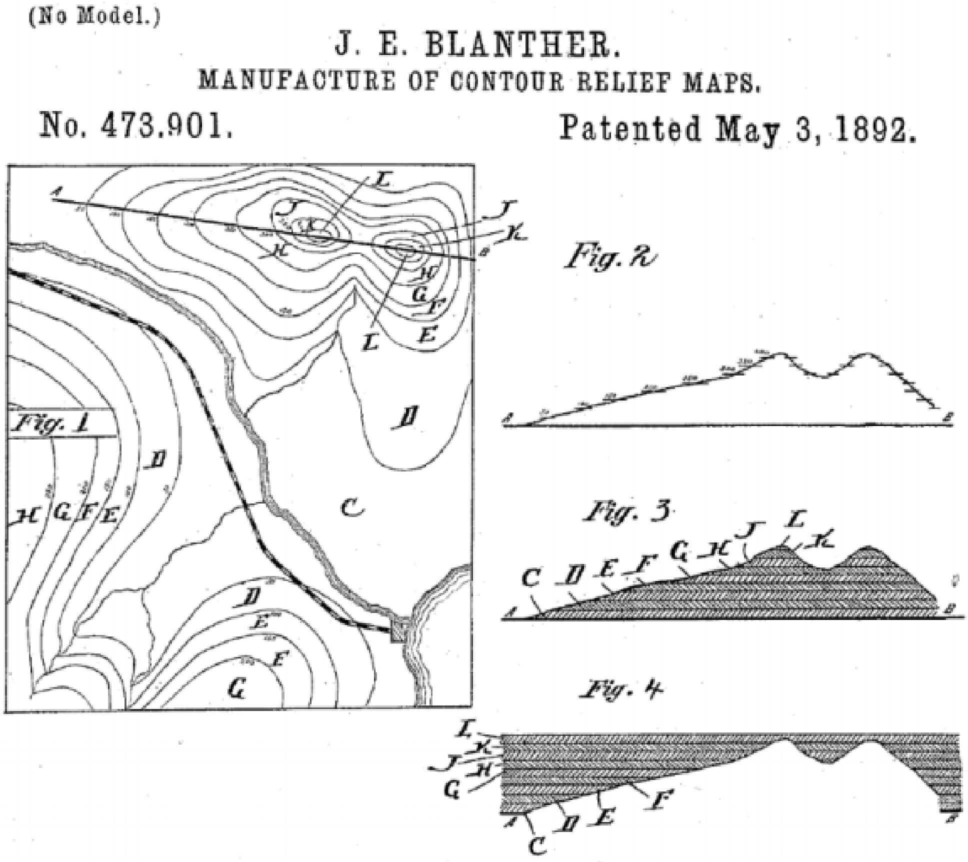

Figure 2-13: Blanther's patent of topographical contour relief map [30]

Photosculpture techniques were developed in the 19th century in an attempt to produce three-dimensional replicas of any object, even that of the human form [28],[34]. Frenchman Francois Willème [36], designed such a technology where a subject or object was placed in a circular room, photographed by 24 equally spaced cameras simultaneously [28], [34]. A scaled down replica was then carved by an artisan using the silhouette of each photograph [28], [34]. To alleviate the tedious work of the artisan, Baese [37] described a technique using graduated light to expose photosensitive gelatine that expands in proportion when treated with water [28], [34].

Topography and photosculpture techniques captured the concept of producing a freeformed shape; however the computing technology and availability at the time had restricted them from doing so[34]. It was in 1951 when Munz [38] proposed the system of selectively exposing a transparent photo emulsion in a layerwise fashion where the layer is a cross section of the object [28], [34]. The system included the concept of lowering a piston and adding the required amounts of material to produce the layers which required post machining processes to produce the three-dimensional object [28]. This system is shown in Figure 2-14.

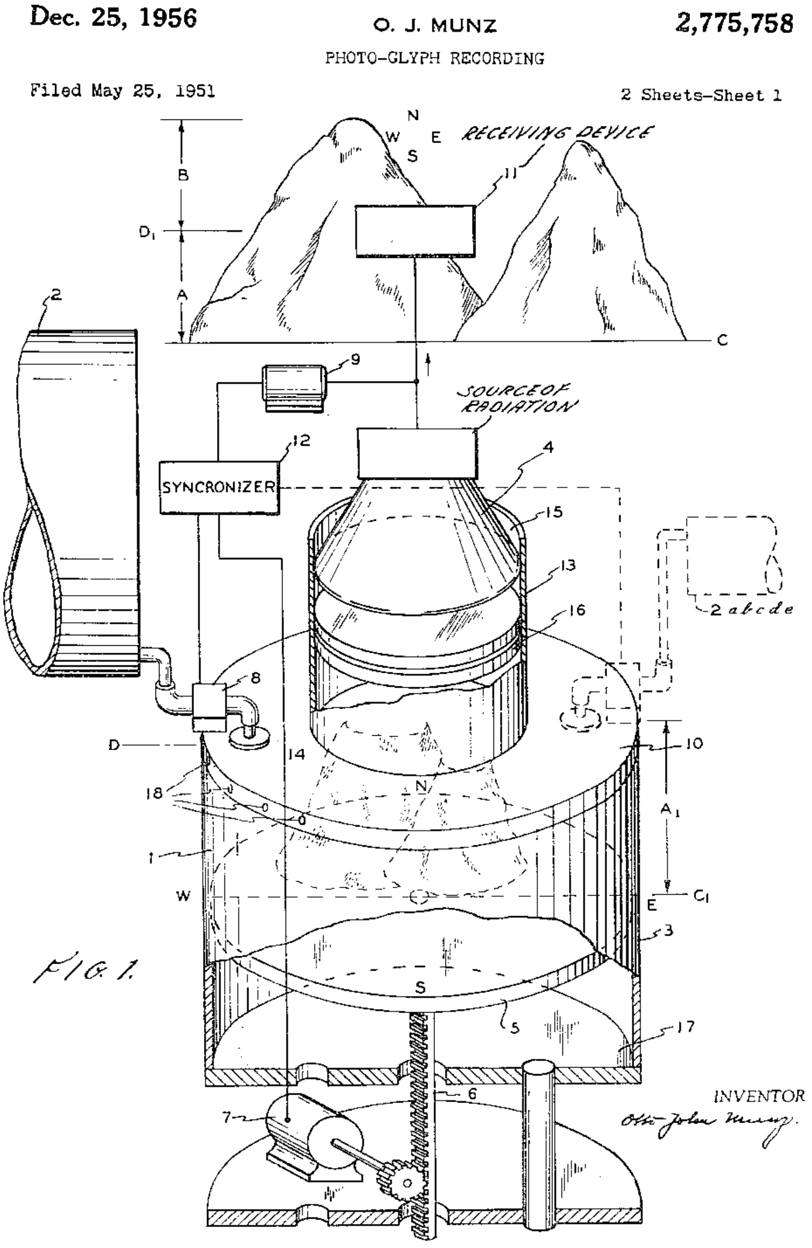

Figure 2-14: Photopolymer technique of Munz [38]

A process termed Photochemical Machining, proposed by Swainson [39] in 1968, would directly fabricate a plastic pattern by selective, three dimensional polymerization of a photosensitive polymer at the intersection of two laser beams [28]. Parallel work conducted at the Battelle Laboratories constructed hardware for the process, but a commercially viable process was not achieved [28]. A schematic of Swainson's system is shown in Figure 2-15. The first process which has all the modern direct deposition additive manufacturing techniques was proposed by Ciraud [40] in 1971. This system is a powder process where an object may be manufactured from a variety of materials that are at least partially able to melt [28]. Parts are produced by particles being drawn to a matrix by gravity, magnetostatics, electrostatics, or positioned by a nozzle located near the matrix [28]. Particles locally adhere to each other with the use of laser, electron or plasma beams and if required, more than one beam may be used to increase particle adhesion [28]. This is shown in Figure 2-16.

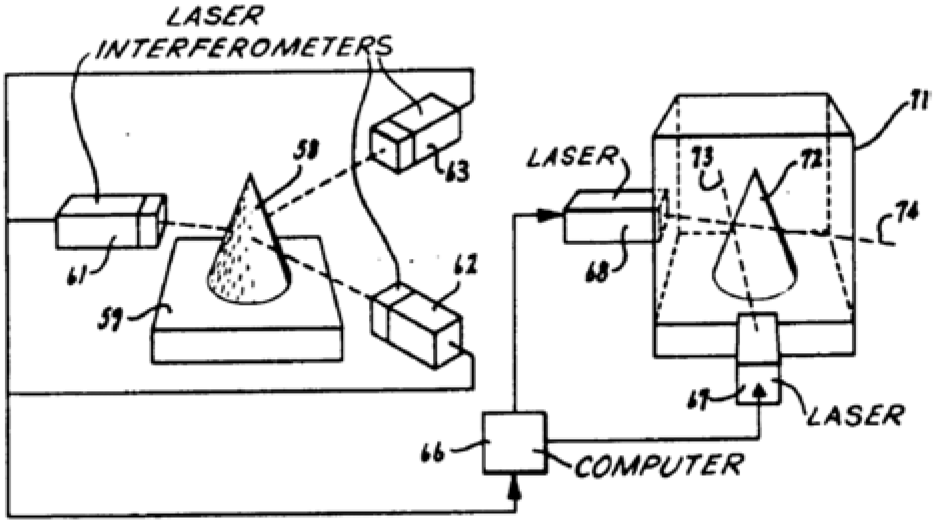

Figure 2-15: Photochemical Machining process proposed by Swainson [39]

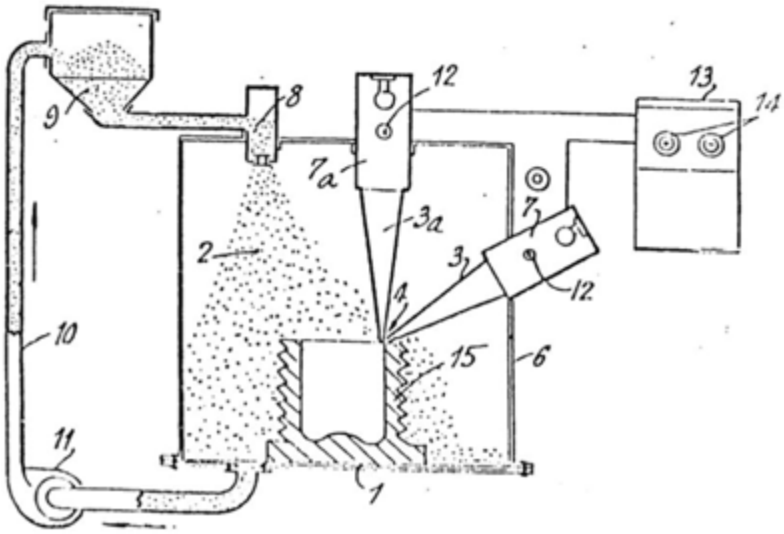

Figure 2-16: Direct deposition AM technique proposed by Ciraud [40]

Householder [41] presented the initial powder laser sintering method in a patent [28]. In this patent, he discussed depositing planar layers of powder sequentially and selectively solidifying it using a controlled heat scanning process [28], [41]. Kodama [42] was the first to publish an account of a functional photopolymer rapid prototyping system [28]. In this technique, a three dimensional model is built up layerwise where exposed areas corresponded to cross sectional layers [28], [42]. He dealt with three methods for this technique, using a mask to control exposure of an UV source and (i) immersing the model downward (ii) immersing the model upwards into a liquid photopolymer vat to create new layers and (iii) using an x-y plotter and an optical fibre to expose the new layer rather than the UV source [28], [42].

Over the years AM technologies have improved to such a great extent that today intricate parts may be produced. However, those who had proposed and developed these systems, mentioned within this section, required great trust that improvements would occur [28].

2.2.2 Emergence of Direct Metal Laser Sntering

These proposals described in the previous section were the stepping stones to the commercialisation of additive manufacturing during the 1980’s [43]. Chuck Hull [44], the founder of the company 3D Systems commercialised the technology described in his patent.

The patent did not clearly mention the use of powder but used a vat of liquid resin similar to that proposed by Komoda [43]. Hull realised that this concept was not limited to liquids and so termed the concept stereolithography (Solid free-form fabrication, 3D printing, optical fabrication etc) and filed broad patents covering any “material capable of solidification’ or “material capable of altering its physical state” [43]. The portfolio of Hull’s patents covers relevant fundamental aspects of today’s additive manufacturing technologies such as the STL files and alternating hatch directions for exposure strategies [43]. In 1997, the company EOS acquired the rights to 3D Systems patent portfolio for the field of Selective Laser Sintering (SLS). It was in the same year that 3D Systems stated “One specific stereolithography technology is known simply as stereolithography and uses a liquid medium. Another stereolithography technology is known as Selective Laser Sintering (SLS). SLS is based on the selective solidification of layers of a powdered medium" [43].

Carl Deckard [45], a Masters student from the University of Texas (UT) investigated a similar technique to that of Hull’s, but with the use of powdered material [43]. Initially terming it Part Generation by Layerwise Selective Sintering (PGLSS) and then later changing it to Selective Laser Sintering (SLS) [43]. The patent filed described the technique as “computer aided laser apparatus which sequentially sinters a plurality of powder layers to build the desired part in a layer-by-layer fashion” [43]. This technique was basically identical to that of Householder’s but with actual experiments taking place [43].

Desk Top Manufacturing (DTM), a company set up to commercialise and develop the technology by UT, introduced the first proper commercial system for laser sintering termed Sinterstation 2000 which was first shipped in 1992 [43]. The next system to be commercialised was that of EOS which was first shipped in 1994. At this stage, both companies had not yet successfully sintered powder metal [43]. A comparison of the two commercial systems is shown in Table 2-4.

Table 2-4: Comparison of the Sinterstation 2000 and EOSINT (P) 350 systems [43]

Feature	Sinterstation 2000	EOSINT (P) 350
Laser	CO_2, 50 Watt	CO_2, 50 Watt
Build volume	Ø305mm x 410 mm = 30 litres	350mm x 350mm x 600mm = 73.5 litres
Powder dispensing	From below	From above
Layer application method	Counter-rotating roller	Vibrating channel
Scanning method	Raster	Vector
Part removal	From above	From below
Early materials	Wax, polycarbonate	Polystyrene, nylon mixture

Parallel research conducted by various institutes experimented with sintering metal in the early 1990's with successful reports by Fraunhofer IPT and Katholieke Universiteit Leuven using 316L stainless steel and Fe-Cu mixtures respectively [43]. Soon after, collaboration between EOS and Electrolux Rapid Development (ERD) produced the first commercial Direct Metal Laser Sintering (DMLS) system. This collaboration opened the doors for commercial use of DMLS for rapid tooling [43]. With the introduction of the EOSINT M250 system, improvements to the materials and processes rapidly increased which then lead to the EOSINT M270 being released in 2004 [43]. This system used a solid-state fibre laser which has the capabilities of partial (SLS) and full melting (Selective Laser Melting) of powders [1].

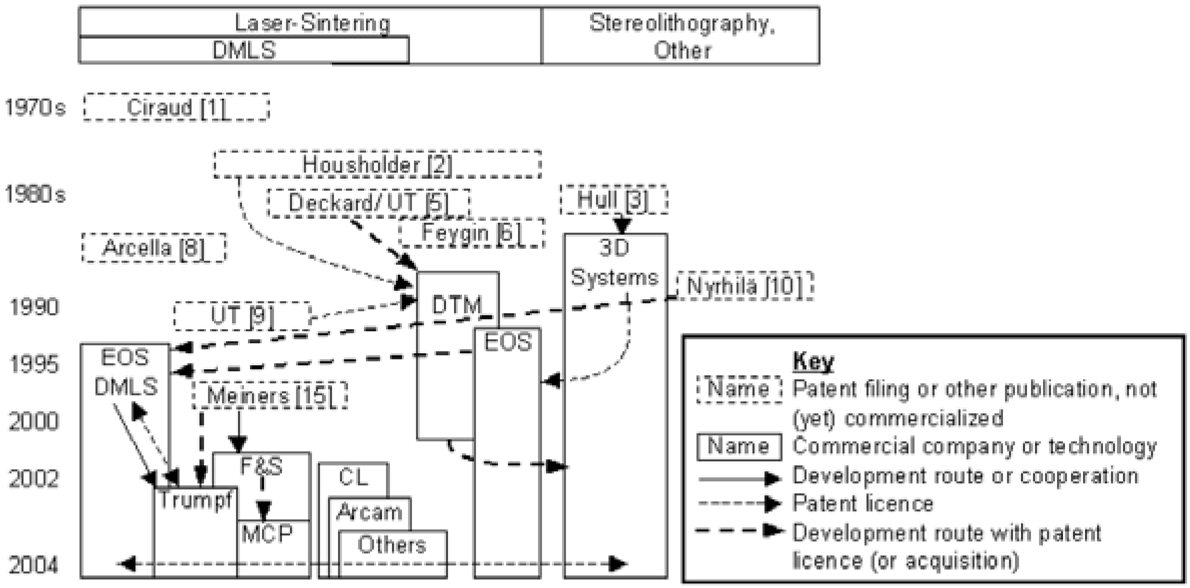

Figure 2-17: Graphical representation of additive manufacturing timeline [43]

2.4 Direct Metal Laser Fabrication

As discussed in the previous section, the development and commercialisation of additive manufacturing technologies improved a great deal once the first reports of successful metal sintering arose. With improvements to laser technologies, computer aided control and powder metallurgy, the process of Direct Metal Laser Fabrication (DMLF) was developed. The purpose of developing DMLF was to fabricate metals directly, particularly mechanical components such as turbine blades and functional prototypes of complex geometry [46]. There are two systems to DMLF techniques: Partial melting and full melting systems [47].

2.4.1 Techniques

Partial melting and full melting system may be divided into separate divisions as can be seen in Figure 2-18 and will be briefly discussed below.

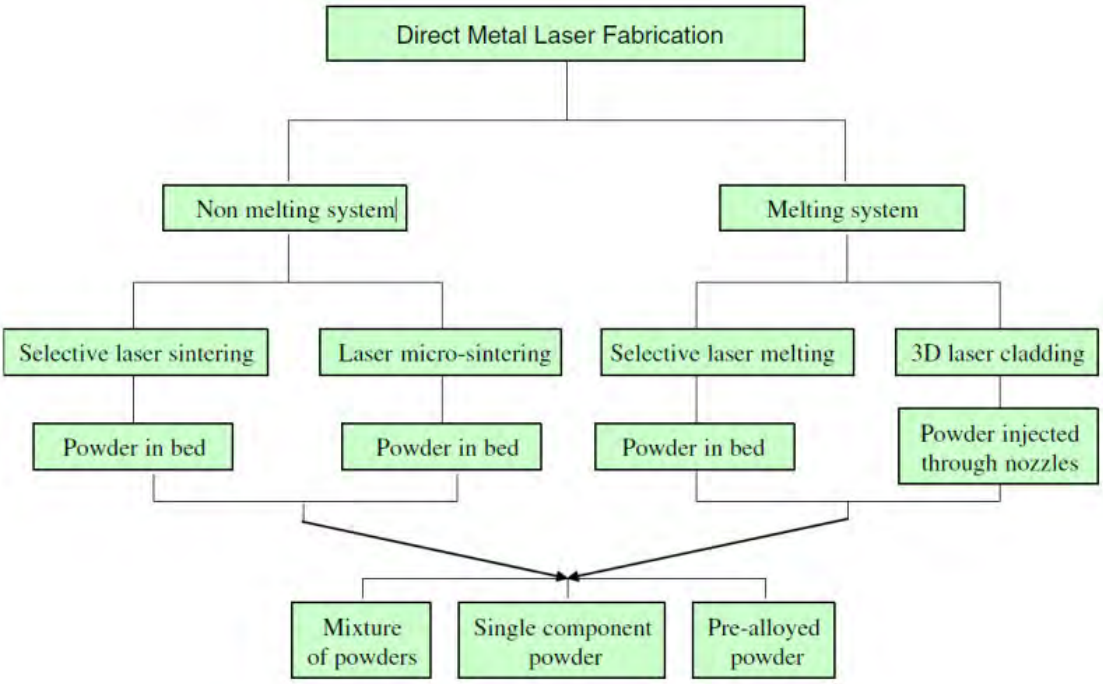

Figure 2-18: Classification of rapid manufacturing methods for direct laser fabrication of metal parts [24]

Selective Laser Sintering

This technique of DMLF uses a thin layer of powder which is deposited onto a build-up area. A laser beam, guided by galvano mirrors, then passes over the build-up area which in turn sinters the thin layer of powder. Once the layer is sintered, the build-up area drops in height by one layer of powder (0.02 - 0.1 mm). A new layer of powder is then deposited on the build-up area and the cycle continues until the component is complete. In this manner, the component is built layer-by-layer from a sliced CAD model. The Selective Laser Sintering (SLS) process takes place in a sealed chamber where the operation is performed in an inert atmosphere (nitrogen or argon) to avoid oxidation [24]. The SLS process is illustrated in Figure 2-19.

Depending on the complexity of the part, parts may require support structures when manufactured. Without support structures, there is a restricted angle or overhanging length which can be built. The supports are required for satisfactory surface finish and adequate adhesion to the plate. [48]

Selective Laser Melting

Selective Laser Melting (SLM) uses a process very similar to that of SLS with the exception of using a much higher energy density laser to enable full melting of the powders [24]. Due to the full melting of powders, fabricated parts attain densities very close to that of the theoretical one [24]. The SLM process is illustrated in Figure 2-19.

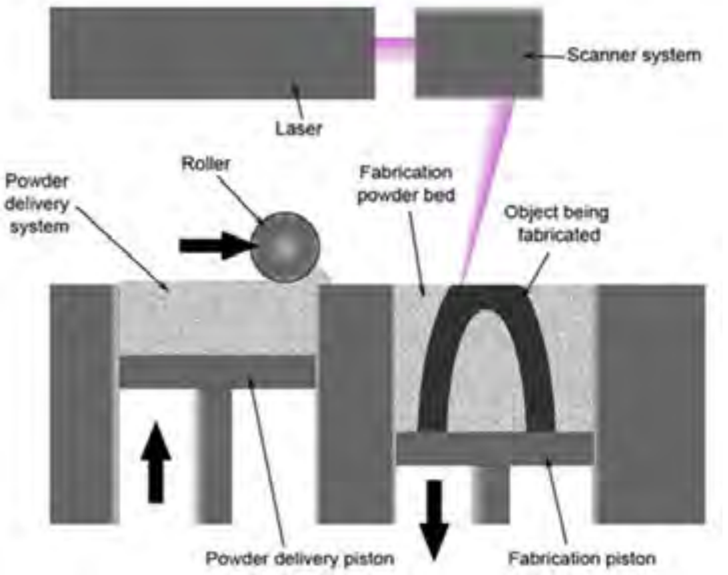

Figure 2-19: illustration of the selective laser sintering/melting process [49]

3D Laser Cladding

3D laser cladding, also known as Laser Engineered Net Shaping (LENS), makes use of powder being injected through nozzles into a laser-generated melt pool, corresponding to a CAD model [24], [50]. Parts are built up in a layerwise fashion where the laser beam and powder nozzle form an angle between each other, typically from 0° - 45° and is approximately 5mm above the melt pool [24], [51]. Due to the powder being injected through nozzles, this technique allows for damaged parts to be repaired and put back into service resulting in a longer service life [50]. The 3D laser cladding process is illustrated in Figure 2-20.

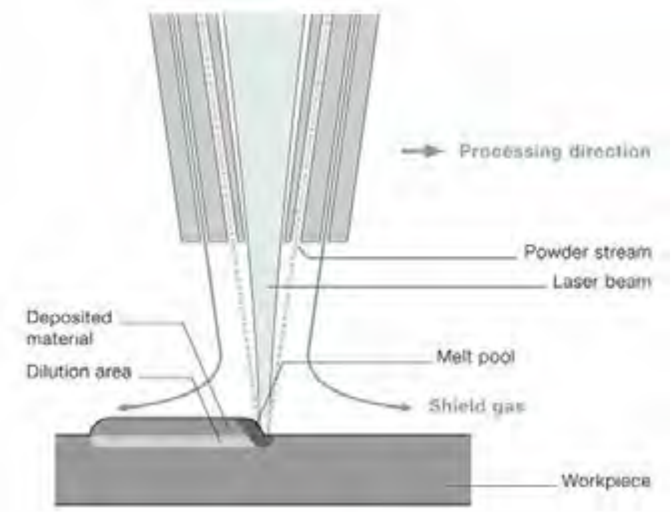

Figure 2-20: Illustration of the 3D laser cladding process [52]

2.4.2 Binding Mechanisms

The continuously improving process parameters of DMLF have brought about densities and mechanical properties comparable with that of bulk metal properties. The improved parameters allow for better binding to occur between particles. There are various forms of binding; however, three primary categories are briefly discussed below. Figure 2-21 below summarises the binding mechanisms that will be discussed.

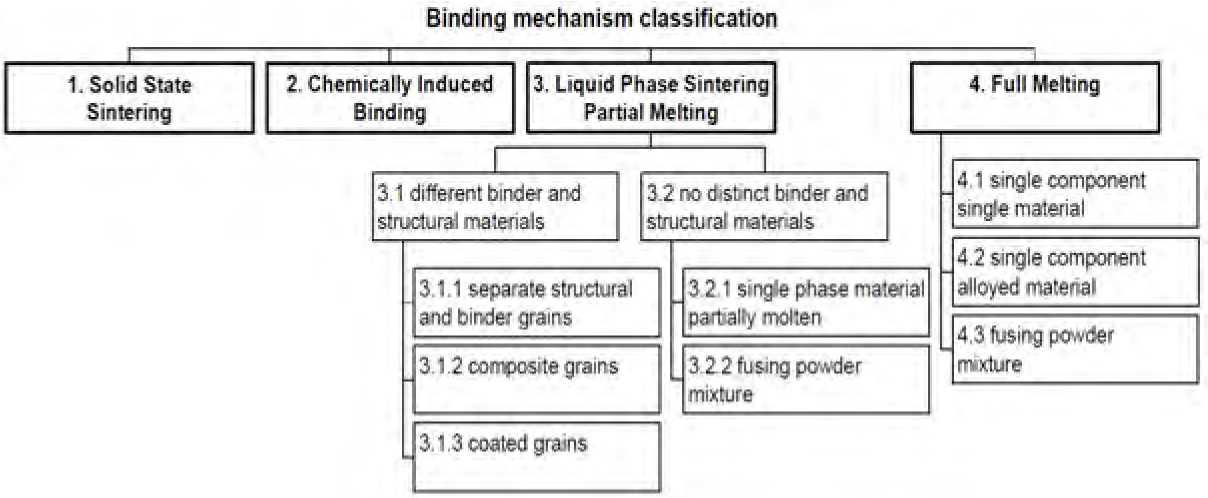

Figure 2-21: Classification of binding mechanisms of powder material [26]

Solid State Sintering

Solid State Sintering (SSS) occurs at temperature below the melting point (T_{melt}) and above $T_{melt}/2$ of the material [26]. The consolidation process occurs by the diffusion of adjacent particles which in turn creates a neck between particles [26], [53]. This necking between particles reduces pore volume and therefore increases densification of the part. Preheating of the powder material is often required as this helps with laser scanning velocity, considering that the process is rather slow which would impact process productivity [26], [53]. SSS may be used in processes such as SLS but is a rather slow binding mechanism and is rarely used [53].

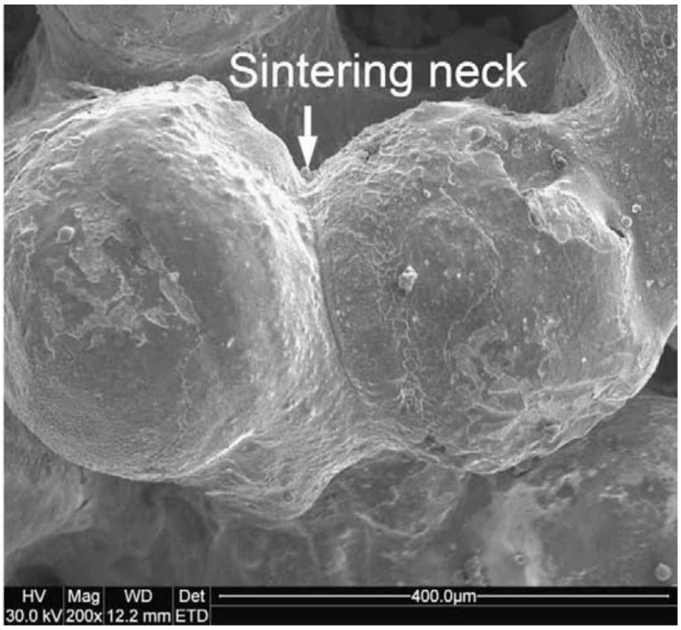

Figure 2-22: Neck formation in Solid State Sintering [54]

Liquid Phase Sintering

Liquid Phase Sintering (LPS) uses a form of binding mechanism where there is a combination of material for structural and binding purposes [26]. The structural material would remain solid throughout the process while the binding material is required to be liquefied for binding to occur [26]. There are cases, however, where the structural and binding materials are the same material [26]. There are various forms of incorporating the binding of the structural material [53]:

1. Mixture of two-powder material i.e. separate structural and binding powder particles.
2. Composite powders where individual particles contain both structural and binding material.
3. Coated particles where the binding material is coated on the structural material.

LPS is also in processes such as SLS although parts produced may be porous and require a post processing densification procedure [53]. The SLS parameters may be adjusted in the case where there is no clear binding and structural material, so that the shell of the particle material is melted but the core remains solid [53].

Full Melting

With the idea of attaining full densification of parts, laser technology has improved to an extent where powder material may now be fully melted. Major progress has been made where densities of 99.9% may be achieved [53]. The full melting mechanism is used by methods such as SLM and allows for the melting of single material powder, alloyed powder and fusing a powder mixture [26]. This process does however come with its drawbacks due to the high temperatures and resulting in large internal residual stresses [53]

2.4.3 Commercialised Systems

Over the years, many companies had started to develop printers to enter the 3D printing market. The three leading companies are EOS, Concept Laser and SLM Solutions which are all based in Germany [55]. Along with these and other companies, specific terms came about for the consolidation of parts. Terms such as Selective Laser Melting, Direct Metal Laser Sintering, Selective Laser Sintering and LaserCUSING all came about with the development of specific company printers, which also brought a lot of confusion about the differences between these terms and methods used.

The patents filed by Ciraud [40] and Householder [41] were the first to resemble the modern idea of 3D printing which is the principal idea behind DMLS and SLM. Deckard [45] who made the first SLS machine when the company DTM was formed held the rights to laser sintering but this was later acquired by EOS who got the rights and portfolio to DTM (including 3D systems and UT) [43]. The different companies themselves are not very clear about their technologies differences to other companies' printers apart from mainly using the terms SLM, DMLS etc. There are procedural similarities between these four methods [56]:

- A part is modelled on a CAD programme
- The part is virtually sliced by the software (STL file)
- Consolidation takes place within a chamber in an inert atmosphere on a powder bed
- A laser selectively solidifies the powder, building a part up in a layerwise fashion
- Unused powder may be reused after going through a sieving process.

One can look at SLS and DMLS as the same thing since the company EOS has the rights over these methods and terms. Although SLS initially was used on a variety of materials such as wax, polycarbonates, glass, ceramics etc. it today is almost only used for polymers [55]. DMLS, as the name suggests, is used for the consolidation of metals.

The company Concept Laser uses a method known as LaserCUSING, combing the C from Concept and the word Fusing (complete melting) [57]. LaserCUSING is a patented method which uses an “island principal” scanning strategy to reduce stresses and warping of a component [57]. An individual layer of material is lasered in lots of small segments (islands) to make up the complete melted layer.

SLM Solutions uses the SLM method to consolidate parts and also co-owns the name rights for SLM [55]. No specific scanning strategy is made mention of but it may be because of the co-ownership to naming rights that other companies had come up with different names and slight changes to scanning strategies so not to infringe on any rights.

Although these companies have come up with their own terminology and methods which have technical differences, SLM often seems to be the generic trade name or proprietary eponym for LaserCUSING and DMLS [56]. In short, these differences in names and methods come down to marketing and patent issues [56].

2.4.4 Selective Laser Melted Ti-6Al-4V

There is a presence of non-equilibrium phase in Ti-6Al-4V due to large temperature gradients characteristic of SLM [58]. This non-equilibrium occurs in the as-built SLM microstructure which has a very fine, acicular martensitic structure (α’ needles) as seen in Figure 2-23 [58], [59]. X-ray diffraction (XRD) analysis indicates that there is only a presence of the HCP structure in the as-built microstructure [58] ,[59], [60]. Due to the martensitic microstructure, the yield stress of as-built SLM Ti-6Al-4V is higher than the wrought alloy [59]. There is, however, a reduction in ductility due to martensite, microcracks and residual stress [59]. During SLM, columnar grains are formed which are, for the most part, in the direction of the build direction [60]. This is because of the partial remelting of previous layers and there is no nucleation barrier to solidification during SLM [58]. These columnar grains may be observed in the front and side view of a sample, as in Figure 2-24. The reason for the grain direction to be slanted in Figure 2-24 is because the grain orientation has a dependence on scanning velocity, scanning strategy and local part geometry [58]. Thus the actual direction with the columnar grains is parallel to the local conductive heat transfer direction [58]. This suggests that the scanning strategy may be a tool to manipulate the grain orientation and microstructural structure [58].

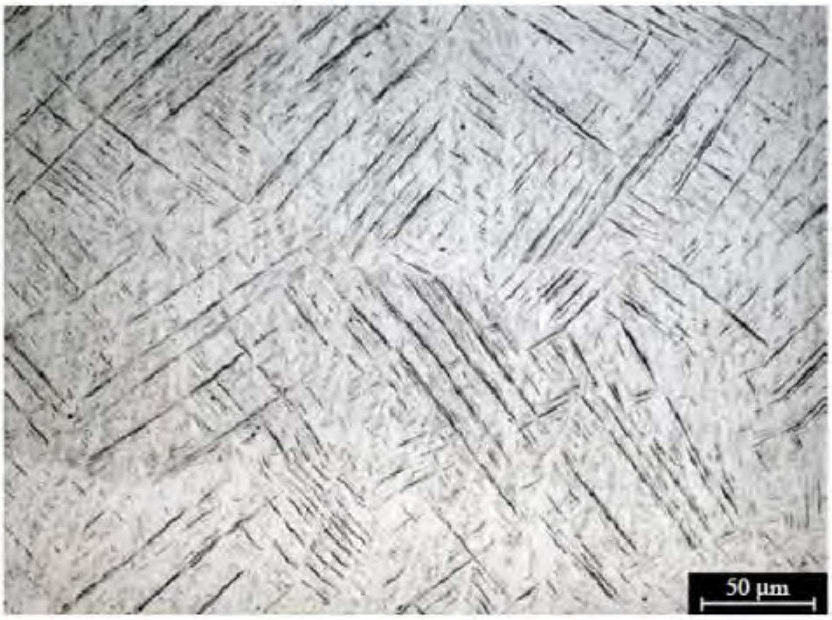

Figure 2-23: Microstructure of Ti-6Al-4V produced by SLM [59]

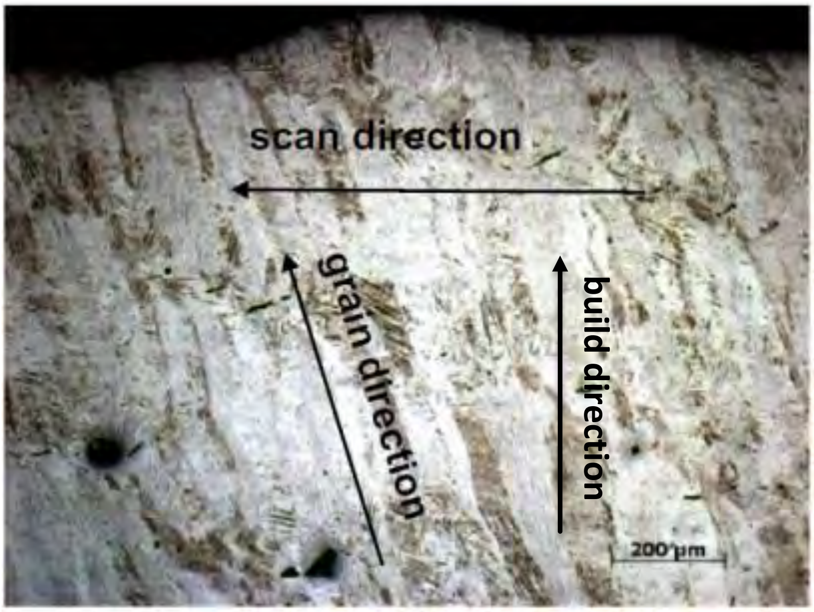

Figure 2-24: Columnar grains from a side view [58]

2.4.5 Residual Stress

SLM makes use of high energy laser beams which introduce large thermal gradients into a component [61]. These thermal gradients cause residual stresses to remain in a part after the SLM process is complete and the part has reached an equilibrium state with the environment [61]. The residual stresses restrict the practical use of a part as it limits the loading capabilities compared to a residual stress free part and may introduce deformations and microcracks into a part [61], [62]. It is therefore of great concern to relieve the residual stress of SLM products.

There are two mechanisms which induce residual stresses into a component [61]. The first mechanism is called the temperature gradient mechanism (TGM) in which large thermal gradients develops around the laser spot due to rapid heating on the material surface but slow conduction to the rest of the material [61]. The heated surface layers wants to expand, but this motion is restricted by the cooler underlying material layers which then induce elastic compressive strains [61]. The second mechanism occurs during the cool-down phase where the surface layers, which were previously heated, want to contract but are restricted in the motion due to the surrounding material [61]. This restriction causes large tensile stresses at the surface layers with compressive stresses below that and tensile stresses again towards the bottom of the material [61]. The two mechanisms are schematically depicted in Figure 2-25.

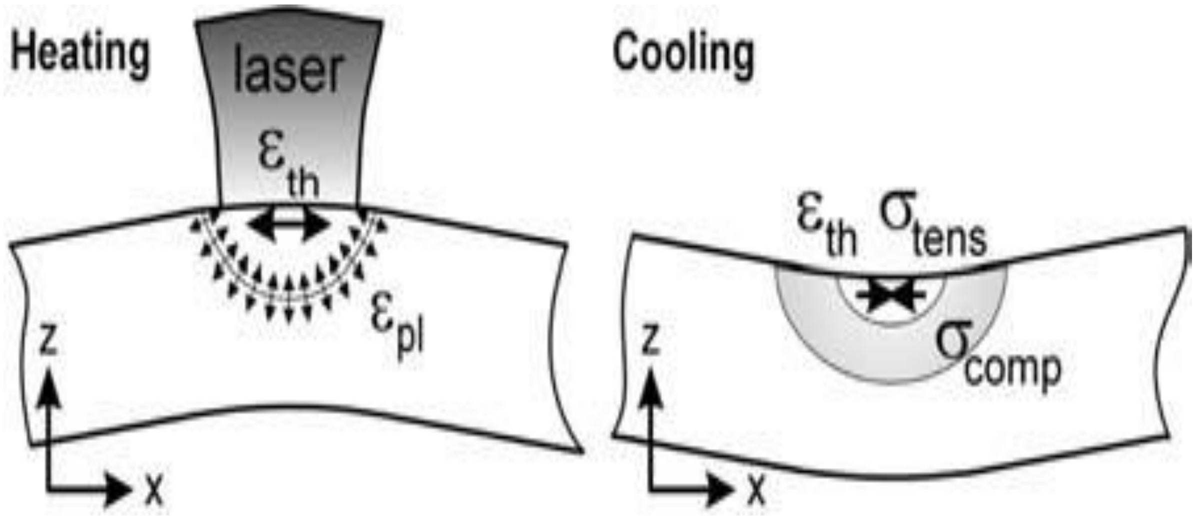

Figure 2-25: Residual stress inducing mechanisms [61]

When a part is removed from the fabrication, there is a reduction in the residual stress as the stress relaxes via shrinkage and bending deformation [61]. The most important parameters which affect the magnitude of the residual stress in the part are the material properties, part and fabrication plate height, laser scanning strategy and heating conditions [61]. Methods to reduce residual stresses include post production heat treatments, the heating of the fabrication plate as this reduces the temperature gradient, and a laser rescanning process [61], [62].

2.5 Linear Elastic Fracture Mechanics

Fracture mechanics concerns itself with the understanding of crack propagations through a material. It is a specialization within solid mechanics in which the relationship between the presence of a crack, the materials ability to resist crack growth and the stress at which a crack propagates is quantified [63]. Linear Elastic Fracture Mechanics (LEFM) requires material to behave in a linear elastic manner, such as non-ductile material, where any plasticity in the material is required to be small compared to the size of the crack i.e. small scale yielding. If the material exhibits large scale yielding, it needs to be analysed under the methods of Elastic Plastic Fracture Mechanics (EPFM) or other techniques.

The fundamental theory of LEFM introduces the concepts of critical energy release rates based on global energy balance considerations, known as the Griffith theory of brittle fracture in order to analyse the crack propagation through a material [64]. An equally fundamental theory of LEFM is introduced by Irwin's theory of brittle fracture in which the concept of the Stress Intensity Factor (SIF) approach is used for crack propagation analysis.

In LEFM there a three modes of fracture called mode I, II, and III which are depicted in the Figure 2-26 below.

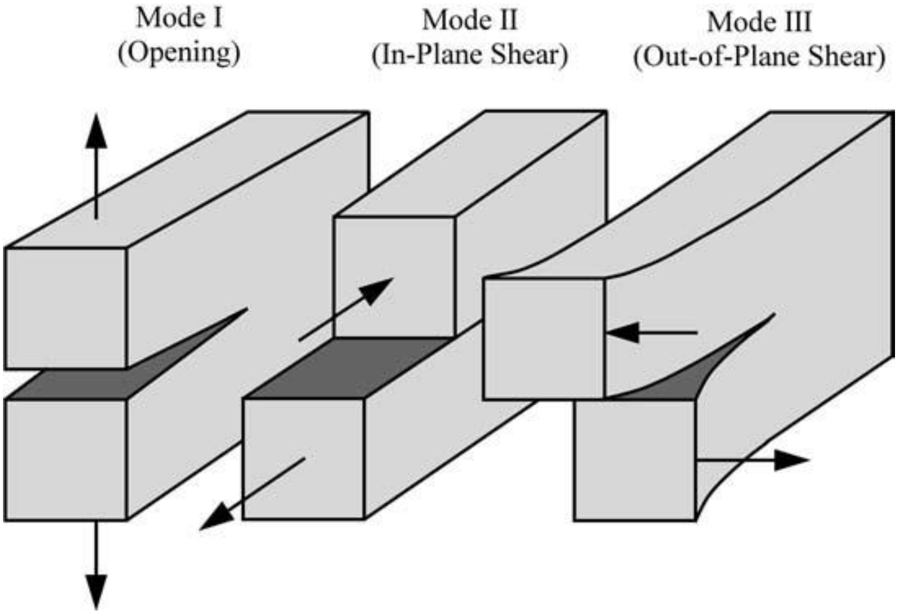

Figure 2-26: The three modes of fracture [65]

This study only deals with the concept of LEFM and briefly discusses the idea of the SIF for mode I fracture.

2.5.1 Stress Intensity Factor

The SIF approach to predicting fracture is a more commonly used method as it deals with crack tip stresses (and strains), which are more commonly used in engineering [66]. In fracture mechanics, the SIF concept considers the crack tip stress field using a single constant, based on the applied load and geometrical conditions. This concept is better understood with the help of visual aids such as in Figure 2-27.

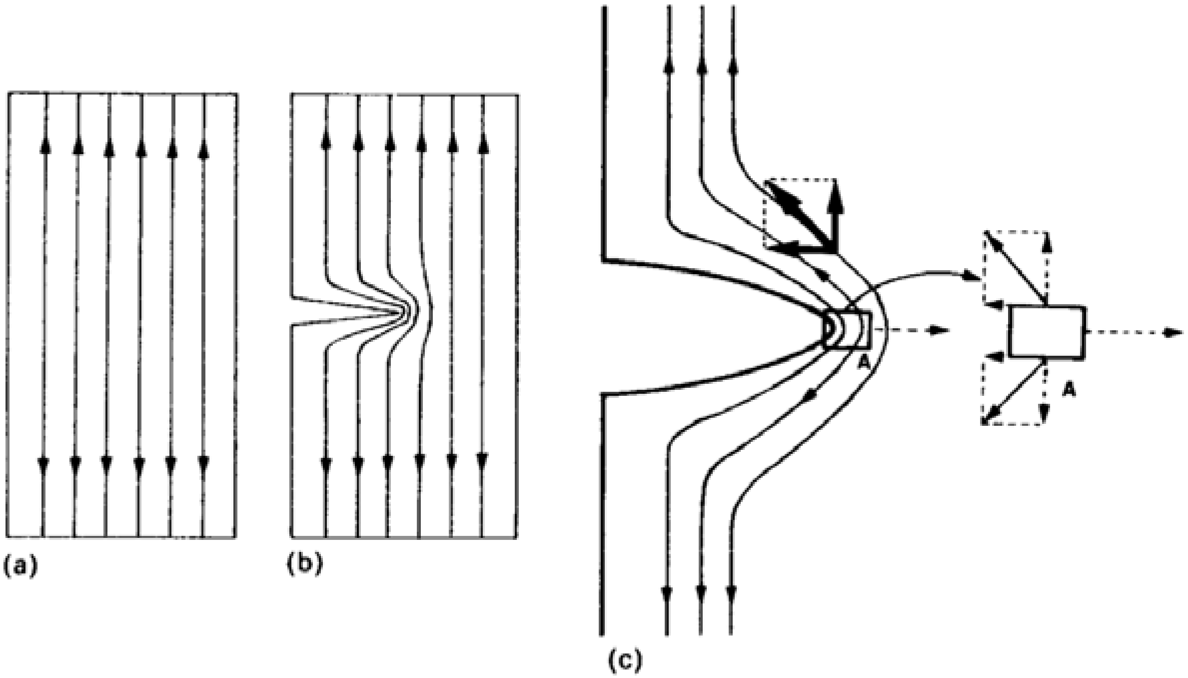

Figure 2-27: Load-flow lines [67]

Figure 15a considers a plate being subjected to a uniform tensile stress which produces uniform load-flow lines. With the addition of a notch to the same plate under the same loading conditions such as in figure 15b, it can be seen that the load-flow lines need flow around the notch resulting in the flow lines being spaced much closer to each other within a small area. This means that the stress is now concentrated around the notch which results in a higher local stress. Figure 15c magnifies the notch area, and shows that the notch tip radius is not sharp and would be measurable compared to that of a crack-tip radius. If one assumes that the crack tip is extremely sharp, the crack radius would approach zero and hence the local stresses at the crack-tip would experience a much larger stress gradient, which theoretically approaches infinity, within a small area. In reality however, the crack-tip radius is finite but due to its geometrically sharp nature, it produces an intensified stress concentration around the crack-tip which is dependent on the applied load, leading to the term Stress Intensity Factor. Fracture mechanics has this concept based on the parameter K which predicts the magnitude of the local stress state at the crack tip and is called the Stress Intensity Factor (SIF) and is defined by:

$$K_I = Y\sigma\sqrt{\pi a} \tag{2.1}$$

Where σ is the applied stress, Y is a geometrical modification factor and a is the crack length. The SIF is measured in $MPa\sqrt{m}$ and the subscript I denotes the Mode I fracture condition. Equation 2.1 shows a relationship between the variables K_I, σ and a which is known as the "triangle of integrity" which is used for predicting the integrity of a component.

2.5.2 Fatigue

When an object undergoes a fluctuating stress well below the materials yield stress, accumulated damage will occur and fracture by fatigue will eventually take place [68]. Fatigue may be divided into two categories: initiation and propagation [69]. It is estimated that over 80% of all mechanical service failures are due to fatigue and is the primary cause of turbine-engine failure in military aircraft [68], [70]. Examples of fluctuating stresses include vibrations, take-off and landing loadings of the aircraft, pressurization and depressurization of a fuselage [69]. Aircraft wings, turbine engines, cars on the road, air craft landing gear are all subject to fatigue failure [68]. Fatigue is more pronounced in ductile material where loads are low enough so that the system remains elastic except for a small plastic zone in front of the crack tip [69]. Once the crack reaches its critical length, the structure is subjected to fast fracture [69].

Any stress raiser in a system will promote crack initiation. Notches, surface discontinuities and flaws all act as stress raisers and initiation sites, however, cracks may still initiate without any flaws in the system due to the formation of slip planes [68]. As the stresses are fluctuating, intrusions and extrusions form along the slip planes which resembles the initiation of a crack at approximately 45° to the applied stress on planes of easy shear, seen in and Figure 2-29 [68], [71]. The crack initiation phase is also known as stage I type crack growth.

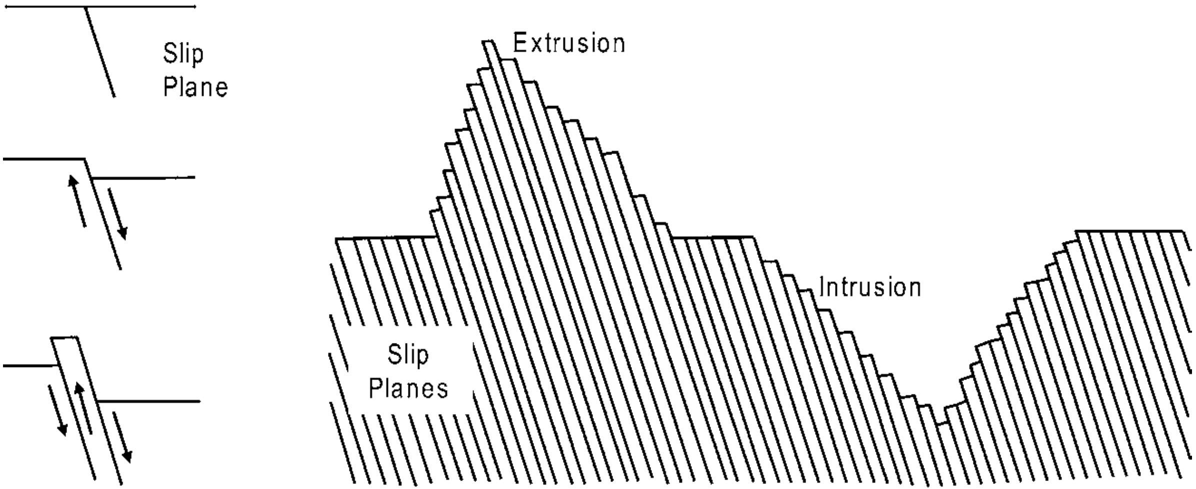

Figure 2-28: Development of extrusions and intrusions during fatigue [68]

The crack initiation phase is largely influenced by microstructural effects such as grain boundaries, inclusions and pearlite zones as they are not able to accommodate the initial crack growth direction [72]. The refinement of grains will increase the fatigue strength of a material as the initial crack will have to overcome more microstructural barriers per a unit of length [72]. As the crack length increases, the stress intensity becomes dominant and the crack direction changes and becomes perpendicular to the applied stress, and enters the crack propagation phase [68].

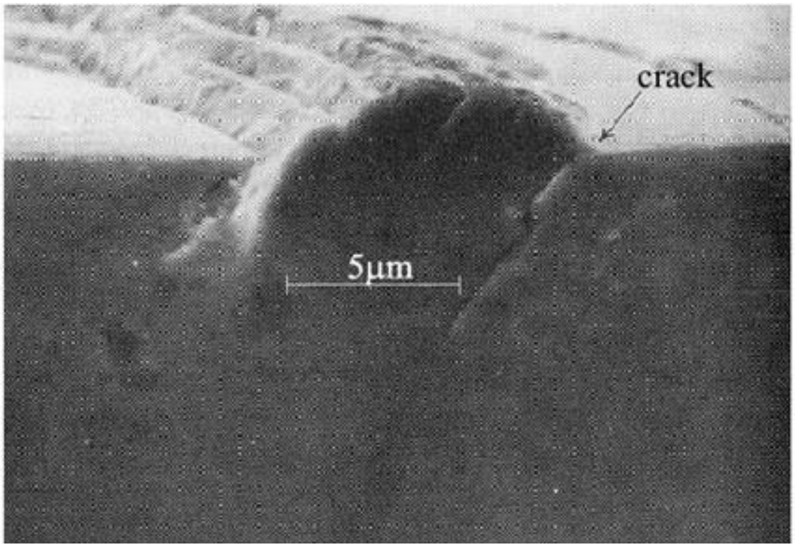

Figure 2-29: Fatigue crack initiation at a slip band [73]

The crack propagation phase is divided into two parts, stable crack growth and unstable crack growth/fast fracture. These are also respectively known as stage II and stage III type crack growth. Stage II has a very weak reliance on microstructural effects and is tension driven where it is mostly analysed by LEFM [74]. This stage of crack propagation produces fatigue patterns known as striations, where each striation represents one fatigue cycle [68]. Striations are not visible to the naked eye and require a scanning electron microscope (SEM) to be examined [68]. One of the more accepted mechanisms of striation formations is that of the continuous blunting and re-sharpening of the crack tip during fatigue loading [72]. Stages I and II can be seen in Figure 2-30.

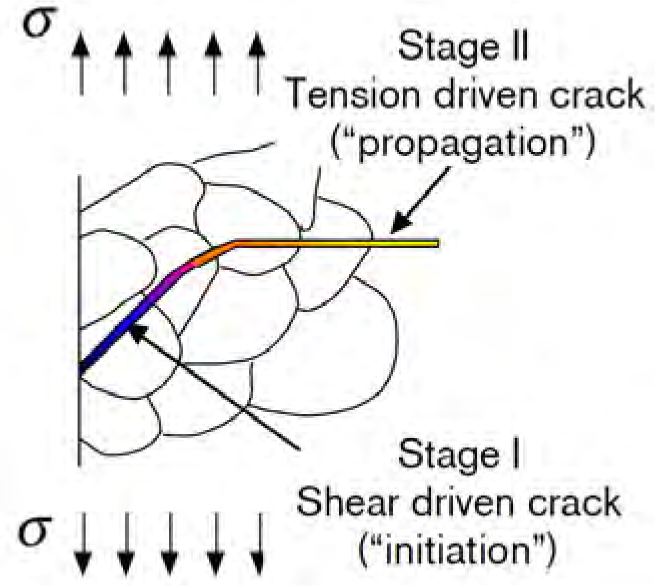

Figure 2-30: Stages I and II of fatigue crack propagation [74]

Stage III crack propagation occurs when the crack length reaches a critical length, where the remaining material can no longer withstand the stress intensity, and finally fast fracture occurs [68]. Fracture is considered to be either ductile or brittle depending on the material properties, geometry of the part and loading conditions [72].

LEFM gives both a visual and quantitative representation of the 3 stages of crack growth on what is known as the Paris curve seen in Figure 2-31.

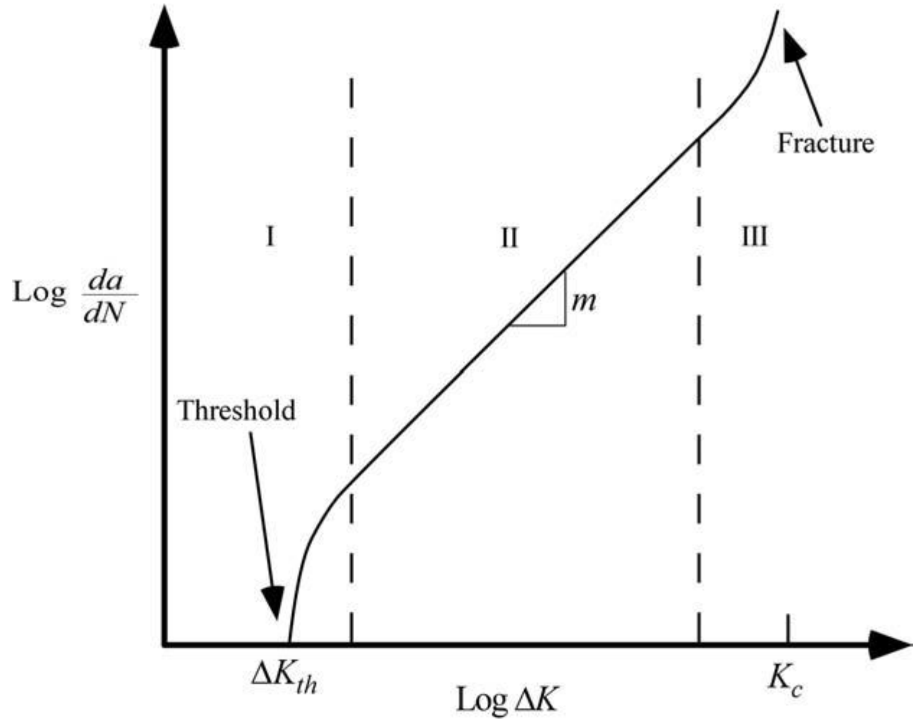

Figure 2-31: Paris curve representation of crack growth behaviour [65]

The Paris curve is placed on a log-log scale where the y-axis, $\frac{da}{dN}$, is the crack growth rate/per cycle and the x-axis, ΔK, is the cyclic stress intensity amplitude. The fatigue curve is divided into three regions which may be seen as the quantification of the three stages of crack growth. The first region refers to crack initiation; the limiting value of which is the fatigue threshold stress intensity, ΔK_{TH}, below which fatigue cracking does not occur. Region two is where stable crack growth occurs and there is a linear relationship between crack growth rate and cyclic stress intensity amplitude. LEFM quantifies this region with a power law known as the Paris equation:

$$\frac{da}{dN} = C(\Delta K)^m \tag{2.1}$$

Where C and m are both material parameters. When the crack growth reaches region three the crack growth rate increases rapidly and the stress intensity reaches a critical value at which the material does not have the ability to resist fracture anymore, and so fast fracture occurs. This limiting critical stress intensity and ability to resist fracture is known as the materials fracture toughness.

2.5.3 Fracture Toughness

The stress intensity which causes fracture is known as the fracture toughness, K_{IC}, which may be regarded as a material property for the particular thickness and temperature under consideration. Once the fracture toughness value is reached, fast fracture will occur. Fracture toughness is governed by the equation:

$$K_{IC} = \sigma_f Y \sqrt{\pi a_c} \tag{2.2}$$

Where σ_f is the stress at fracture, Y is a dimensionless geometrical factor and a_c is the critical crack length. The fracture toughness of a material decreases with the increase in material thickness [75]. As the thickness of a specimen increases, the fracture toughness reaches an asymptotic value which is referred to as plain strain fracture toughness [65] ,[75]. The plain strain fracture toughness is considered to be the true fracture toughness of a material as it is independent of thickness [75]. The valid thickness for plane strain fracture toughness is governed by the equation:

$$B \geq 2.5 \left(\frac{K_{IC}}{\sigma_y}\right)^2 \tag{2.3}$$

Thin parts will have higher fracture toughness values and will be in plane stress or a mixed mode condition. These two conditions are accompanied by shear lips on its fracture surface [75]. The effect of thickness on fracture toughness can be seen in Figure 2-32.

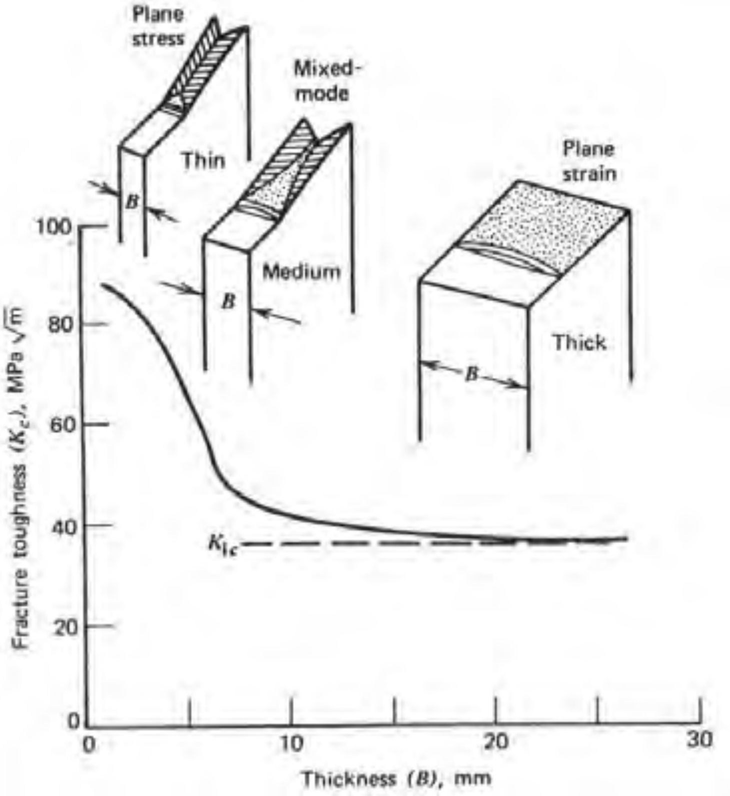

Figure 2-32: Variation in fracture toughness with specimen thickness [75]

2.5.4 LEFM Applications of Fatigue and Fracture Toughness

Flaws are an inevitable part of structures [76]. When these flaws are subjected to operational stresses, fracture mechanics may be used to assess the structural integrity of the engineering system [76]. Fracture mechanics provides a quantitative relationship between stress, flaw size and toughness whereby the structural integrity of an engineering systems may be assessed on its "fitness for purpose" [76]. This relationship is represented by what is known as the "Triangle of Integrity", as seen in [76].

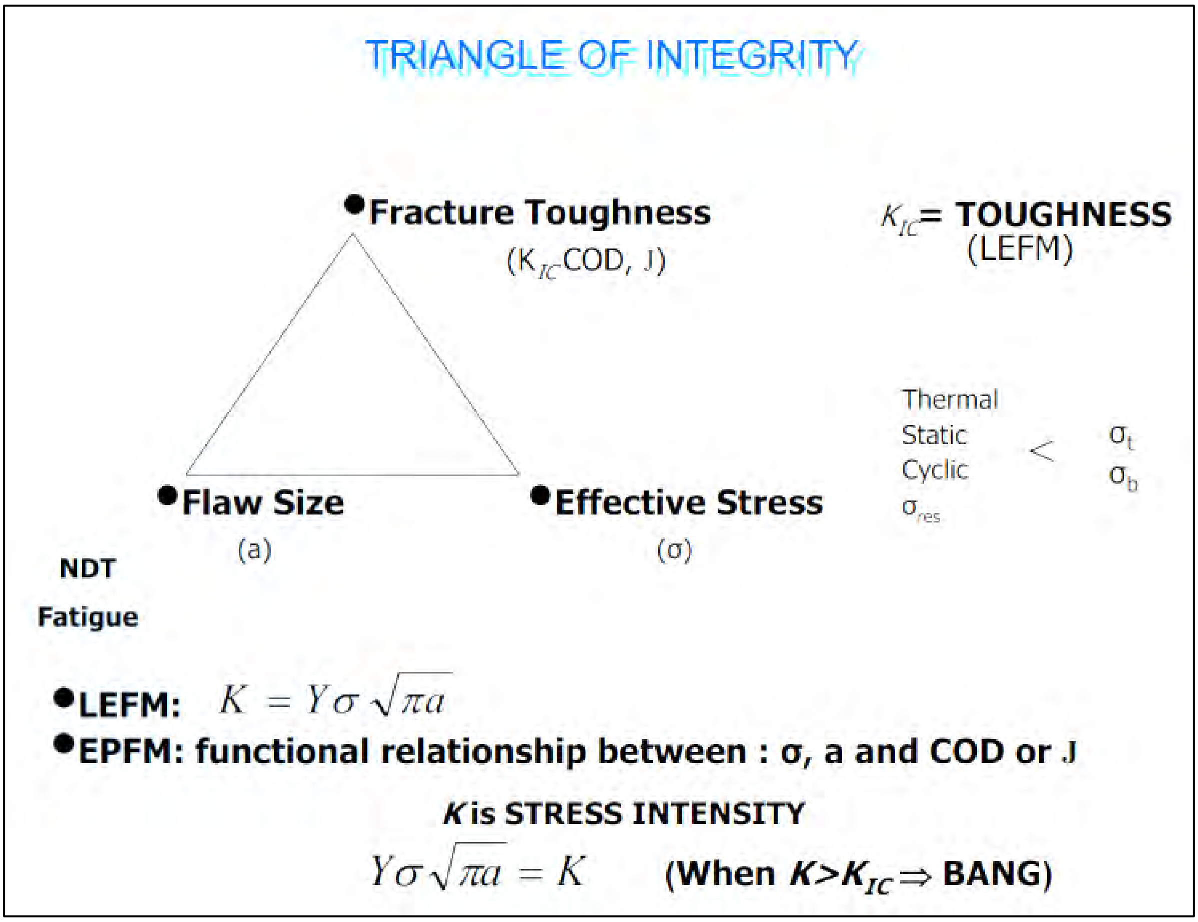

TRIANGLE OF INTEGRITY

- **Fracture Toughness**
  (K_{IC}COD, J)

K_{IC}= **TOUGHNESS**
(LEFM)

Thermal
Static
Cyclic
σ_{res}
<
σ_t
σ_b

- **Flaw Size**
  (a)
- **Effective Stress**
  (σ)

NDT

Fatigue

- **LEFM:** $K = Y\sigma\sqrt{\pi a}$
- **EPFM: functional relationship between : σ, a and COD or J**

***K* is STRESS INTENSITY**

$Y\sigma\sqrt{\pi a} = K$ **(When $K>K_{IC} \Rightarrow$ BANG)**

Figure 2-33: The "Triangle of Integrity" [77]

As long as there are two terms known of the triangle, a third may be solved e.g. if the fracture toughness of a material is known which is under an operational cyclic stress, the critical crack length for that specific scenario may be solved for. Non-destructive testing (NDT) methods are used to determine what the current crack length is so that it may be compared to the critical crack length.

The Paris equation may also be used to predict the remaining life in a component. Equation 2.2 can be substituted into equation 2.1 to form:

$$\frac{da}{dN} = C(\Delta\sigma Y\sqrt{\pi a})^m \tag{2.4}$$

Equation 2.4 is then rearranged to form:

$$dN = \frac{da}{C(\Delta\sigma Y\sqrt{\pi a})^m} \tag{2.5}$$

Equation 2.5 may then be integrated between the initial crack length a_i, obtained from NDT testing, and the critical crack a_f, obtained from the "Triangle of Integrity" so that the number of cycles to failure may be solved for:

$$N_f = \int_0^{N_f} dN = \int_{a_i}^{a_f} \frac{da}{C(\Delta\sigma Y\sqrt{\pi a})^m} \tag{2.6}$$

The combination of the "Triangle of Integrity" and the Paris equation forms a very powerful tool as it is able to answer questions such as [76]:

- What is the critical crack size at service loads?
- How safe is the system if it contains a crack?
- How long might it take for a crack to grow from initial to critical size?
- How often should a particular structure be non-destructively inspected?

2.6 Summary

The aim of this chapter was to introduce the relevant topics which have a direct influence on this research project. This chapter presented general information on titanium, Ti-6Al-4V with regards to its properties, microstructure and applications. Additive manufacturing was discussed along with SLM of Ti-6Al-4V and drawbacks from SLM. Furthermore, an introduction to LEFM was given with the basics of fatigue and fracture toughness explained and how fracture mechanics uses these two characteristics to obtain fatigue life predictions on a component.

Chapter 3 – Particular Relevant Studies

This chapter evaluates various works within literature which have undertaken studies on SLM manufactured Ti-6Al-4V with a special interest in fatigue, fracture toughness and residual stress. The aim of this chapter is to establish an understanding of recent significant literature for this project. This chapter looks at the work of:

- Van Hooreweder et al in 2012 [6]
- Leuders et al in 2013 [5]
- Edwards and Ramulu in 2014 [7]
- Knowles in 2012 [1]

The reason for evaluating these specific studies is to understand what the current literature is and what the gap in literature which should be filled is, as this research project may be seen as a continuation of these previous studies. For further details of experimentation and results of the specific studies, please refer to the relevant references.

3.1 Van Hooreweder (2012)

This research study was one of the first which dealt with the analysis of fracture toughness and fatigue of Ti-6Al-4V manufactured by SLM. As a result, the main aim of the project was to gain an initial insight of the as built SLM Ti-6Al-4V with respect to fatigue and fracture toughness. The study was conducted in Belgium at The Katholieke Universiteit Leuven where the in-house developed SLM machine was used to produce specimens with a bidirectional scanning strategy for experimentation. High quality test specimens were manufactured which resulted in a relative density of 99.7%.

Experiments were conducted using compact tension (CT) specimens for both fatigue and fracture toughness. The ASTM standards E647 and E399 were used for the fatigue and fracture toughness tests respectively. Vacuum arc remelted (VAR) mill annealed Ti-6Al-4V was used as a reference during experimentation. The fatigue and fracture toughness results are shown in Figure 3-1 and Table 3-1 respectively.

Table 3-1: Comparative fracture toughness results between VAR and SLM Ti-6Al-4V [6]

	VAR Ti-6Al-4V	SLM Ti-6Al-4V
Specimens	10	10
Density (%)	99.68 ± 0.046	99.73 ± 0.036
K_{IC} (MPa.m$^{0.5}$)	69.98 ± 3.53	52.4 ± 3.48
$K_{IC,\ 95\%}$ (MPa.m$^{0.5}$)	67.8	50.2

Van Hooreweder [6] goes onto to explain that the reason for the relatively lower fracture toughness value in the SLM Ti-6Al-4V is due to the microstructure which consists of fine acicular martensite phase. The martensite causes the material to be more brittle which then decreases the fracture toughness compared to a more ductile phase of the same material. It is also mentioned that a suitable heat treatment to transform the microstructure into an α+β matrix for improved ductility could be applied.

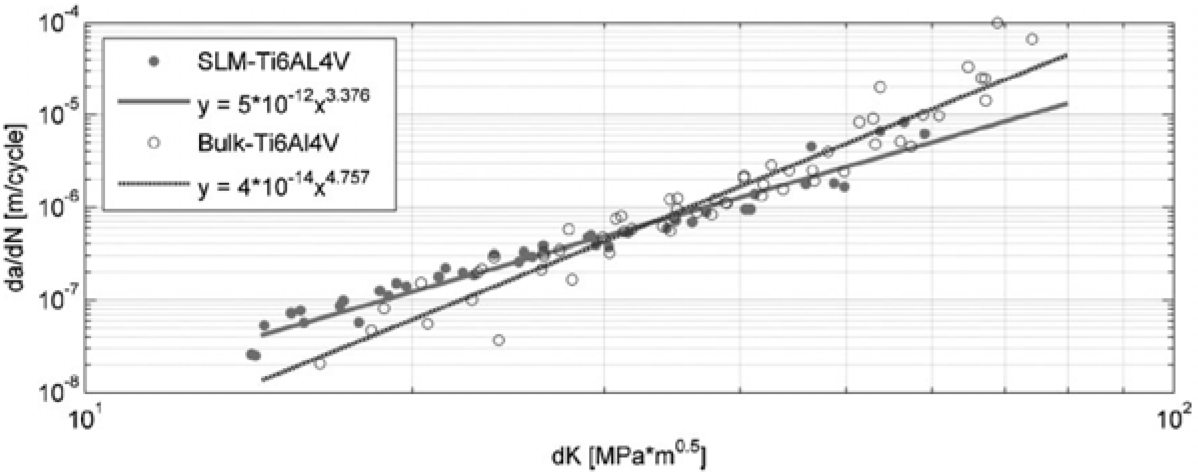

Figure 3-1: Paris curve of VAR and SLM Ti-6Al-4V [6]

It is claimed that the fatigue results for both VAR and SLM Ti-6Al-4V are similar to that found in literature. The SLM Ti-6Al-4V has a higher crack growth rate up to 30MPa.m$^{0.5}$ whereafter the VAR Ti-6Al-4V then has the faster crack growth rate. Even though the SLM Ti-6Al-4V seems to have a better performance in the higher stress intensity values, it will reach its fracture toughness value more rapidly than the VAR specimens.

The paper concluded that the inferior fracture toughness values were most likely due to the martensitic microstructure and that this microstructure lead to acceptable fatigue behaviour of the SLM material.

3.2 Leuders et al (2013)

This study investigated the high cycle fatigue (HCF) and crack growth behaviour of Ti-6Al-4V manufactured by SLM [5]. Cylindrical specimens were used for HCF testing and CT specimens crack growth behaviour testing according to the ASTM E466 and E647 respectively. The SLM 250^{HL} machine was used to fabricate the specimens which uses a 400W yttrium fibre laser. Ti-6Al-4V particles averaged 40µm with layer thicknesses of 30µm. No information on the scanning strategy has been given.

Leuders [5] considered four scenarios for testing. One as-built condition, two heat treated conditions and one hot isostatic pressed (HIP) condition. The heat treatment conditions and fatigue limit results may be seen in Table 3-2.

Table 3-2: Heat treatment parameters and fatigue limits at stress amplitude of 600MPa [5]

Case	1 As-built	2 Heat treated	3 Heat treated	4 HIPed
Temperature (°C)	-	800	1050	920(100bar)
Time (h)	-	2	2	1
Atmosphere	-	Argon	Vacuum	Argon
Cycles to failure	27000	93000	290000	2000000

It can clearly be seen that the heat treatments improve the fatigue strength of the SLM Ti-6Al-4V products. The HIPed specimens have the greatest fatigue strength as both porosity and residual stress had been decreased. The study mentions that the effect of residual stress on fatigue strength is low whereas it is the defects such as pores which have a significant effect as these decrease the time to crack initiation. Residual stress has a greater impact on the crack growth behaviour which can be seen in Figure 3-2 and Figure 3-3.

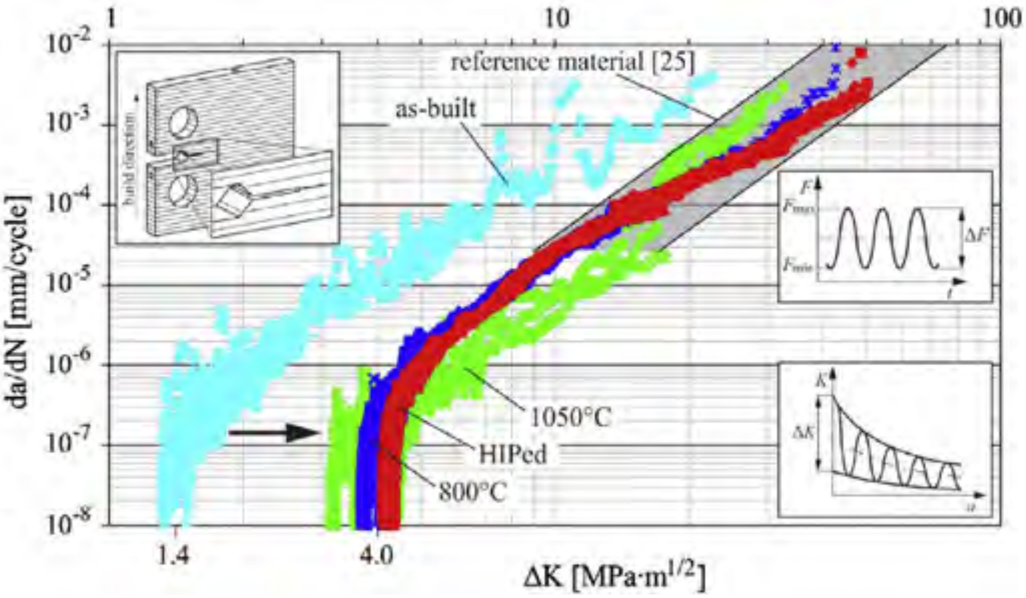

Figure 3-2: Crack growth curves of SLM Ti-6Al-4V in four different conditions for crack growth perpendicular to build direction [5]**.**

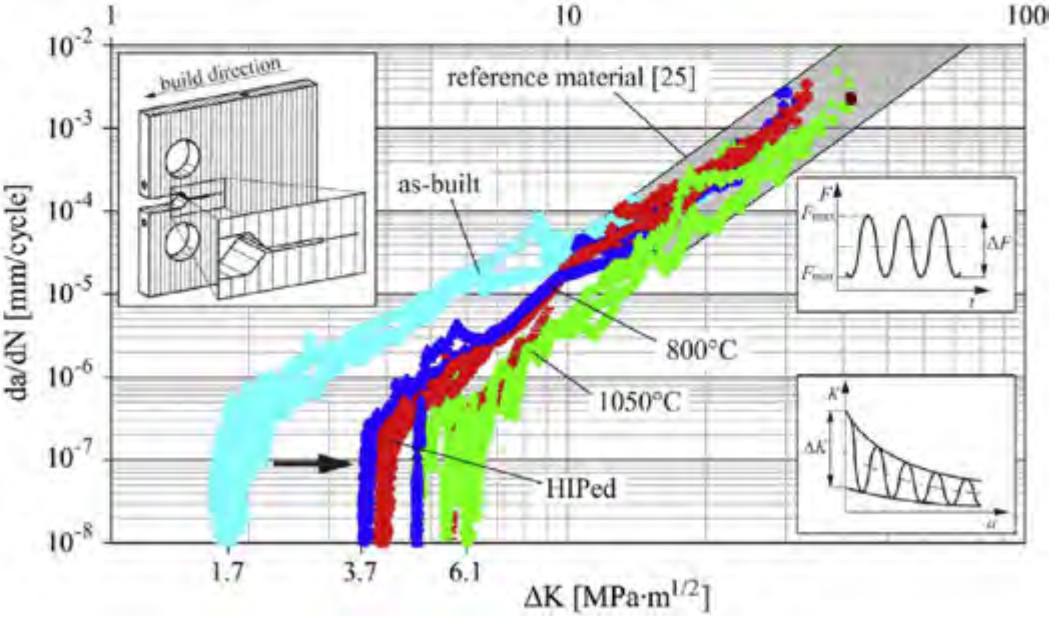

Figure 3-3: Crack growth curves of SLM Ti-6Al-4V in four different conditions for crack growth parallel to build direction [5]**.**

From both crack growth figures, it can be seen that the as-built conditions has the lowest threshold value due to the high residual stresses in the specimen. The heat treated and HIPed specimens have higher threshold values due to a decrease in residual stress and changes in microstructure due to the various heat treatments.

3.3 Edwards and Ramulu (2014)

This study concerned itself with the fatigue performance of SLM Ti-6Al-4V. Specimens were manufactured in a MTT 250 machine in an argon atmosphere. The machine has a fibre laser which was used at a full power of 200W with a scanning speed of 200mm/s. A multi-directional scanning strategy was employed which changes by 67° after each layer. Layer thickness was kept constant at 50µm.

Flat bar specimens were manufactured for the fatigue testing according to the ASTM E466 standard. Three build orientations were assessed: two "horizontal", where the profile height is parallel to the x and y-axis, and one "vertical" specimen, where the profile height is parallel to the z-axis. Fatigue testing was conducted on two specimen conditions: as-built and machined. No heat treatments or further post-processing machining took place. The target fatigue life for this study was set at 200000 cycles. Results may be seen in Table 3-3 for the machined condition specimens and Figure 3-4 for both as-built and machined conditions.

Table 3-3: Fatigue results of the different build orientations in the machined conditions [7].

Build orientation profile height	Parallel to x-axis	Parallel to y-axis	Parallel to z-axis
Number of samples	3	4	5
Failure stress at cycle limit	240MPa	170MPa	100MPa

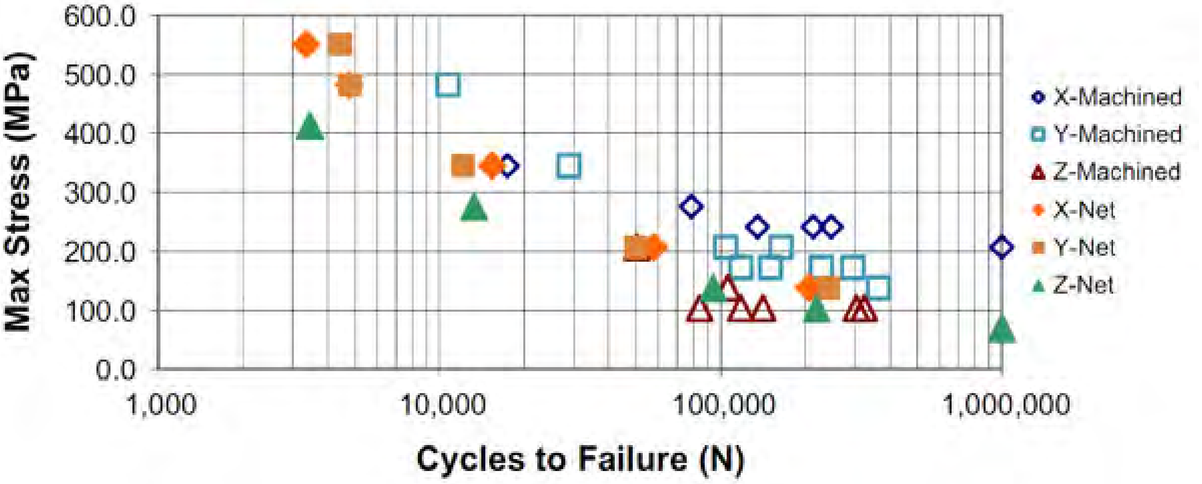

Figure 3-4: Fatigue S-N curves for both as-built and machined conditions of different build orientations [7]

In both Figure 3-4 and Table 3-3 it can be seen that that there is an effect on fatigue performance with respect to build orientation. This dependence is seen in both as-built and machined conditions. All specimens tested exhibited lower fatigue strengths for the target life cycles when compared to the wrought material under the same testing conditions. Edwards [7] goes on further to explain that the degree of scatter in the results is also affected by the build orientation where the profile height parallel to the x-axis has the tightest distribution and the profile height parallel to the y-axis has the largest scatter. Edwards [7] mentions that the differences found with respect to build orientation could be the result of porosity, microstructure and surface roughness although further investigation would be required.

3.4 Knowles (2012)

The work conducted by Knowles [1] was an MSc project conducted at the University of Cape Town. The scope of the project was to measure the residual stress in as-built SLM Ti-6Al-4V and investigate the effect of specific heat treatments on residual stress.

Specimens were manufactured in the EOSINT M270 machine which has been described in section 4.3.1. The method of detecting residual stress used was a stress relaxation hole drilling technique according to the ASTM E837 standard on cylindrical specimens. Four heat treatments were used: stress relief, recrystallization anneal, duplex anneal and beta anneal. For detailed explanations on the heat treatments and residual stress measurement results, refer to the work of Knowles [1]. A summarised version of results may be seen in Table 3-4.

Table 3-4: Heat treatments effect and their effect on the maximum principal residual stress levels [1]

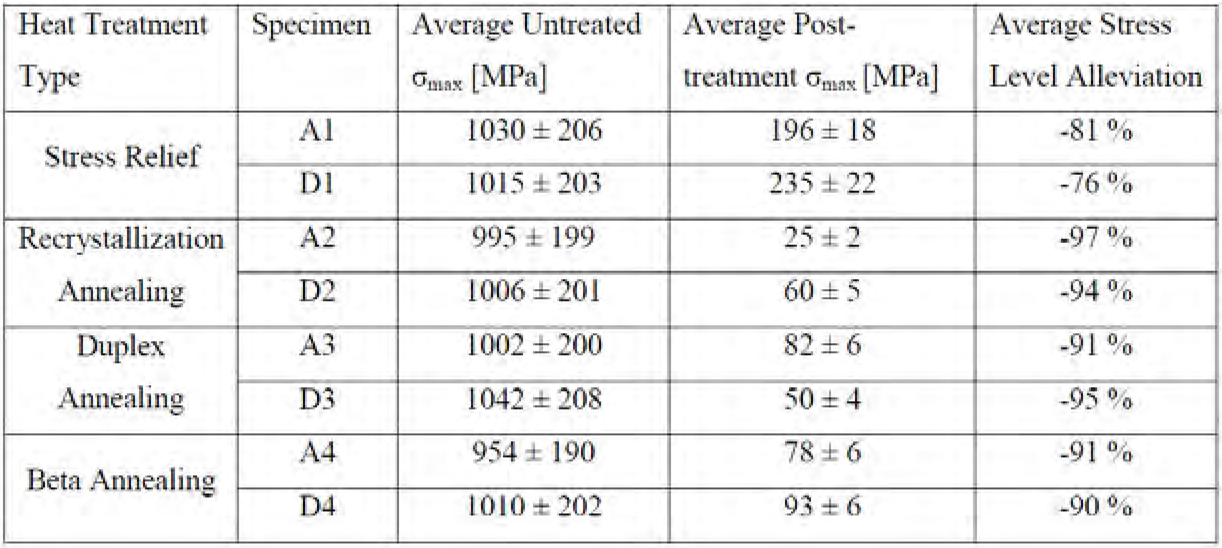

Heat Treatment Type	Specimen	Average Untreated σ_{max} [MPa]	Average Post-treatment σ_{max} [MPa]	Average Stress Level Alleviation
Stress Relief	A1	1030 ± 206	196 ± 18	-81 %
	D1	1015 ± 203	235 ± 22	-76 %
Recrystallization Annealing	A2	995 ± 199	25 ± 2	-97 %
	D2	1006 ± 201	60 ± 5	-94 %
Duplex Annealing	A3	1002 ± 200	82 ± 6	-91 %
	D3	1042 ± 208	50 ± 4	-95 %
Beta Annealing	A4	954 ± 190	78 ± 6	-91 %
	D4	1010 ± 202	93 ± 6	-90 %

Specimens A1-A4 were built in a vertical orientation and D1-D4 in a horizontal orientation. Slight differences in residual stress measurement are noticed between all specimens. Residual stress measurement took place at two locations on each specimen. Figure 3-5 and Figure 3-6 shows the residual stress profile, measured at two locations, before and after heat treatment for specimen A2 and D2.

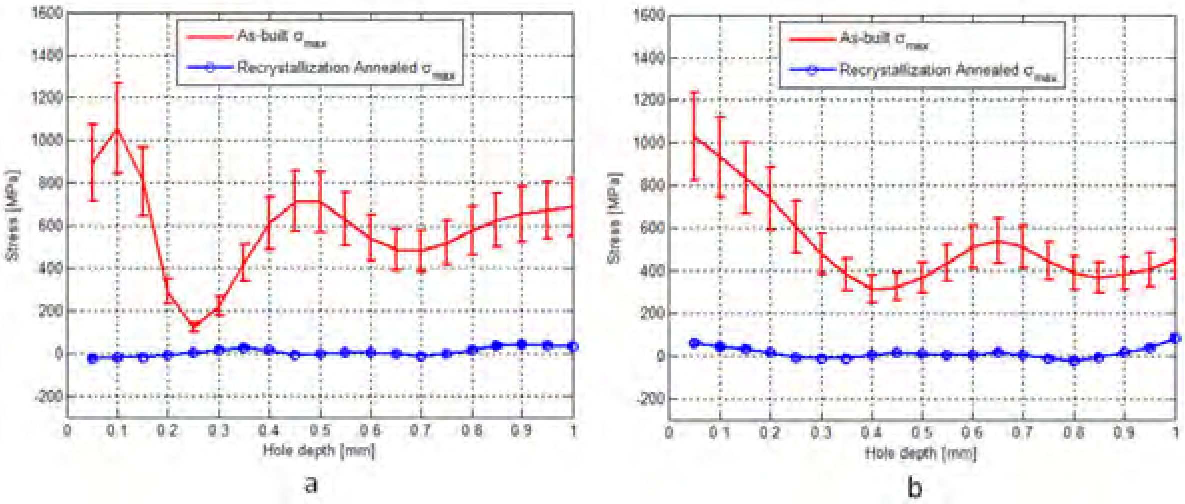

Figure 3-5: Effect of the recrystallization annealing on the maximum principal stress of specimen A2 at, a) Gauge position 1 and, b) Gauge position 2 [1].

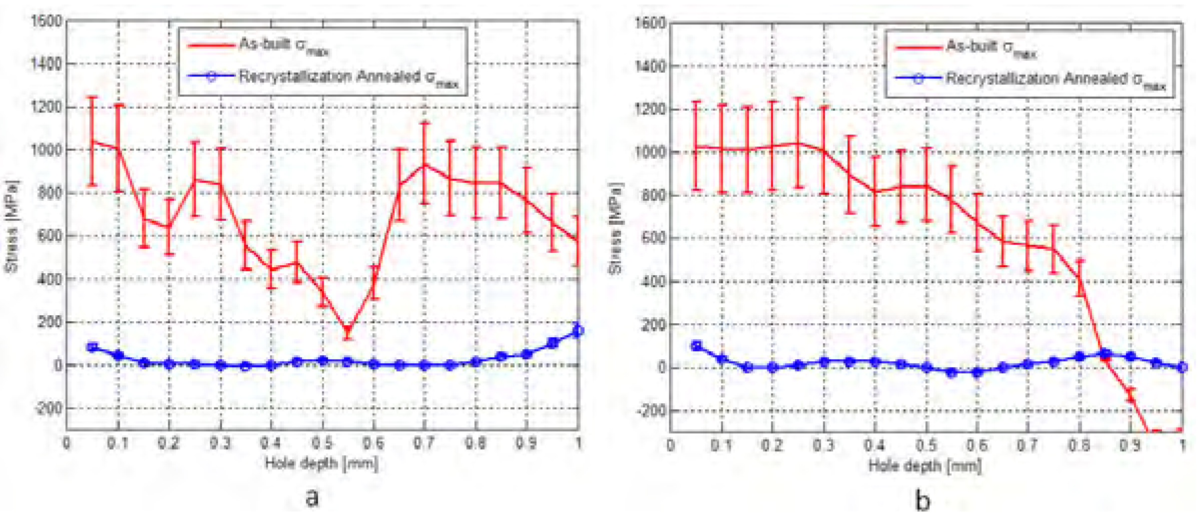

Figure 3-6: Effect of the recrystallization annealing on the maximum principal stress of specimen D2 at, a) Gauge position 1 and, b) Gauge position 2 [1]

The residual stress measurements show a highly non-uniform profile even when measured on the same specimen at different locations as well as for the different build orientations. Residual stresses are measured to be above 1000MPa which also exceeds the yield stress of the material. As can be seen in both figures, the heat treatments have a significant effect on the residual stress, relieving about 94-97% of the stress. It is worth mentioning as well that after heat treatment takes place, the new residual stress profile is far more uniform than before the heat treatment.

3.5 Comments on Relevant Studies

The initial crack growth rate and fracture toughness study that was conducted by Van Hooreweder [6] only looks at a single build orientation for as-built conditions. Further study on the crack growth rate and fracture toughness of SLM Ti-6Al-4V after the residual stress has been relieved along with more build orientations should be investigated. Literature on SLM Ti-6Al-4V fracture toughness is very limited and no other published work has been found apart from that of Van Hooreweder [6].

Leuders et al [5] conducted a study on fatigue and crack growth rate on SLM Ti-6Al-4V on one as-built, two heat treated and one HIPed conditions. The fatigue results showed a clear difference in the four different conditions. Crack growth rate testing was conducted using the same four conditions as the fatigue testing, but two different build orientations were used.

The as-built condition specimens performed well below the heat treated and HIPed specimens as well as conventional manufactured Ti-6Al-4V. This as-built crack growth rate result is in conflict with the work of Van Hooreweder [5], possibly due to manufacturing parameters. Even though crack growth rate testing was conducted on two build orientations, no explicit comparison between the two orientations was made. It can clearly be seen from Figure 3-2 and Figure 3-3 that there is a difference in the crack growth behaviour but this difference is not mentioned nor elaborated on. The heat treatments and HIPed processes used for the study do not mention the amount of stress that is actually relieved by these processes although this may be interpreted from the fatigue and crack growth rate results.

Edwards and Ramulu [7] consider the effect on fatigue with respect to build orientation. All specimens were in the as-built conditions with half of the specimens having their surfaces machined. There was no real significant difference between the as-built and surface machined specimens fatigue results. There was however a noticeable difference in the fatigue results with respect to build orientation. It is mentioned that the differences found with respect to build orientation could be the result of porosity, microstructure and surface roughness. Taking into account the work of Leuders et al [5] where different microstructures were obtained through the heat treatments and lower porosities obtained through the HIPed process, crack growth rate behaviour between build orientations still differed from each other. This suggest that the differences found with respect to build orientation may not be a result of porosities and microstructure but that one should possibly take the height of the specimen into account as well.

The investigation of Knowles's [1] work aims to measure and relieve the residual stress of SLM Ti-6Al-4V. The project was successful in terms of measuring the stresses before and after various heat treatments were conduct and in that way finding an optimal heat treatment for the reduction in residual stress. In the current study, one of Knowles's [1] heat treatments are used to relieve the residual stress before conducting fatigue and fracture toughness testing. This heat treatment will be discussed in the experimental procedure section of the project.

3.6 Summary

All of the studies dealt with SLM Ti-6Al-4V which have been manufactured under various parameters i.e. printing machine, scanning strategy, scanning speed, laser power etc.. This allows for one to analyse the experimental results for any similarities or differences between these studies, which may lead to a greater understanding of the effect of manufacturing parameters on mechanical properties on SLM Ti-6Al-4V. Specifically fatigue and fracture toughness for this current MSc project. Comments have also been made on these studies which indicate certain aspects which still need to be looked at or understood better especially with respect to the noticeable build orientation effects. The aspects which have been made mention in the comments will be discussed in Chapter 5 in which the aims of the project will be elaborated on.

Chapter 4 -Experimental Details and Procedures

The previous chapters provided the background information to the project and established the need for an experimental investigation of the fatigue crack growth rate and fracture toughness of SLM Ti-6Al-4V, with respect to build orientation. This chapter presents the experimental details, procedures and equipment required of the experimental aspect of this investigation.

4.1 Fatigue Crack Growth Rate Testing

The ASTM E647-13a provides the guidelines for determining fatigue crack growth rate behaviour of metallic materials. The rate of crack growth ranges from fatigue threshold, through the log-linear phase and right up until fast fracture. The crack growth rate testing in the standard describes the test method for growth rates both above and below 10^{-8} m/cycle. This thesis uses the ASTM E647-13a guideline and focuses on crack growth rates above 10^{-8} m/cycle.

4.1.1 Specimen Configuration

Figure 4-1 defines the standard dimensioning of the CT specimens as a function of specimen “width”, W. The specimens in this study for fatigue crack growth rate CT SLM Ti-6Al-4V investigations nominally had dimensions of W = 32 mm and thickness, B, 6.5 mm. The starter notch, a_n, with a nominal length of 6.5mm, was manufactured into the specimens during the SLM process. A detailed drawing of CT specimen geometry used in this thesis can be found in the relevant appendix.

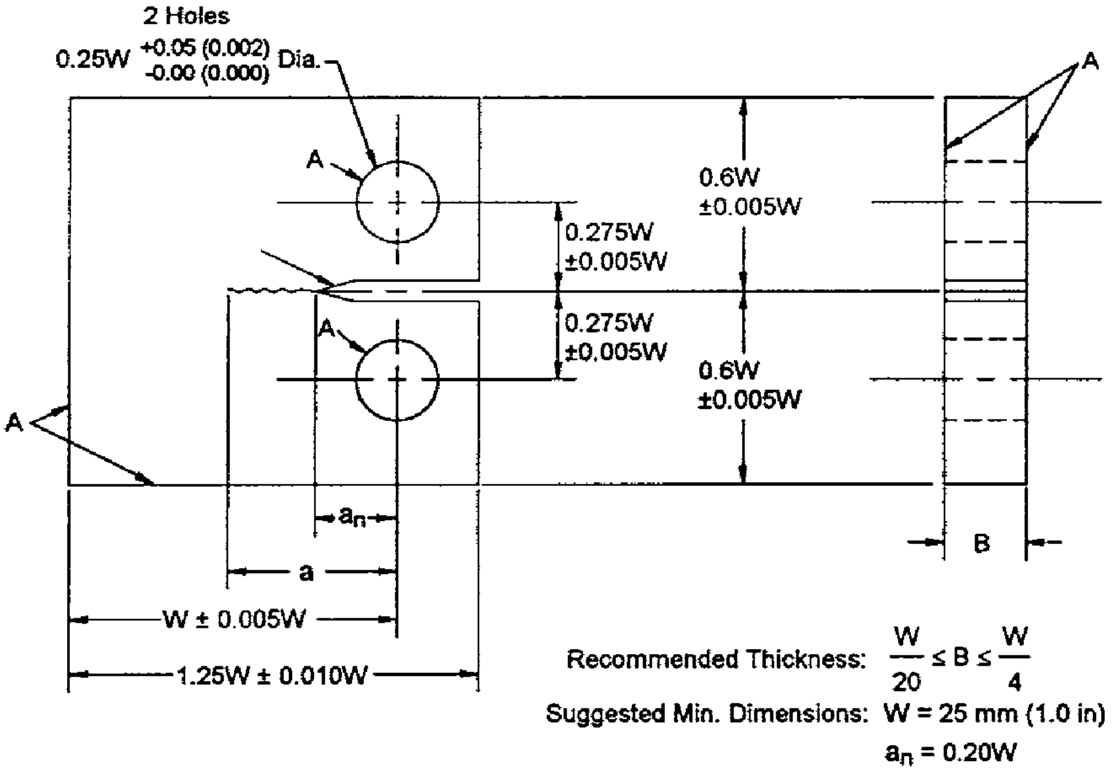

Figure 4-1: Standard CT specimen for fatigue crack growth rate testing [78]

4.1.2 Procedure

The procedure followed for conducting the fatigue crack growth rate testing is described in detail under the procedure section (section 8) in the ASTM E647-13a standard. The fatigue crack growth rate tests were conducted for three different build orientation, namely, the FLAT, VERTICAL and EDGE orientation (orientations will be described in section 4.4). For each orientation, four fatigue crack growth rate tests (a total of 12 tests) were conducted in which the results were plotted on a crack length (a) versus number of cycles (N) graph and crack growth rate (da/dN) versus cyclic stress intensity (ΔK) graph for analysis. All specimens had undergone a heat treatment, described in section 4.3.2, before testing which was conducted at room temperature on the universal ESH servo hydraulic fatigue machine.

A visual technique for measuring crack extension, Δa, was used to measure crack extensions at intervals of 0.25mm. A travelling microscope with a precision of 0.025mm was utilised to complete this task.

Apart from two tests, fatigue precracking was conducted at an initial cyclic SIF ranging between 12-15 MPa.m$^{0.5}$. The two tests, one FLAT specimen and one VERTICAL specimen, were conducted at cyclic SIF of approximately 7 MPa.m$^{0.5}$ in order to obtain low crack growth rates. The fatigue precracks were grown to 2 mm before any data was recorded, and no stepping down of forces was required for these tests. Scatter present in the raw experimental data of *da/dN* is reduced by using a three point moving average. An example of the moving average takes the form of:

$$\acute{a}_i = \frac{(a_{i+1} + a_i + a_{i-1})}{3}$$

Where the value of *ΔK* is computed using the "new" crack size, $\acute{a}_i$. Figure 4-2 illustrates one of the specimens used for fatigue crack growth rate testing.

Figure 4-2: Fatigue crack growth rate specimen in its final condition before testing.

The following list provides a summary of the relevant details about all the fatigue tests:

- The nominal width, W, of the specimen was 32mm
- The nominal thickness, B, was 6.5mm
- Visual crack monitoring technique with 0.025mm precision was employed

- The R-ratio (P_{min}/P_{max}) used was 0.1 with a sinusoidal waveform at 10Hz for precracking as well as the data collecting portion of the test.

The following table provides the overall experimental testing details of all the fatigue crack growth rate tests:

Table 4-1: The fatigue crack growth rate experimental details

Specimen	W (mm)	B (mm)	ΔP (kN)	Initial ΔK ($MPa.m^{0.5}$)
FLAT – 1	32.06	6.6	1.8	6.5
FLAT – 2	32.02	6.6	3.375	12.3
FLAT – 3	32.02	6.46	3.6	13.4
FLAT – 4	32.1	6.6	3.825	14
VERTICAL – 1	32.1	6.54	1.8	6.6
VERTICAL – 2	32.1	6.52	3.375	12.4
VERTICAL – 3	32.12	6.54	3.6	13.2
VERTICAL – 4	32.1	6.48	3.825	14.2
EDGE – 1	32.06	6.4	3.15	12
EDGE – 2	32.06	6.4	3.375	13
EDGE – 3	32.08	6.36	3.6	13.6
EDGE – 4	32.12	6.38	3.825	14.5

4.2 Fracture Toughness Testing

The ASTM E399 is the standard CT test that was undertaken for the linear-elastic plane-strain fracture toughness, K_{IC}, investigations.

4.2.1 Specimen Configuration

The fracture toughness specimens have similar dimensioning to that of the fatigue crack growth rate specimens where the W = 32 mm, however B = 16 mm. The required thickness of fracture toughness specimens is illustrated in Figure 4-3. The starter notch for these specimens was also manufactured via the SLM process and nominally has a length of 6.5 mm. A detailed drawing of the fracture toughness CT specimen geometry used in this thesis can be found in the relevant appendix.

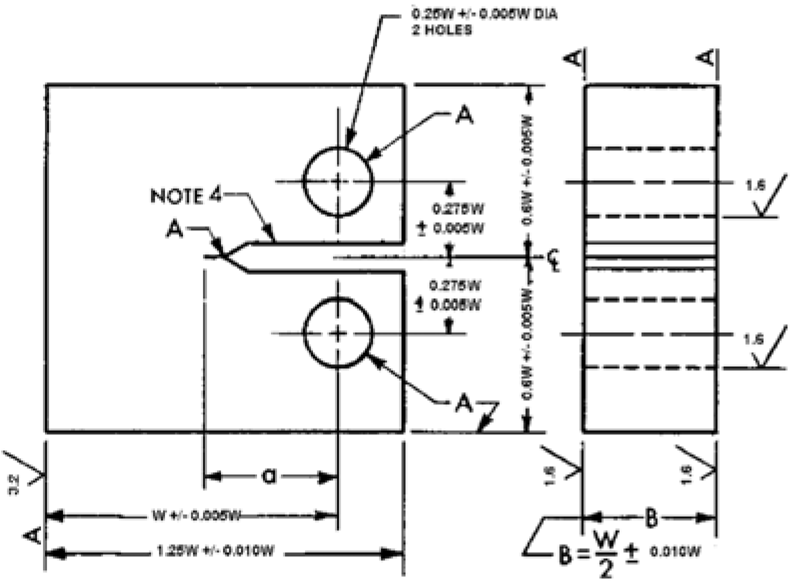

Figure 4-3: Standard CT specimen for fracture toughness testing [79]

4.2.2 Procedure

The procedure followed for conducting fracture toughness testing is described in detail in section 8 of the ASTM E399 - $12^{\varepsilon 3}$. A total of nine tests were conducted i.e. three per orientation and results plotted on a force vs. displacement graph. All testing was conducted on heat treated specimens, at room temperature, on the Instron retrofitted ESH servo hydraulic fatigue machine.

The following list provides relevant details about all the fracture toughness tests:

- The nominal width, W, of the specimen is 32mm
- The nominal thickness, B, is 16mm
- Crack initiation cyclic SIF ≈ 15 MPa.m$^{0.5}$
- Precrack extension ≈ 0.5 a/W
- Precracking conducted at R = 0.1 with a sinusoidal waveform at 10Hz
- Loading rate until fracture = 2 MPa.m$^{0.5}$/s

The following table provides the overall experimental testing details of all the fracture toughness tests:

Table 4-2: The fracture toughness experimental details

Specimen	W (mm)	B (mm)	ΔP (kN)	Initial ΔK (MPa.m$^{0.5}$)
FLAT – 1	32.08	16.24	9.9	14.3
FLAT – 2	32.14	16.16	10.35	15
FLAT – 3	32.08	16.12	9.9	14.7
VERTICAL – 1	32.14	16.04	9.9	14.8
VERTICAL – 2	32.12	16.04	9.9	14.6
VERTICAL – 3	32.14	16.02	9.9	14.8
EDGE – 1	31.98	16.08	9.9	14.6
EDGE – 2	31.94	16.1	9.9	14.3
EDGE – 3	31.96	16.06	9.9	14.4

4.3 Specimen Details

All the Ti-6Al-4V specimens were manufactured at the Centre for Rapid Prototyping and Manufacturing (CRPM) at the Central University of Technology (CUT) in Bloemfontein. A total of 21 specimens were used for this thesis consisting of 12 fatigue crack growth specimens and 9 fracture toughness specimens. Both the fatigue and fracture toughness specimens were divided into four and three specimens per a build orientation respectively i.e. three build orientations which may be seen in Figure 4-4.

Information regarding the chemical composition as well as powder particle size is regarded as private information and thus cannot be mentioned within this dissertation.

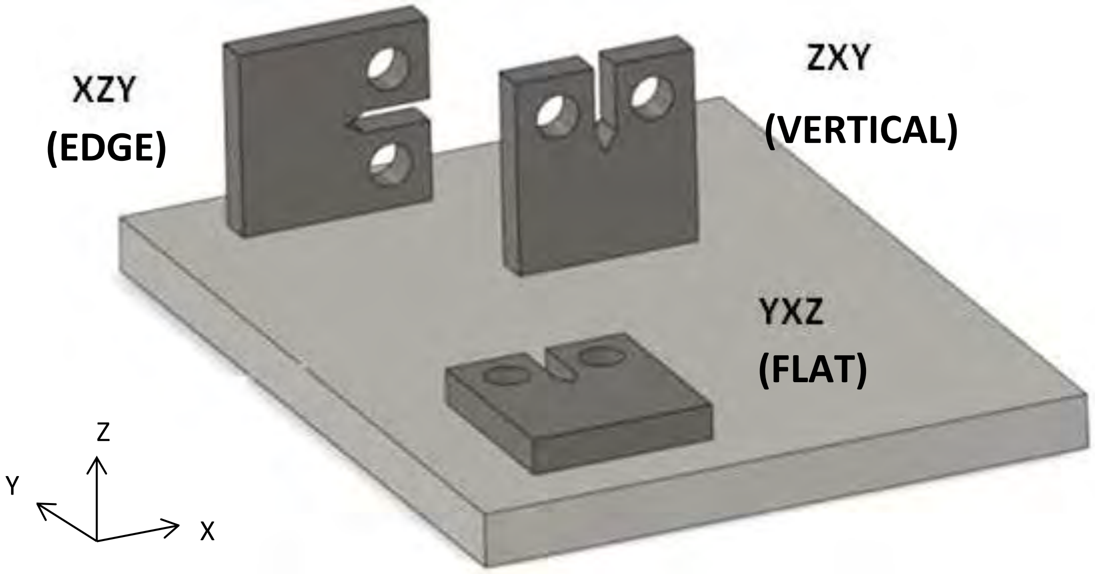

Figure 4-4: Build orientation of CT specimens with the build direction perpendicular to the base plate.

When dealing with AM technologies such as SLM, there is a standard manner in which the specimens build orientation is termed which is given in the ASTM F2921 – 11 standard terminology for additive manufacturing – coordinate systems and test methodologies. Figure 4-5 illustrates the build orientation notations.

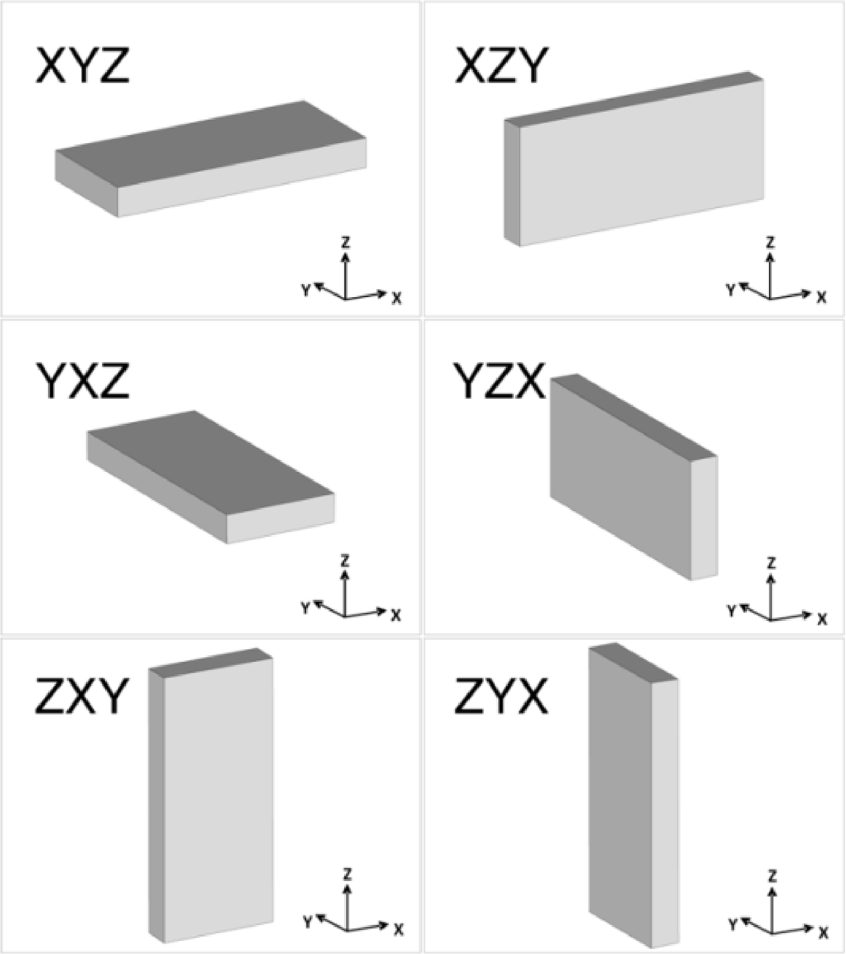

Figure 4-5: Build orientation notation for various build orientations [80].

The manner in which the notation works is by designating the axis which is parallel to the longest length first, followed by the axis which is parallel to the second longest length and the axis parallel to the shortest length goes last. This thesis uses the orientation known as YXZ, ZXY and XZY which will be referred to as the FLAT, VERTICAL and EDGE orientation respectively. To further describes these orientations with respect to crack growth:

- The FLAT orientation has a crack grown perpendicular to build direction, in the ZY plane
- The VERTICAL orientation has a crack grown parallel to the build direction, in the YZ plane
- The EDGE orientation has a crack grown perpendicular to build direction, in the XY plane

With regards to the specimen build orientation, ideally, there should be six different orientations, as seen in Figure 4-6. However, the three orientations mentioned above are sufficient and account for orientation effects due to the SLM manufacturing process. During the SLM process (specific to this project), a multidirectional scanning strategy is used. This means that for every layer of powder material, the laser scans over the material at an angle different to that of the previous layer of material. If the xy plane in Figure 4-7 were to be rotated about an axis normal and at the centre of the xy plane, it would not affect the product as it is still being built up to the same height with the same scanning strategy. Likewise, if one were to consider the illustration in Figure 4-6 to be manufactured via the SLM process where the short transverse direction is the build direction, specimen orientation T-S and L-S may be considered to be the same. This is because for the T-S and L-S orientation, the cracks interaction with build layers will be the same. The orientations may be described as follows:

- The FLAT orientation considers both T-L and L-T orientations
- The VERTICAL orientation considers both T-S and L-S orientations
- The EDGE orientation considers both S-T and S-L orientations

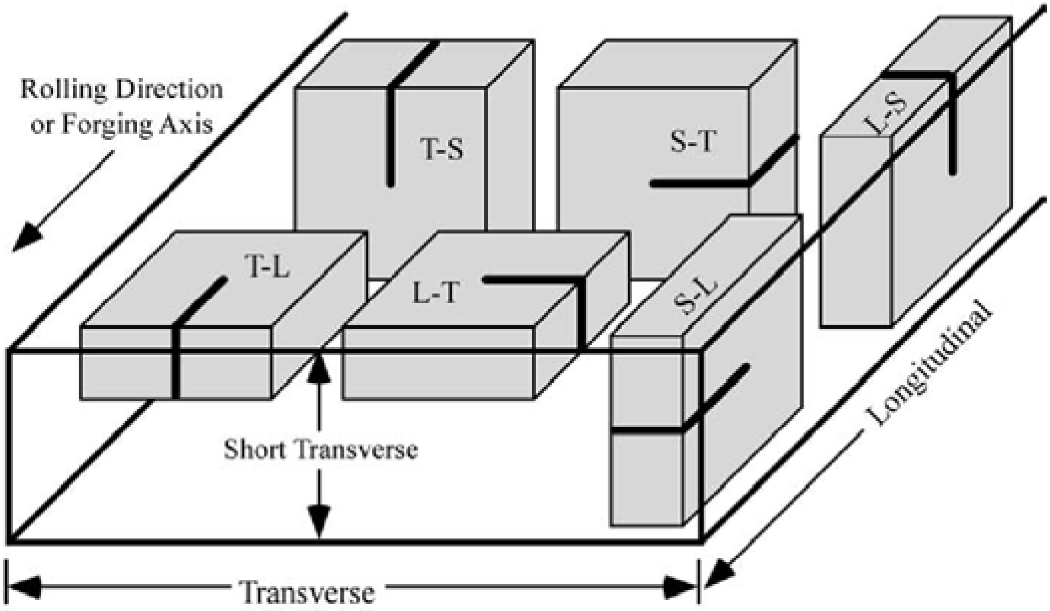

Figure 4-6: ASTM notation extracted from rolled plate and forgings [65]

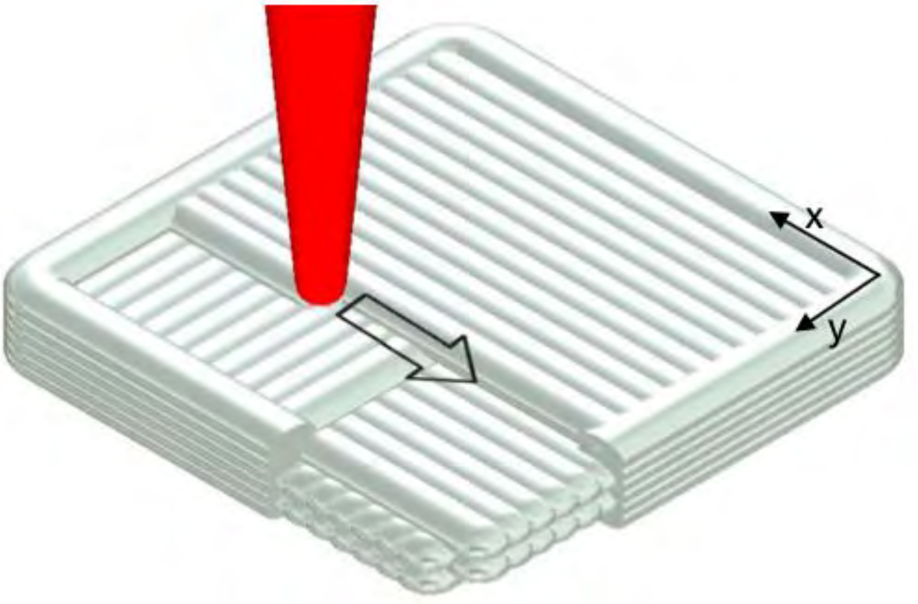

Figure 4-7: A multidirectional scanning strategy [81]

The purpose for testing the material in these three different orientations is to observe whether there exists an anisotropic behaviour. There is a very little published research, if any, on the FLAT orientation for fatigue crack growth rate testing while the VERTICAL and EDGE has very little mentioned on it about any orientation dependencies [5], [7]. Furthermore, to date, no fracture toughness testing with respect to build orientation has been found in literature.

4.3.1 Three Dimensional Laser Printer – EOSINT M270

The EOSINT M270 uses the DMLS consolidation method to produce a part. A focussed laser beam fuses metal powder using a 200W Yb-fibre laser with a multidirectional scanning strategy, controlled via computer software producing a part directly from a 3D CAD model without requiring any tooling [82]. This printer has the capabilities to process a variety of metal powders such as aluminium alloys, maraging steel, stainless steel as well as novel alloys developed by EOS [82]. However, this research project focuses on the consolidation of Ti-6Al-4V metal powder. Ti-6Al-4V powder used in the EOS printers meet the requirements of the ASTM 1472 standard for maximum concentration of impurities [83]. Further technical data such as build speed, scan speed, laser diameter etc. may be found in Figure 4-8. The EOSINT M270 can fuse metal powder by sintering or melting in a similar manner to SLS and

SLM respectively. SLS and SLM are more commonly known terms used for such forms of consolidation and so for the remainder of the report, the consolidation of Ti-6Al-4V by the EOSINT M270 printer will be referred to as SLM.

It should be noted that no specifics regarding the scanning strategy were supplied by EOS nor could be found in literature. The suppliers at CUT have mentioned that standard settings are used, which they have been able to estimate, but regard it as private information.

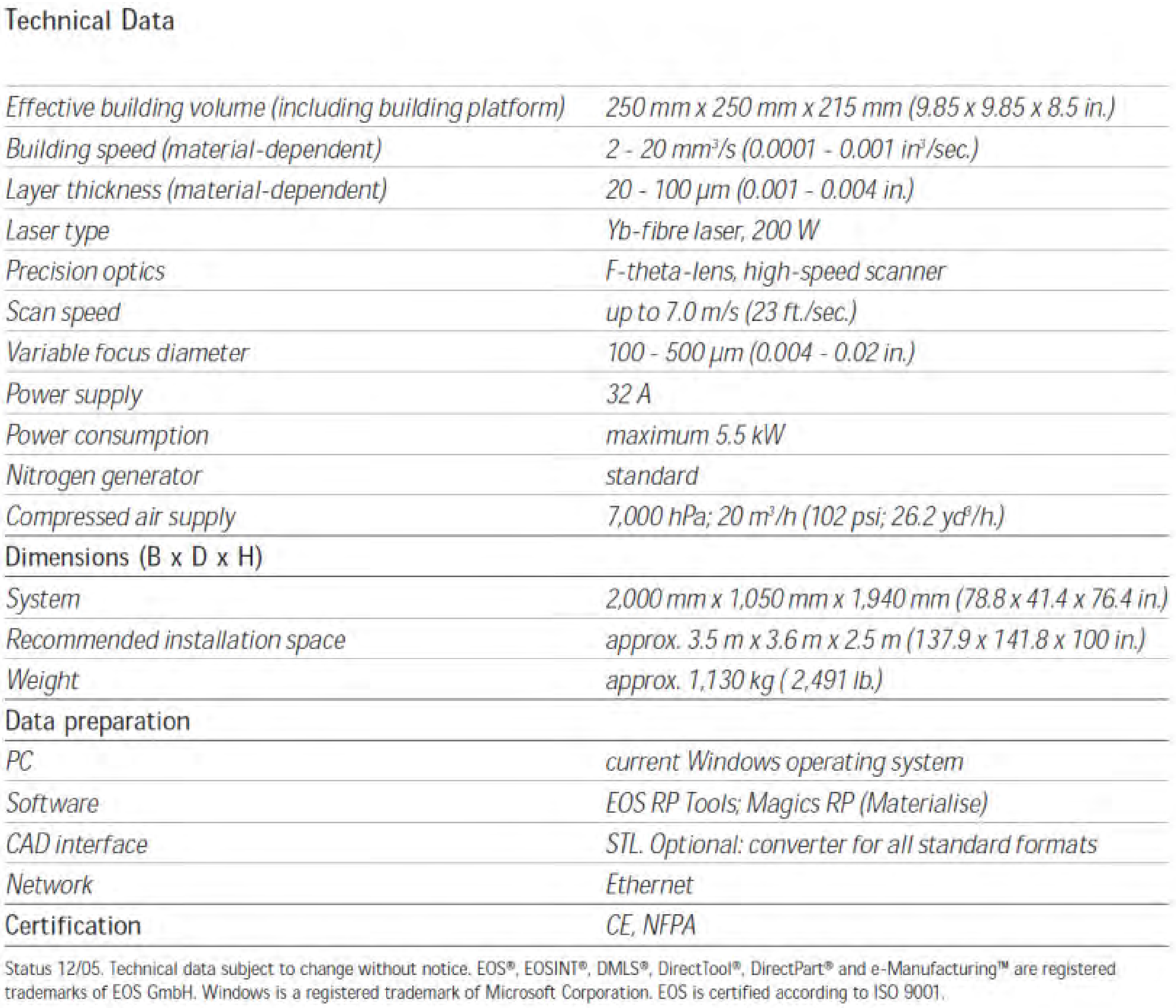

Technical Data

Effective building volume (including building platform)	*250 mm x 250 mm x 215 mm (9.85 x 9.85 x 8.5 in.)*
Building speed (material-dependent)	*2 - 20 mm^3/s (0.0001 - 0.001 in^3/sec.)*
Layer thickness (material-dependent)	*20 - 100 µm (0.001 - 0.004 in.)*
Laser type	*Yb-fibre laser, 200 W*
Precision optics	*F-theta-lens, high-speed scanner*
Scan speed	*up to 7.0 m/s (23 ft./sec.)*
Variable focus diameter	*100 - 500 µm (0.004 - 0.02 in.)*
Power supply	*32 A*
Power consumption	*maximum 5.5 kW*
Nitrogen generator	*standard*
Compressed air supply	*7,000 hPa; 20 m^3/h (102 psi; 26.2 yd^3/h.)*
Dimensions (B x D x H)	
System	*2,000 mm x 1,050 mm x 1,940 mm (78.8 x 41.4 x 76.4 in.)*
Recommended installation space	*approx. 3.5 m x 3.6 m x 2.5 m (137.9 x 141.8 x 100 in.)*
Weight	*approx. 1,130 kg (2,491 lb.)*
Data preparation	
PC	*current Windows operating system*
Software	*EOS RP Tools; Magics RP (Materialise)*
CAD interface	*STL. Optional: converter for all standard formats*
Network	*Ethernet*
Certification	*CE, NFPA*

Status 12/05. Technical data subject to change without notice. EOS®, EOSINT®, DMLS®, DirectTool®, DirectPart® and e-Manufacturing™ are registered trademarks of EOS GmbH. Windows is a registered trademark of Microsoft Corporation. EOS is certified according to ISO 9001.

Figure 4-8: EOSINT M270 technical data [82]

4.3.2 Specimen Preparation

Once the specimens have been received, the inherent residual stress needs to be relieved first as any other machining process could damage the specimen due to the high residual stress. The heat treatment followed was the duplex anneal investigated by Knowles [1]. Before the heat treatment occurs, the specimens need to be coated with ceramic slurry to prevent any significant oxidation. A Kiln Contracts HTF 028 box furnace was used as this allowed for air cooling after each annealing process.

Figure 4-9 illustrates the duplex annealing time–temperature process.

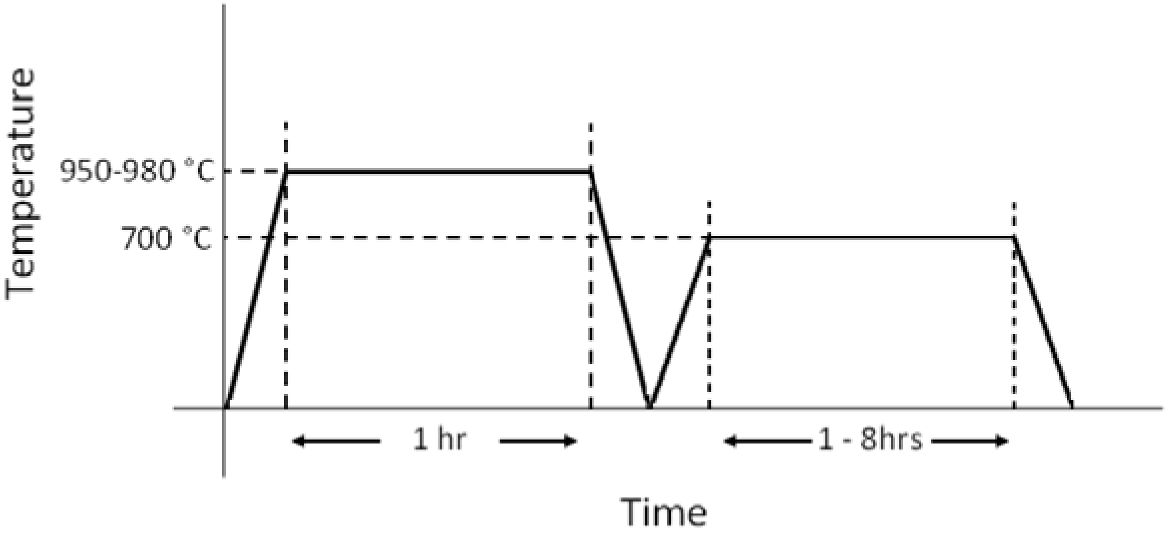

Figure 4-9: Duplex annealing process [1].

The details of the duplex anneal is as follows:

- Heating rate of 630°C/hour
- First annealing temperature - 950°C for one hour
- Second annealing temperature - 700°C for two hours
- Both cooling processes are air cools

After the heat treatment has been completed, the specimens have minor post manufacture machining on them to make sure all dimensions are within the tolerances given in the ASTM E399 and E647 standard. The machining takes place at the UCT mechanical engineering workshop.

Since the crack growth monitoring system will be that of a visual technique, the surface of specimen is required to have a mirror like finish to be able to monitor a crack with the correct lighting conditions. In order to obtain the desired surface finish, the specimen was surface ground by hand using P80 sand paper and incrementally increasing the fineness of the sand paper until P2400 was reached. Only the portion of the specimen in which the crack path would lie was polished. As is suggested in the ASTM E647 standards, reference markings were made along the crack path in 1mm increments.

4.5 Testing Equipment

Fatigue crack growth rate and fracture toughness testing was conducted on a retrofitted 50kN ESH servo hydraulic machine which is operated using instron software. The machine uses a feedback system where the servo-controller compares the input command with the measured performance to give an error which will then be corrected by the servo-valve to adjust the actuator movement accordingly [84]. The control mechanism of the machine may be operated via load, position or strain control, however, only load control was used for this thesis. The ESH machine may be seen in Figure 4-10.

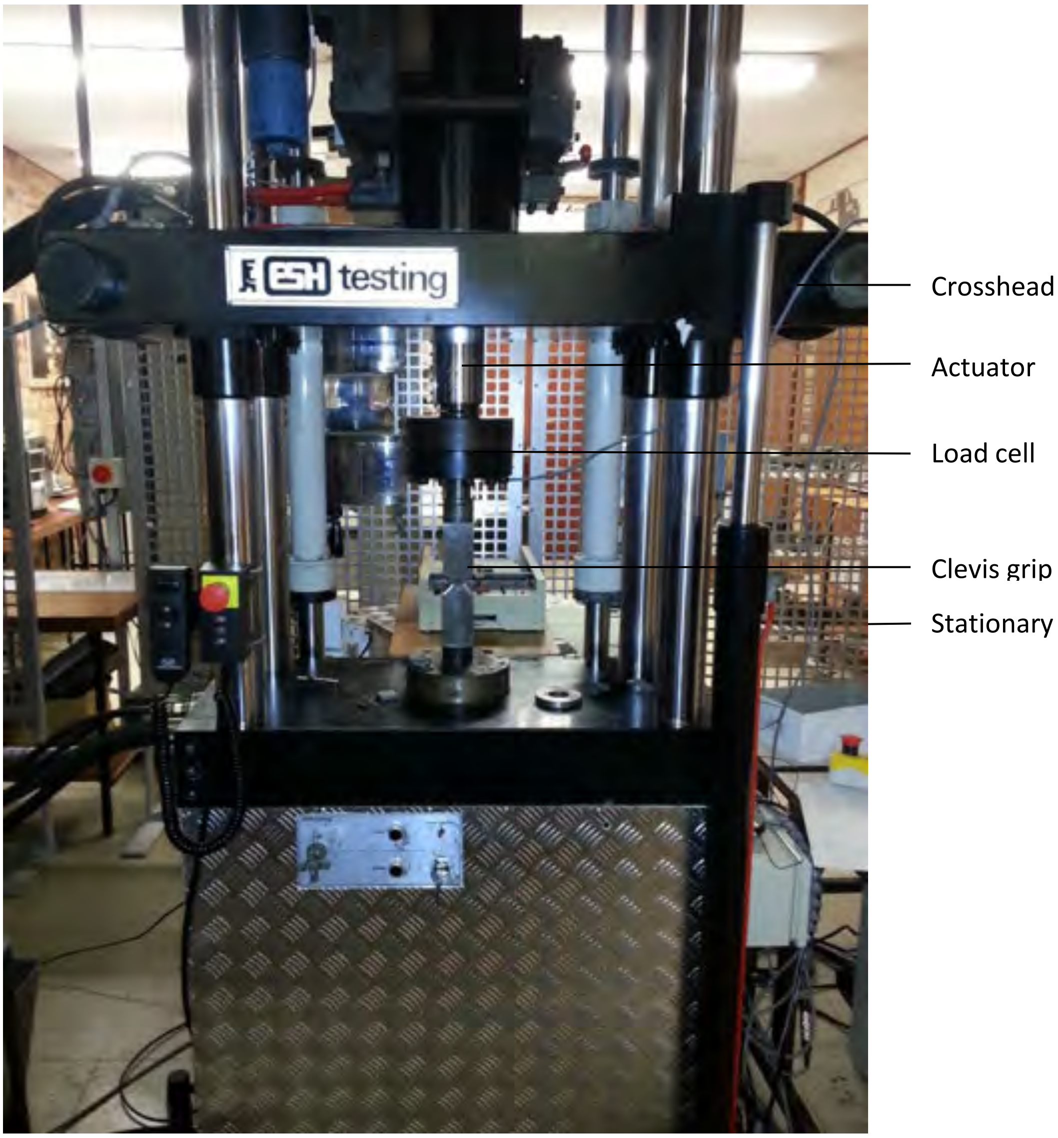

Figure 4-10: ESH machine used for fatigue and fracture toughness testing.

There is an approximated 100mm travel in the actuator of the machine. For the ESH machine operation, it requires its response-system (control loop tuning) to be adjusted for a specific material. This is as different material will have various degrees of stiffness and therefore the response from the machine needs to differ for various materials. The common PID gain (propotional-intergral-derivatve) parameters are used to adjust the speed of response, phase advancement and steady state errors. Overall, the PID gain allows for the measured output on the test piece to be adjusted so that it matches the demand signal output. In this case, the demand signal output is a sinusoidal wave of specific amplitude with a frequency of 10Hz. However, since the test piece is experiencing a 10Hz sinusoidal wave (after PID adjustment), the phase difference between the demand signal output and measured output on the test piece is not of concern. Once the ESH machine's control loop system is tuned correctly for the Ti-6Al-4V and grip system, the error feedback given by the software, which compares the measured output with the command input, was kept below 1% with a ±0.5% error on the reading.

Figure 4-11: Clevis grips used for fatigue and fracture toughness testing.

For the fatigue crack growth rate testing, the results obtained directly from using the ESH machine along with the instron software is the crack extension and the number of cycles per crack extension. These results are then manipulated to form the Paris curve and obtain the Paris equation thereof, according to the ASTM E647.

The ESH machine along with the instron software outputs the force and crack mouth opening displacement experienced throughout the fracture toughness tests. The force and crack mouth opening displacement is then analysed according to the ASTM E399 $-12^{\varepsilon 3}$ in order to determine K_{IC}.

4.6 Microscopy Preparation

A BUEHLER IsoMet low speed micro-slicer which uses a diamond tipped blade was used to cut a small piece of the specimen to analyse. This slicer was used as it does not raise the temperature of the specimen when being cut and so does not distort the testing condition microstructure. The cut specimen is then mounted in resin using the Struers LaboPress- 3 hot mounting system which heats up and compresses the resin. Thereafter the mounted specimen is polished using the Struers TegraPol-11 automatic polisher which uses the following sequence for polishing:

- Dur pad using 9µm diamond paste for 10 minutes
- Chem pad using OP solution for 10 minutes
- Nap pad using water for 5 minutes

After the polishing process has been completed, the specimen may now be etched to remove the surface layer of the material and expose the microstructure for the desired analysis. Kroll’s reagent was used with the composition given in Table 4-3.

Table 4-3: Kroll’s reagent used for sample etching

Composition	Concentration	Etching Duration
Distilled Water	50 ml	2-5 seconds
HNO_3	25 ml	
HF	5 ml	

The outcome of this work is so that one may make a basic analysis of what the as-built microstructure is, the grain boundary direction with respect to build orientation as well as a top, side and front view of the specimen’s microstructure. Furthermore, to view the microstructure of the specimens after the duplex anneal heat treatment has taken place and its interaction with the fatigue crack.

4.7 Density Testing

The density testing method that was performed followed the method described in the ASTM B311 – 08 standard test method for density of powder metallurgy (PM) materials containing less than two percent porosity. This method is based on the Archimedes principal of water displacement. A Sartorius Quintix® density testing kit, which has a readability of 0.1mg, was used to conduct the tests. The method of calculating the density is as follows:

- The specimen was weighed in air, given the parameter A
- The mass of the support stand, test specimen support and beaker filled with distilled water as measured and given the parameter C
- The specimen is placed into the test specimen support within the distilled water and the mass was measured and given the parameter B
- The water temperature is measured and obtain the density of the water at the recorded temperature from the tables given in the ASTM B311
- The density of the specimen may be calculated according to the following equation:

$$\rho_{specimen} = \frac{A}{\rho_{water}(A-B+C)} \tag{4-4}$$

The mass of each specimen was measured three times over and the average was used in calculations. The density of the SLM products of this project is compared to that of the full density of Ti-6Al-4V quoted at 4,43 g.cm^{-3} [8]. Half of a fractured fatigue specimen was used to measure the density as seen in Figure 4-12.

Figure 4-12: Specimen used in density test

4.8 Summary

This chapter has described the experimental techniques required in this study to evaluate the fatigue crack growth rate and fracture toughness of SLM Ti-6Al-4V. The methods used to conduct these tests followed the ASTM E647 and E399 standards. The details of the specimens were then discussed as well as the preparations of the specimens in order for the testing to be conducted according to the ASTM standards. The heat treatment of choice to relieve the residual stress was discussed. The 50 kN ESH fatigue machine which is used to conduct both fatigue crack growth rate testing as well as the fracture toughness testing was briefly described as well as the general precautions required to operate the machine. The procedure on how the microstructural analysis and density testing were done have been discussed. The following chapter discusses the results obtained from all the experimentation.

Chapter 5 – Results

This chapter presents the experimental results, including crack growth rate with respect to build orientation along with the microstructural analysis and density testing of specimens. The chapter then presents fracture toughness results and the validity of the results. Chapter 6 discusses the findings for the crack growth rate and fracture toughness testing with respect to build orientation.

5.1 Fatigue Crack Growth Rate Testing

5.1.1 FLAT Orientation

Figure 5-1 and Figure 5-2 display the crack length vs. number of cycles results for all four specimens in the FLAT (YXZ orientation). Specimen FLAT – 1 has been plotted on its own graph as it has the largest cycles to failure of this orientation. This leads it to have a scale too large for the rest of the specimens to be plotted on the same graph.

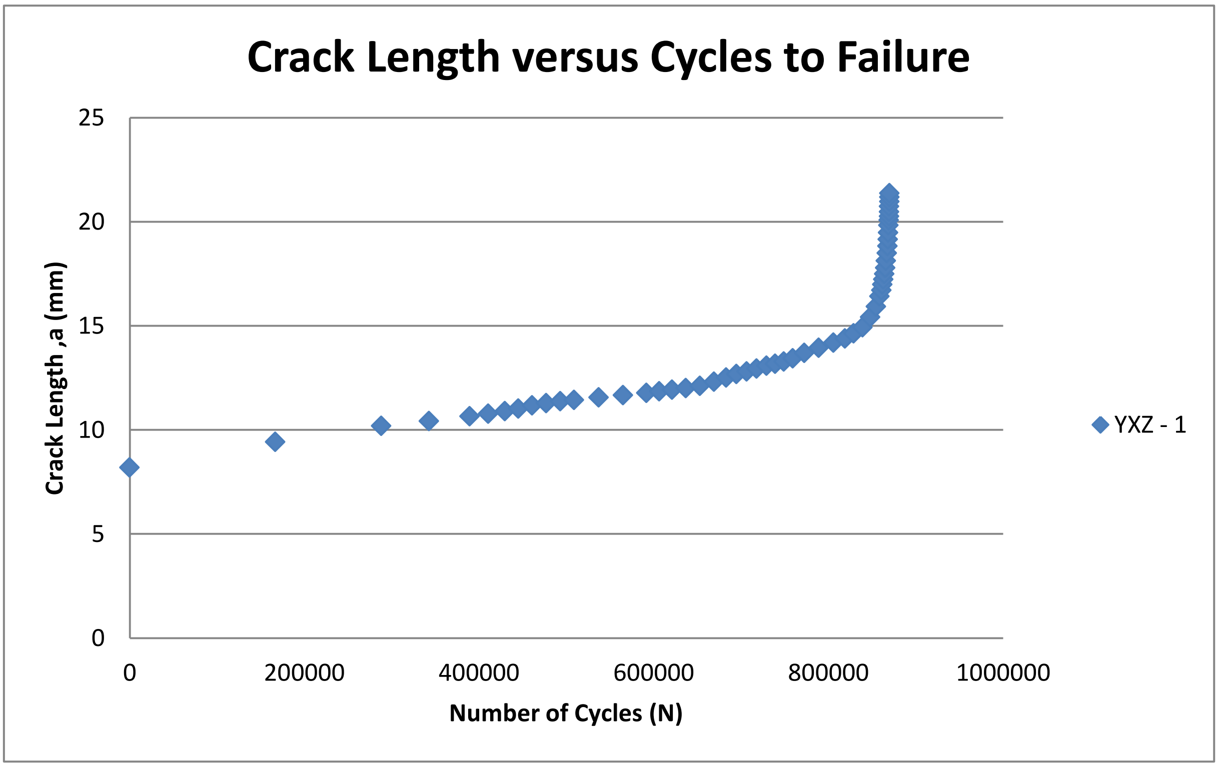

Figure 5-1: Crack length versus cycles to failure graph for specimen FLAT – 1.

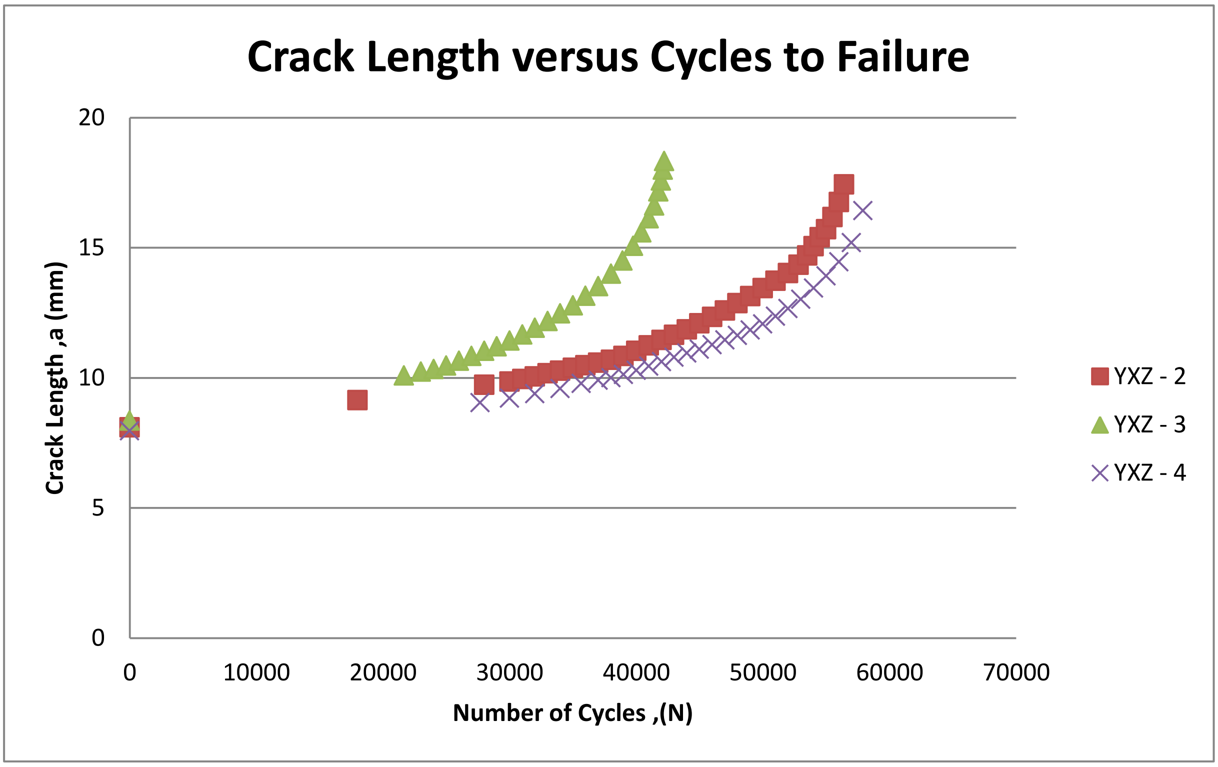

Figure 5-2: Crack length versus cycles to failure graph for specimen FLAT – 2, 3, and 4.

Figure 5-3 represents the linear region II of the crack growth rate curve which is also known as the Paris regime. It would be expected that one would obtain significantly low crack growth rates for specimen FLAT – 1 (YXZ – 1), as it was tested at the lowest cyclic SIF. However, when analysing the fatigue crack growth rate data, significantly large scatter was present in crack growth rates between 10^{-8} and 10^{-7} m/cycle, even after data reduction, when compared to that above 10^{-7} m/cycle. Thus it was decided, for this orientation, to only present the Paris regime for cyclic SIF's above 20 MPa.$m^{0.5}$.

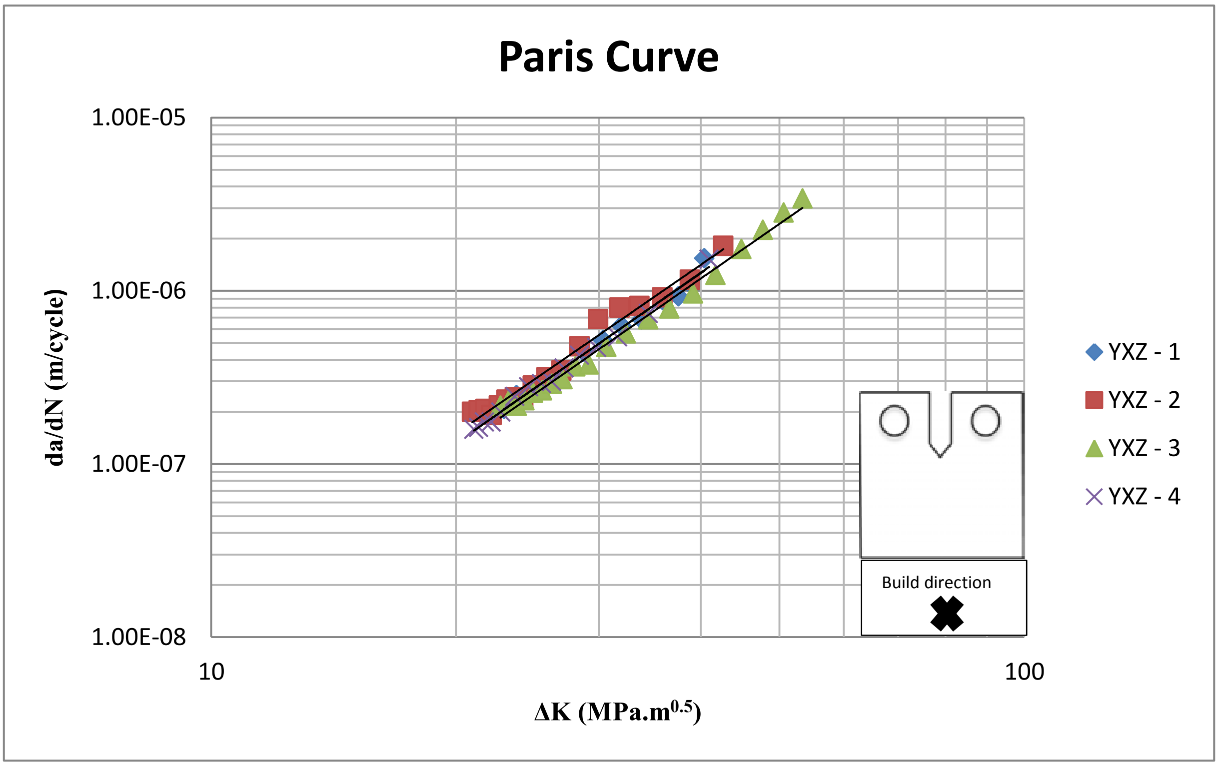

Figure 5-3: Fatigue crack growth rate (Paris regime) curve for specimens FLAT – 1, 2, 3 and 4.

The four FLAT samples had the most stable fatigue crack growth rate behaviour (low amounts of scatter) of all the orientations and displayed excellent repeatability in the results, as can be seen by the Paris equations in Table 5-1. It must be noted that for this orientation tested, stable crack growth behaviour (scatter plus linearity) occurred approximately from a cyclic SIF of 20 MPa.m$^{0.5}$ onwards and fast fracture, in most cases, occurred below 50 MPa.m$^{0.5}$. The Paris regime curve is quantified into the Paris equation, which may be used for life prediction estimations, as seen in Table 5-1.

Table 5-1: Paris equations for specimens FLAT – 1, 2, 3 and 4

Specimen	Paris Equation
FLAT – 1	$\frac{da}{dN} = (8.03 \times 10^{-12})\Delta K^{3.24}$
FLAT – 2	$\frac{da}{dN} = (9.31 \times 10^{-12})\Delta K^{3.23}$
FLAT –3	$\frac{da}{dN} = (7.03 \times 10^{-12})\Delta K^{3.26}$
FLAT – 4	$\frac{da}{dN} = (7.42 \times 10^{-12})\Delta K^{3.27}$
Average	$\frac{da}{dN} = (7.95 \pm 0.99) \times 10^{-12}\Delta K^{3.25 \pm 0.01}$

5.1.2 VERTICAL Orientation

Specimen VERTICAL – 1 was tested at the lowest loading condition of all specimens in this orientation. This low load testing condition (below a cyclic SIF of 7 MPa.m$^{0.5}$) had also produced large scatter at low crack growth rates, but stability (scatter plus linearity) occurred from approximately 18 Mpa.m$^{0.5}$ while fast fracture occurred above 50 MPa.m$^{0.5}$. All specimens within this orientation produced significant amounts of scatter up until approximately 18 Mpa.m$^{0.5}$. Thus it was decided, for this orientation, to only present the Paris regime for cyclic SIF's above 18 MPa.m$^{0.5}$. Crack length versus number of cycle's to failure is displayed in Figure 5-4 and Figure 5-5 below as well as the Paris curve in Figure 5-6.

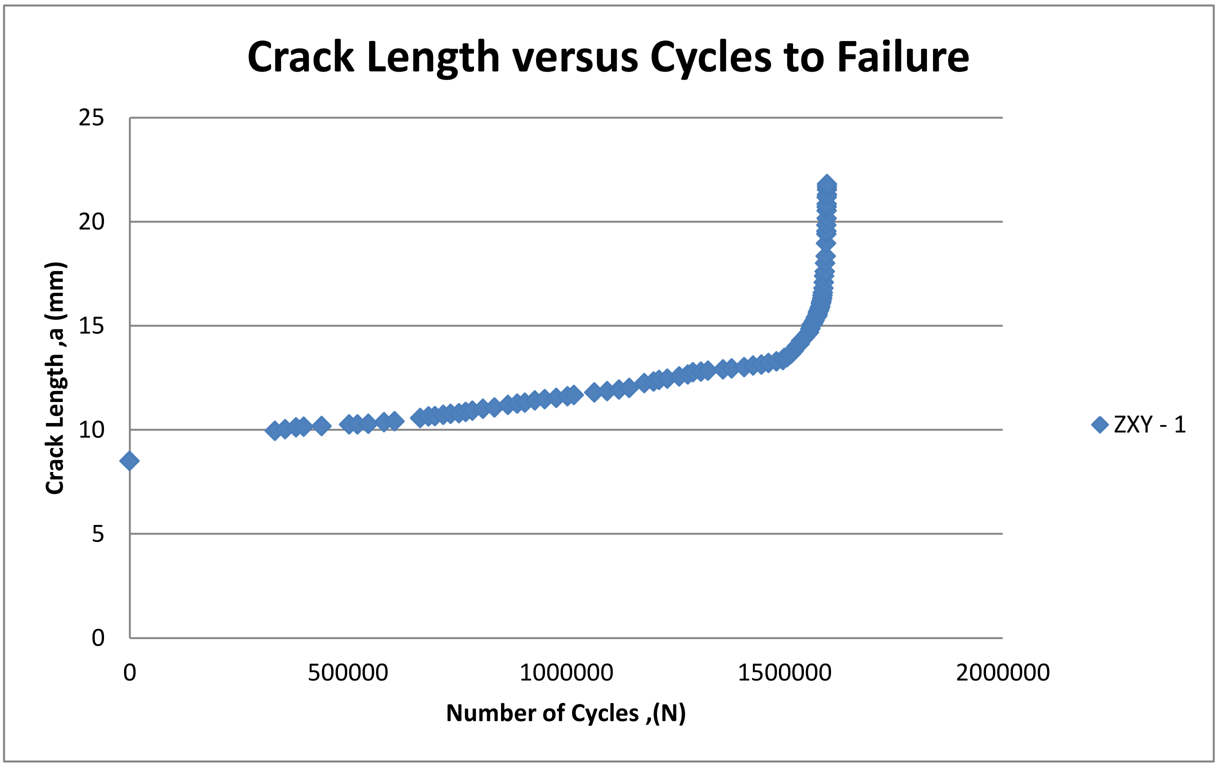

Figure 5-4: Crack length versus cycles to failure graph for specimen VERTICAL – 1.

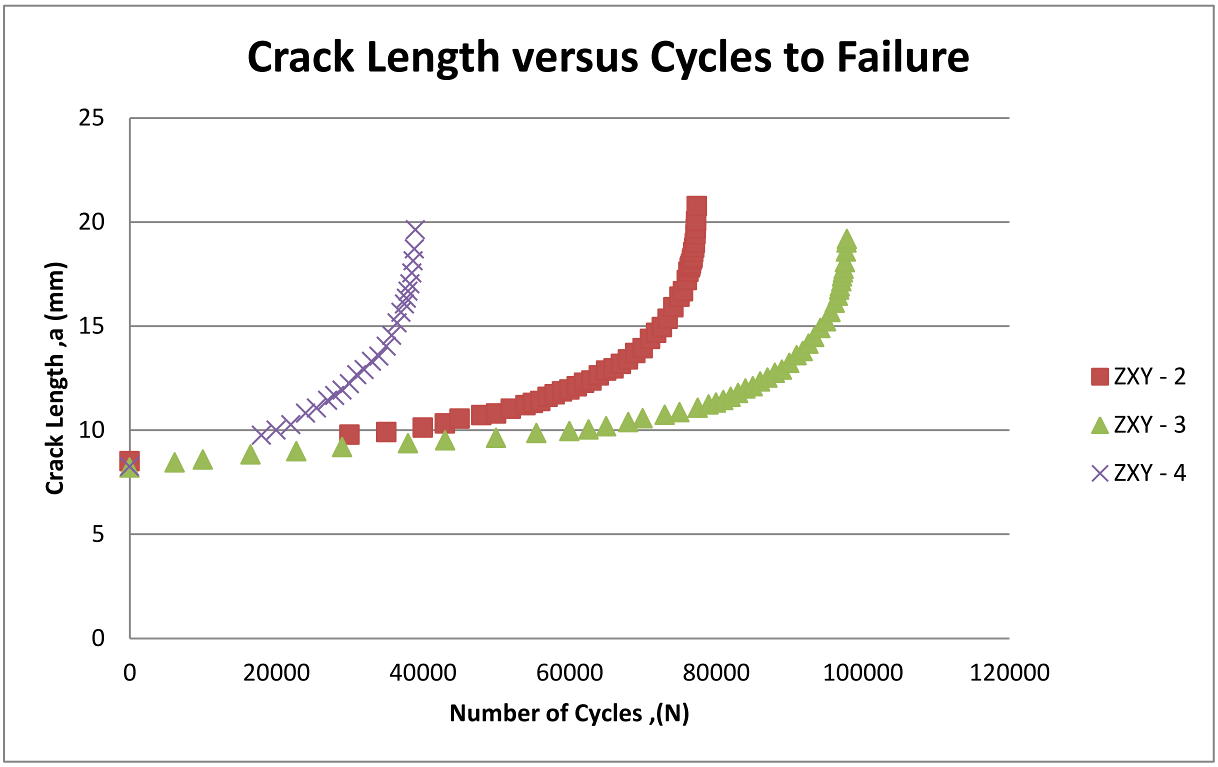

Figure 5-5: Crack length versus cycles to failure graph for specimen VERTICAL – 2, 3, and 4.

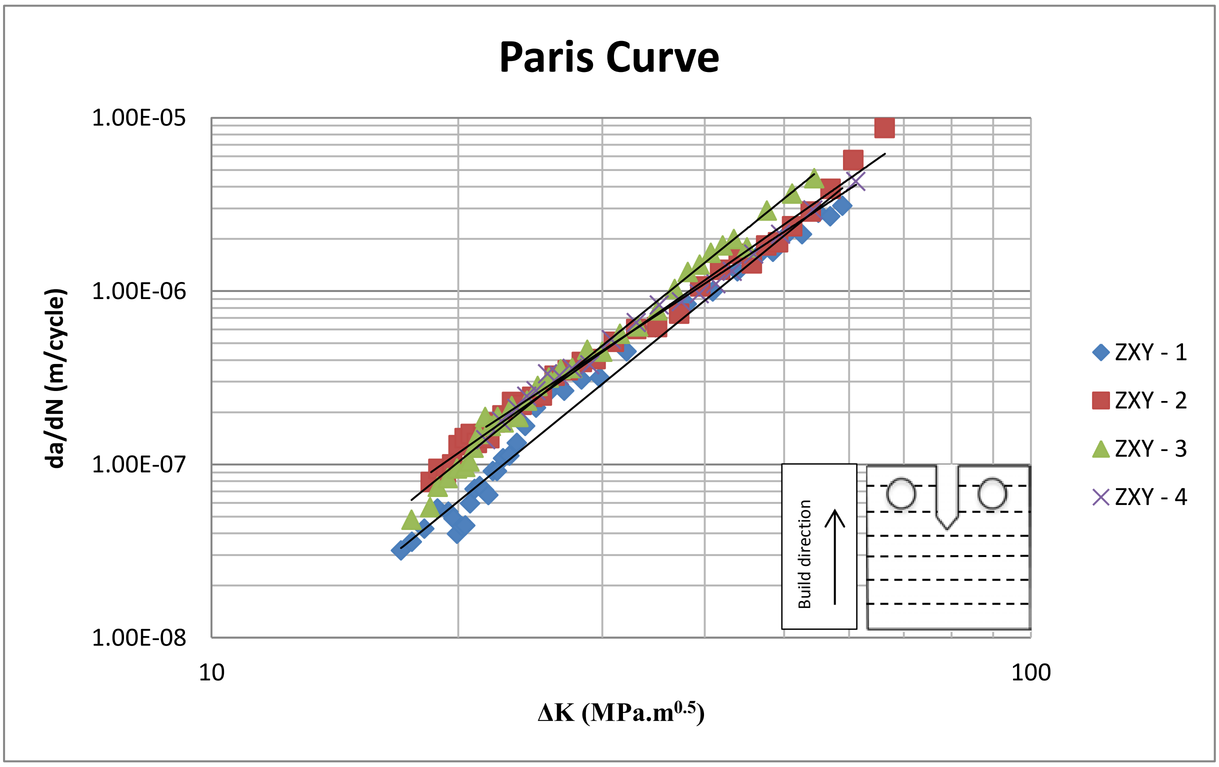

Figure 5-6: Fatigue crack growth rate (Paris regime) curve for specimens VERTICAL – 1, 2, 3 and 4.

There was a noticeable difference in the fatigue crack growth rate behaviour between the VERTICAL and FLAT specimens. Firstly, the VERTICAL specimens did not have an as stable crack growth behaviour (i.e. larger scatter) as the FLAT specimens, as seen in Figure 5-7. From the scatter band it can be seen that the FLAT orientations scatter lies fully within the VERTICAL orientations scatter band. For a given cyclic SIF (ΔK), this difference in scatter translates to, for the lower band, a 17% - 58% higher crack growth rate in the FLAT orientation and a 3% - 24% higher crack growth rate in the VERTICAL orientation for the upper band. Figure 5-6 shows that there is a slight "waviness" to the crack growth behaviour (compared with the FLAT orientation as seen in Figure 5-3). This behaviour may be seen in the Paris equations as well in Table 5-2. Secondly, the VERTICAL specimens started to stabilize its crack growth behaviour (lower amounts of scatter and linear crack behaviour) slightly earlier than the FLAT specimens and obtained higher cyclic SIF's (above 50 Mpa.m$^{0.5}$) before fracture occurred. A certain anomalous behaviour occurred in the VERTICAL specimens which may explain these differences and is discussed further in Chapter 6.

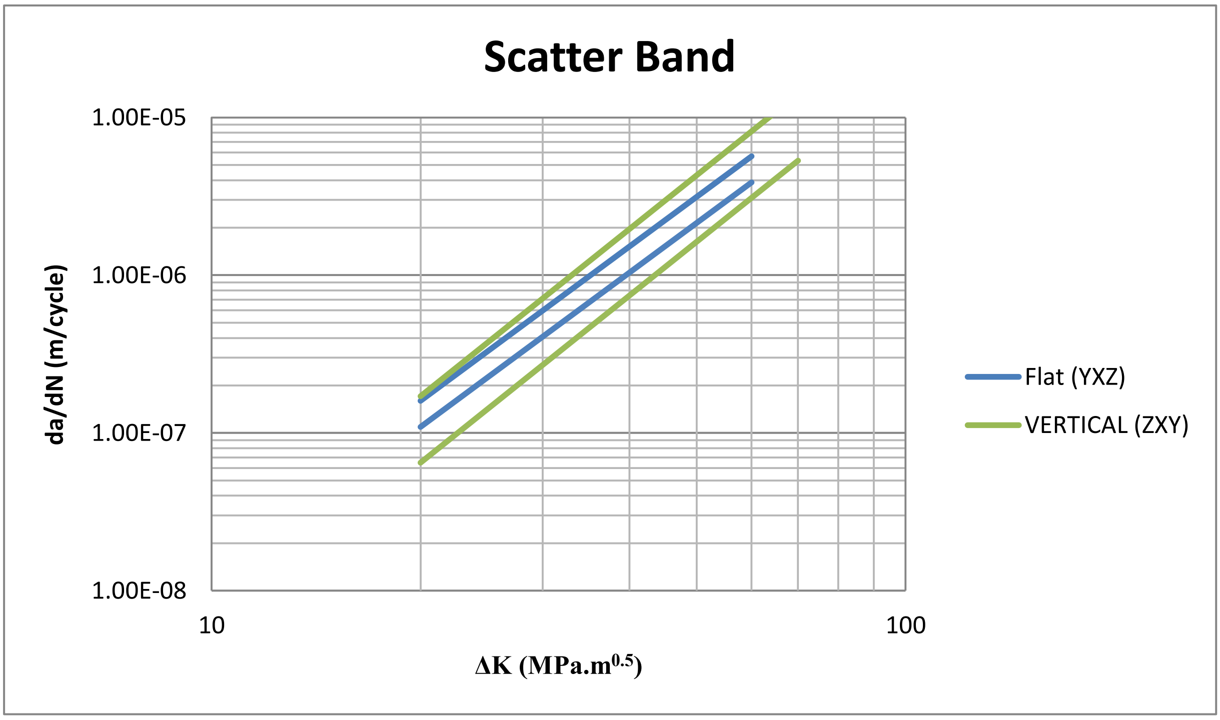

Figure 5-7: Scatter band comparison between the FLAT and VERTICAL orientations.

Table 5-2: Paris equations for specimens VERTICAL – 1, 2, 3 and 4

Test	Paris Equation
VERTICAL – 1	$\frac{da}{dN} = (5.92 \times 10^{-13})\Delta K^{3.85}$
VERTICAL – 2	$\frac{da}{dN} = (5.64 \times 10^{-12})\Delta K^{3.32}$
VERTICAL – 3	$\frac{da}{dN} = (1.09 \times 10^{-12})\Delta K^{3.82}$
VERTICAL – 4	$\frac{da}{dN} = (1.22 \times 10^{-11})\Delta K^{3.09}$
Average	$\frac{da}{dN} = (4.88 \pm 5.38) \times 10^{-12} \Delta K^{3.52 \pm 0.38}$

5.1.3 EDGE Orientation

Figure 5-8 and Figure 5-9 display the crack length versus number of cycles results for all four specimens in the EDGE (XZY) orientation. Specimen EDGE – 1 had the largest cycles to failure for this orientation and has been plotted on a separate graph (Figure 5-8). The Paris curves for this orientation are displayed in Figure 5-10.

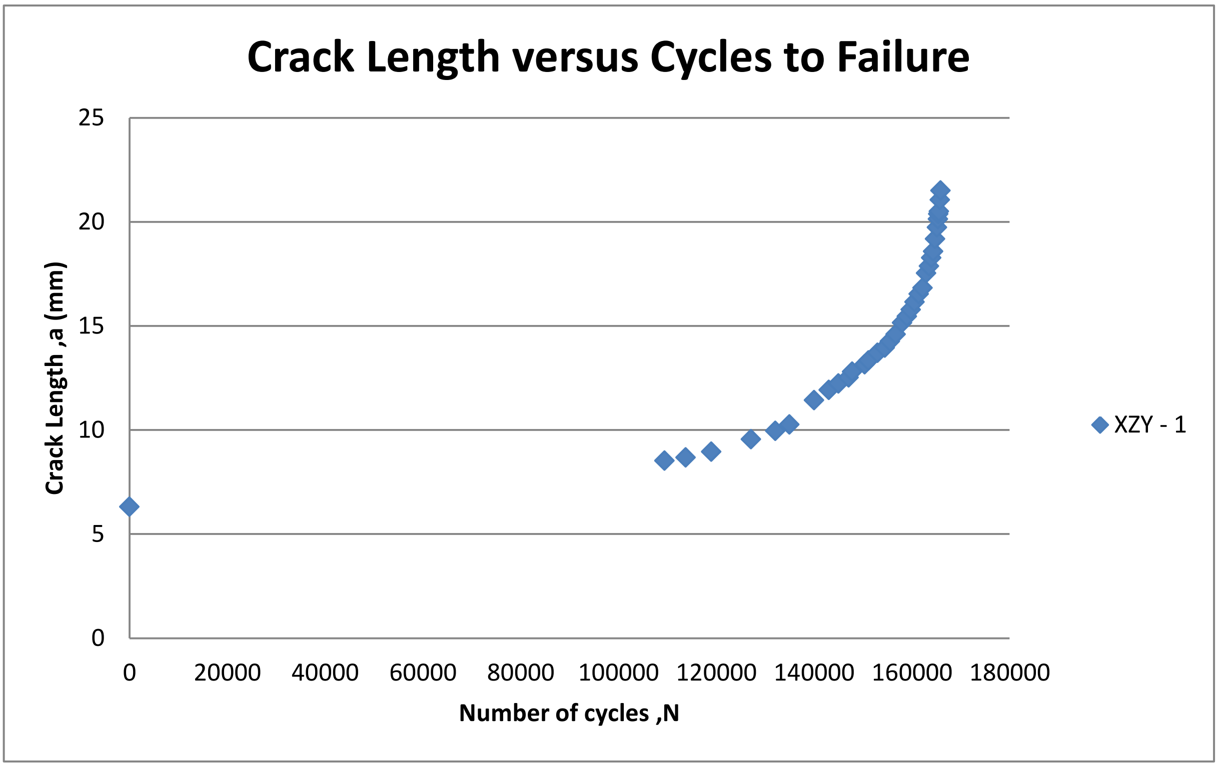

Figure 5-8: Crack length versus cycles to failure graph for specimen EDGE – 1.

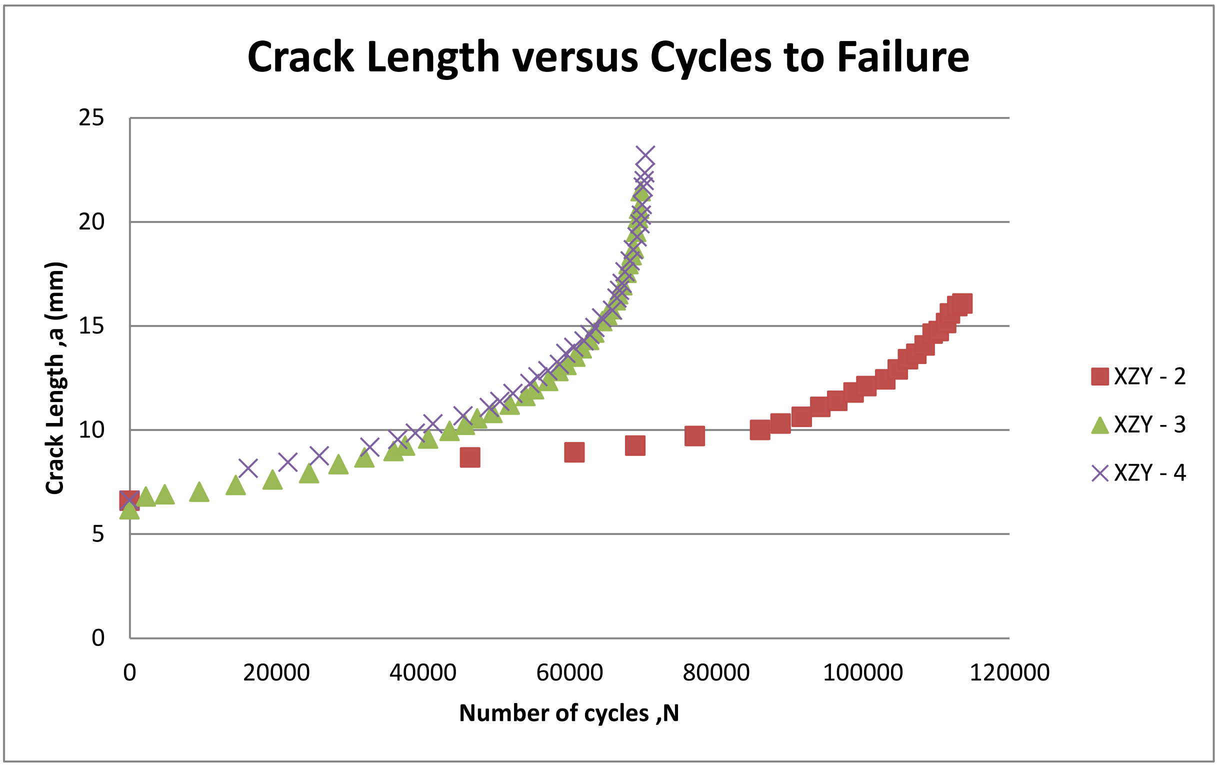

Figure 5-9: Crack length versuscycles to failure graph for specimen EDGE – 2, 3, and 4.

Specimen EDGE – 1 had the most stable crack growth behaviour (linearity) for this orientation, similar to the FLAT orientation crack growth behaviour with no anomalous behaviour observed. EDGE – 2 had the most undesirable crack growth behaviour and the test could not be conducted until failure occurred for reasons which will be explained in Chapter 6. Both EDGE – 3 and 4 did not have as stable crack growth behaviour as EDGE – 1 where EDGE – 4 had the least linear log-log behaviour of all specimens. A low load test was not conducted on the EDGE as the results from the previous orientations (FLAT – 1 and VERTICAL – 1) proved to be more time consuming than beneficial. The linear portion for the EDGE orientation was taken from a cyclic SIF of approximately 20 MPa.m$^{0.5}$ until fast fracture had occurred between 50 MPa.m$^{0.5}$ and 60 MPa.m$^{0.5}$. These observations may also be seen in Figure 5-10 and Table 5-3.

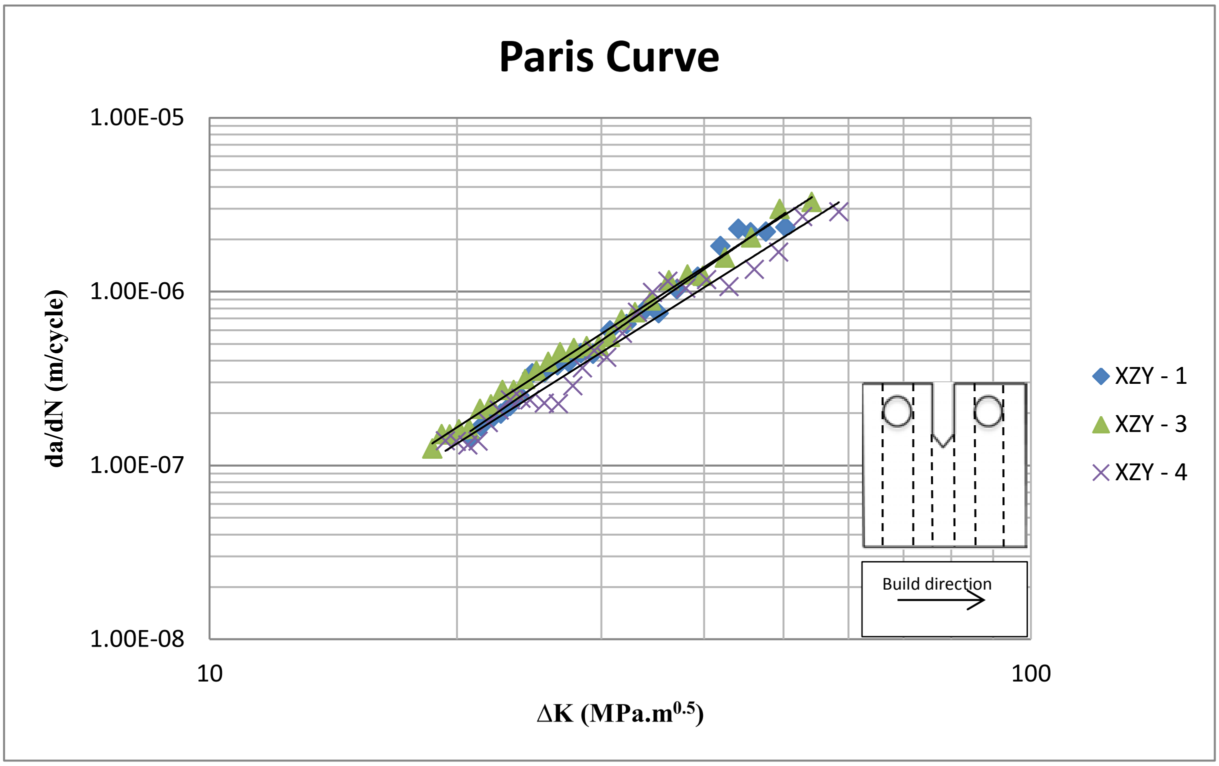

Figure 5-10: Fatigue crack growth rate (Paris regime) curve for specimens EDGE – 1, 3 and 4.

Table 5-3: Paris equations for specimens EDGE – 1, 3 and 4.

Test	Paris Equation
EDGE – 1	$\frac{da}{dN} = (7.65 \times 10^{-12})\Delta K^{3.27}$
EDGE – 2	N/A
EDGE – 3	$\frac{da}{dN} = (1.72 \times 10^{-11})\Delta K^{3.06}$
EDGE – 4	$\frac{da}{dN} = (1.76 \times 10^{-11})\Delta K^{2.98}$
Average	$\frac{da}{dN} = (14.1 \pm 5.64) \times 10^{-12}\Delta K^{3.10\pm0.15}$

Comparisons between scatter bands are made between two orientations at a time as this allows for better clarity on individual graphs. Scatter band comparisons are seen in Figure 5-11 and Figure 5-12.

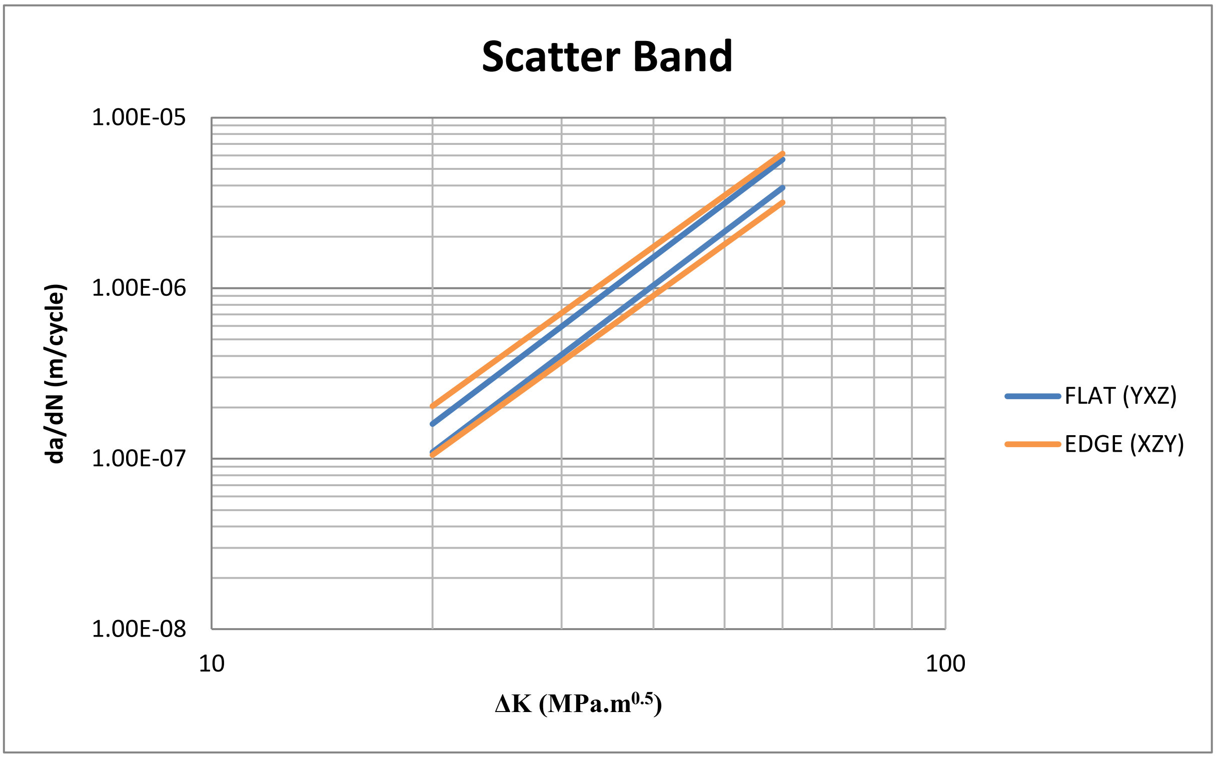

Figure 5-11: Scatter band comparison between the EDGE and FLAT orientations

It can be observed from the above figure that the EDGE orientation's scatter band contains the narrower scatter band of the FLAT orientation. The crack growth rate for a given cyclic SIF (ΔK) of the lower bands shows that the FLAT orientation has a 3% - 21% higher cyclic SIF than the EDGE orientation. It is observed that the upper band of the EDGE orientation has an 8% - 27% higher crack growth rate for a given cyclic SIF than the FLAT orientation.

When comparing the scatter bands of both the EDGE and VERTICAL orientations shown in Figure 5-12, the band width seems to be similar (similar amounts of scatter). However, due to different C and m parameters between the two orientations, the scatter bands occupy different regions of the graph. For the upper band, between a cyclic SIF between 20-40 MPa.m$^{0.5}$, the EDGE orientation has a 3% - 37% and 14% - 53% higher crack growth rate. Above 40 MPa.m$^{0.5}$, the EDGE orientation has a 6% - 13% lower crack growth rate than the VERTICAL orientation. The lower band of the EDGE orientation has a 14% - 53% higher crack growth rate than the VERTICAL orientation for a cyclic SIF ranging between 20-50 MPa.m$^{0.5}$. Above 50 MPa.m$^{0.5}$, the EDGE orientation has a 0 % - 4% lower crack growth rate than the VERTICAL orientation.

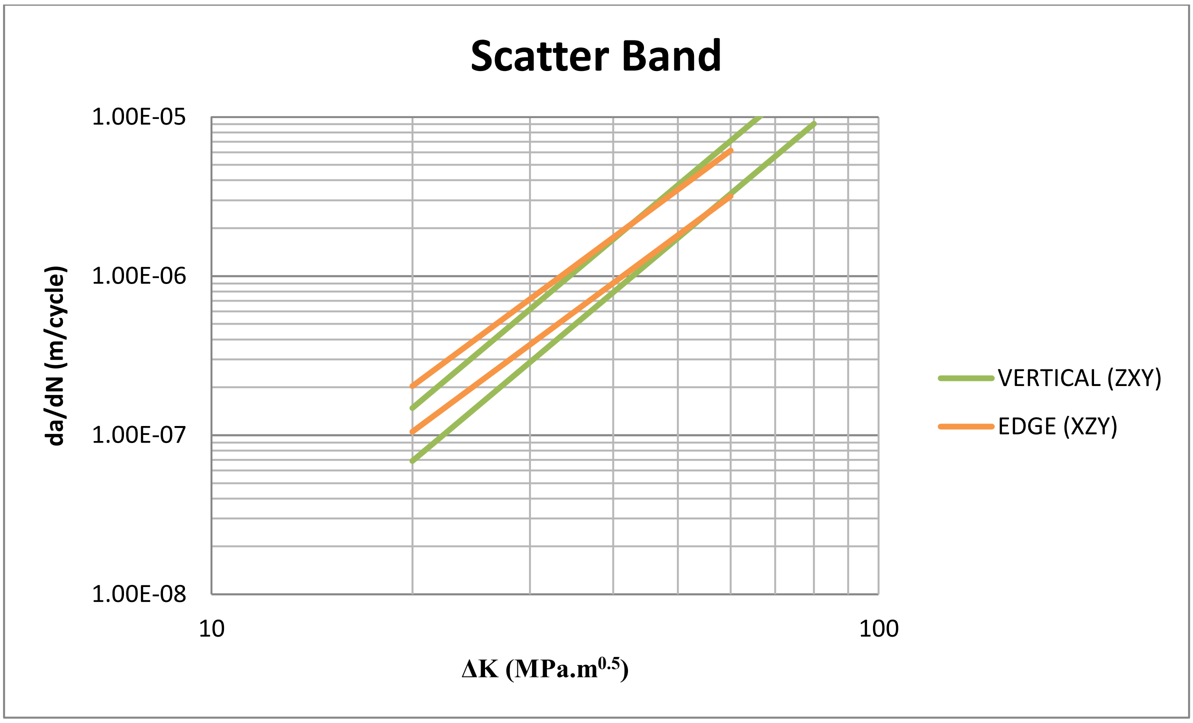

Figure 5-12: Scatter band comparison between the EDGE and VERTICAL orientations

For all of the specimens tested, ideally a 2mm precrack was aimed for. However, when conducting the tests, significant amounts of scatter and non-linearity was still present in data beyond the 2mm precrack distance when compared to the data above a cyclic SIF of approximately 18 MPa.m$^{0.5}$ and 20 MPa.m$^{0.5}$. This project only presents the results of the linear (log-log) portion of the Paris regime and considers the scatter plus non-linearity portion of the graphs as future work to be investigated.

Overall, the fatigue crack growth rate results have displayed that the FLAT (YXZ) orientation has the least amount of scatter when compared to that of the VERTICAL (ZXY) and EDGE (XZY) orientations. The FLAT orientation also has the greatest repeatability in results. Despite the difference in scatter and fast fracture values, each orientation displays acceptable results and occupies similar regions on the da/dN versus ΔK graphs. Comparing the medians of the scatter bands for all three orientations, seen in Figure 5-13, highlights the similarities and displays slight differences in each orientation. The greatest difference that is observed from these fatigue crack growth rate results is the scatter between each orientation. However, there are greater differences with respect to the orientations that have been observed during testing. These differences have been referred to as anomalies within this chapter and are discussed in detail in Chapter 6.

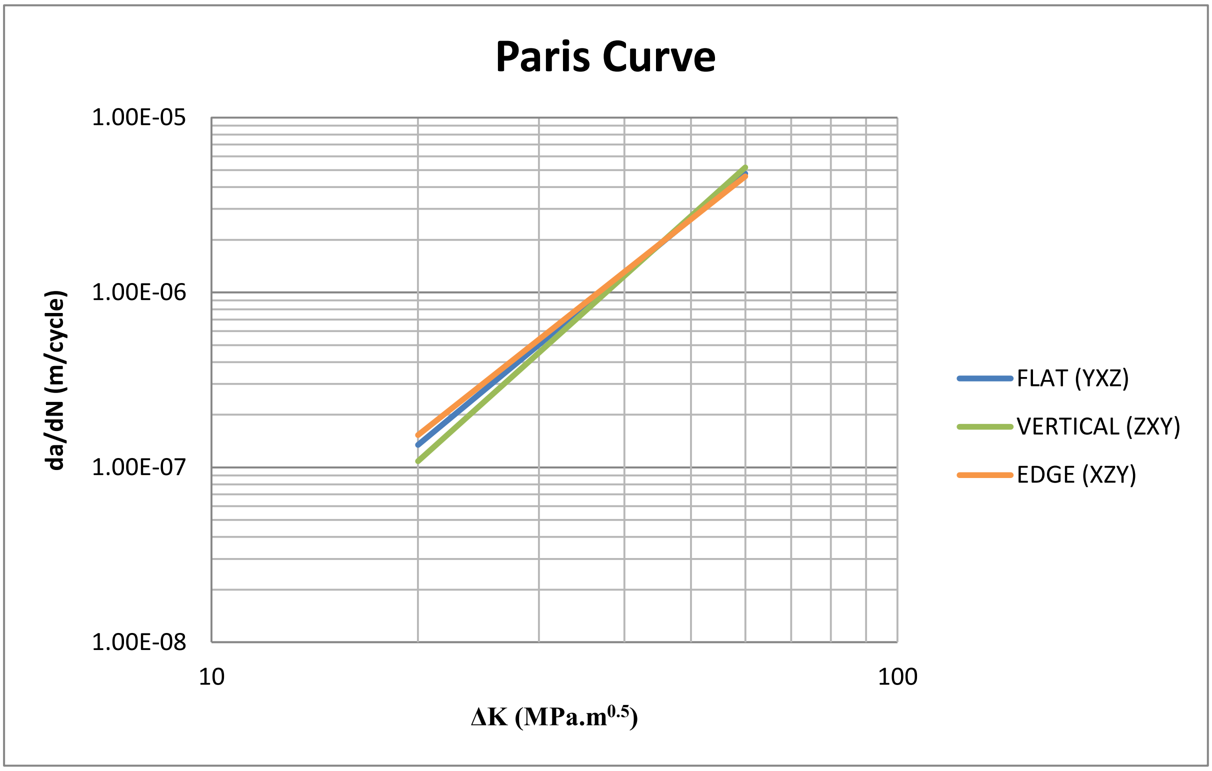

Figure 5-13: Paris curve of the average Paris equations of each orientation.

Error Analysis

The uncertainty in results mainly stems from the load cell and loop tuning that is used for testing purposes. Other sources of error which have been identified, largely has a negligible effect on the results and are all listed below:

- **Load Cell:** The load cell has a ± 0.5% error of the reading of the load cell capacity. The load cell capacity is a 50kN load cell which means there is a ± 0.25kN error on both fatigue crack growth rate and fracture toughness testing.

- **Loop Tuning:** This involved the PID tuning specific to the fatigue crack growth rate testing only. The error was kept below 1% on individual tests.

- **ESH Universal Machine:** In order for the fatigue motion to occur, pistons are driven through a distance. Although there are errors on the position of the pistons, all testing was conducted under load control, and thus any positional errors of the pistons will be taken as negligible.

- **Travelling Microscope:** The microscope has a precision of 0.025mm while an error on the readings is not known. However, a travelling microscope typically has an error of 0.005mm which translates to a 0.006 MPa.$m^{0.5}$ error for a measured crack length. This error will be regarded as negligible.

- **Vernier Calliper:** The Vernier calliper had a 0.02mm error on the reading. It was used to measure the W, a_n, and B of all specimens. This translates to 0.01, 0.02 and 0.05 MPa.$m^{0.5}$ respectively. These values will be regarded in fracture toughness error calculations only.

Where applicable, these errors will be used in the relevant calculations and displayed error margins such as in Table 5-4.

Table 5-4: The fatigue crack growth rate results

Specimen	Initial ΔK at notch (MPa.m$^{0.5}$)	"Precrack" ΔK (MPa.m$^{0.5}$)	ΔP (kN)	Error Margin (kN)	Actual R-ratio range
FLAT – 1	6.5	22.21	1.8	± 0.27	0.27
FLAT – 2	12.3	20.55	3.375	± 0.29	0.02 – 0.2
FLAT – 3	13.4	22.11	3.6	± 0.29	0.03 – 0.19
FLAT – 4	14	20.74	3.825	± 0.29	0.03 – 0.18
VERTICAL – 1	6.6	17.03	1.8	± 0.27	0.27
VERTICAL – 2	12.4	18.1	3.375	± 0.29	0.02 – 0.2
VERTICAL – 3	13.2	17.55	3.6	± 0.29	0.03 – 0.19
VERTICAL – 4	14.2	20.76	3.825	± 0.29	0.03 – 0.18
EDGE – 1	12	20.08	3.15	± 0.29	0.02 – 0.2
EDGE – 2	-	-	-	-	-
EDGE – 3	13.6	18.16	3.6	± 0.29	0.03 – 0.19
EDGE – 4	14.5	18.82	3.825	± 0.29	0.03 – 0.18

5.1.4 Density

The density results are shown below in Table 5-5.

Table 5-5: Density test results

Specimen	Average Mass in air (g)	Average Mass in Water (g)	Density (%)	Average
FLAT – 1	18.86	14.82	99.69	99.66 ± 0.02
FLAT – 2	18.70	14.69	99.64	
FLAT – 3	17.41	13.69	99.62	
FLAT – 4	17.72	13.93	99.65	
VERTICAL – 1	17.93	14.08	99.46	99.66 ± 0.11
VERTICAL – 2	17.98	14.14	99.73	
VERTICAL – 3	17.04	13.41	99.77	
VERTICAL – 4	17.02	13.39	99.66	
EDGE – 1	18.62	14.62	99.51	99.40 ± 0.51
EDGE – 2	19.46	15.23	98.53	
EDGE – 3	19.08	14.99	99.78	
EDGE – 4	19.44	15.27	99.78	

Each orientation had similar densities, however, specimen EDGE – 2 had the lowest densities and will be discussed further in Chapter 6.

Slight variations in densities from specimen to specimen have been observed, with a one having a significant difference in density namely specimen EDGE-2. The small variations in the density reading may be contributed to experimental error. Some examples of where the errors may originate from include:

- Various amounts of surface pores per a specimen (air bubble adhesion)
- A small area of the specimen was polished i.e. surface roughness (air bubble adhesion)
- Amount and location of porosities within specimens may differ from specimen to specimen
- Mishandling of specimens causing scratches and dents
- User error

5.2 Fracture Toughness Testing

The fracture toughness tests were conducted on a total of nine specimens (three per orientation), which are completely separate from the fatigue crack growth rate specimens.

5.2.1 FLAT, VERTICAL and EDGE Orientation

For clarification, one figure and one force versus displacement graph per specimen orientation is given below. All fracture toughness results are listed in Table 5-6. All remaining fracture surface figures and force vs. displacement graphs may be found in the relevant appendix.

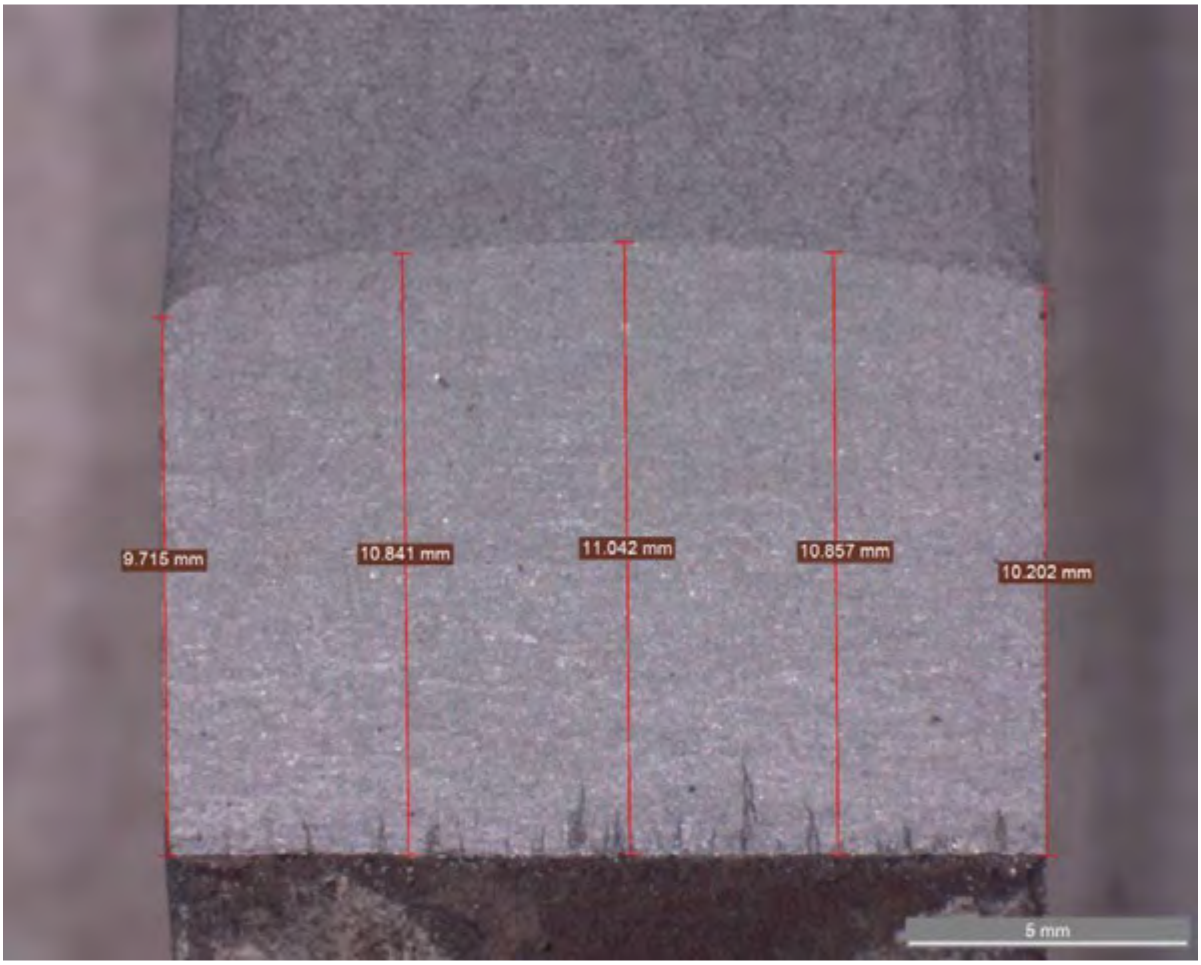

Figure 5-14: Crack length measurement of fracture surface of specimen FLAT – 2.

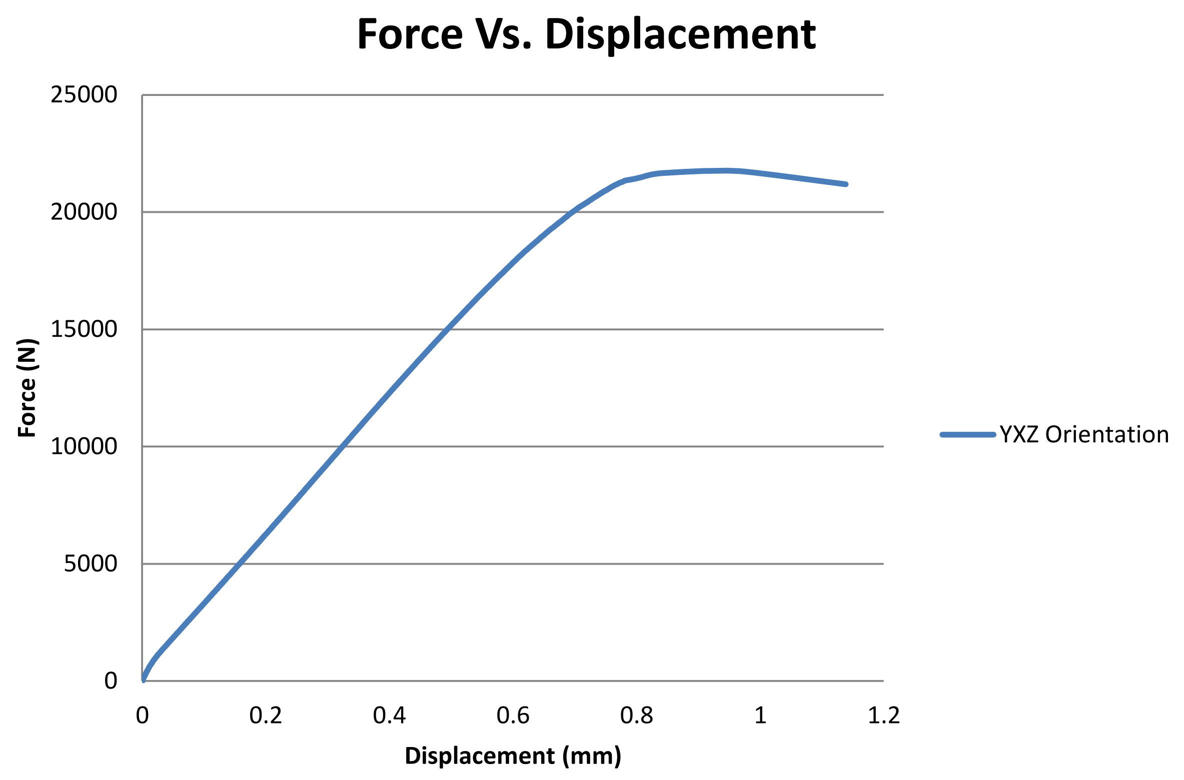

Figure 5-15: Graph of force vs. displacement for specimen FLAT – 2.

Figure 5-16: Crack length measurement of fracture surface of specimen VERTICAL – 3.

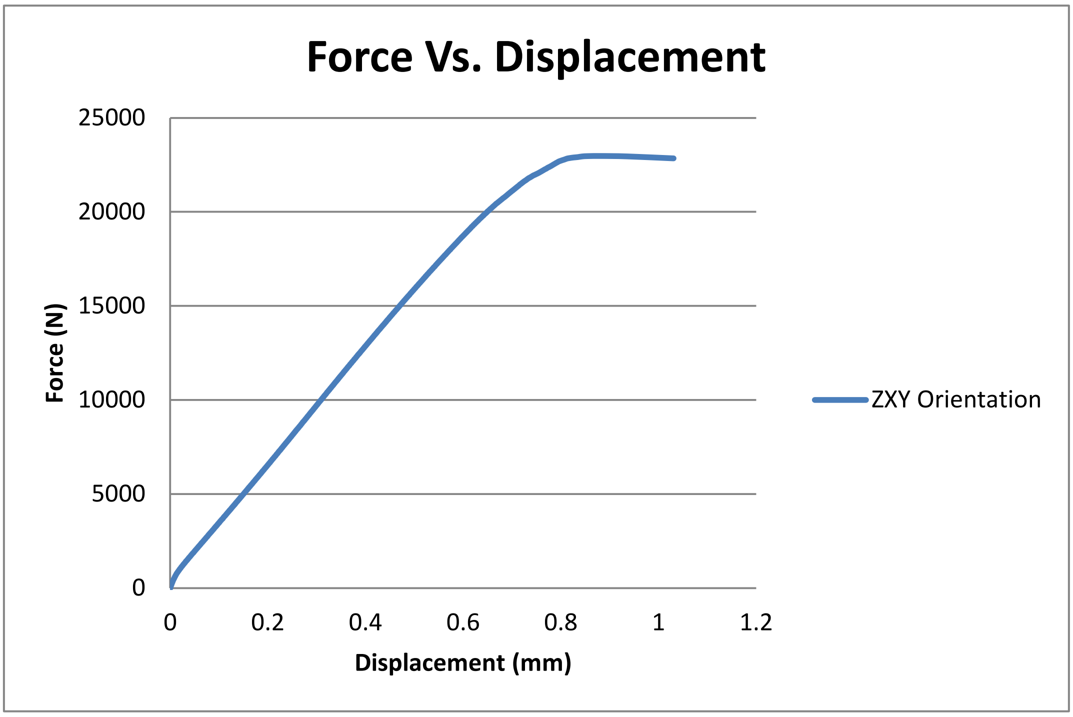

Figure 5-17: Graph of force vs. displacement for specimen VERTICAL – 3.

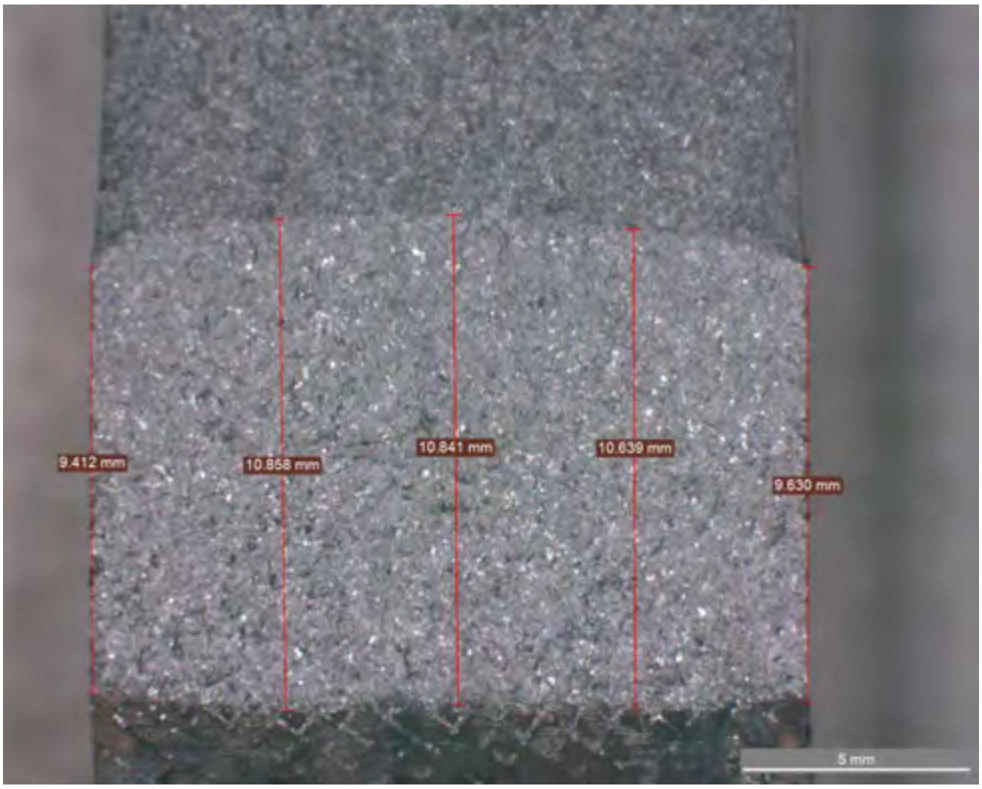

Figure 5-18: Crack length measurement of fracture surface of specimen EDGE – 3.

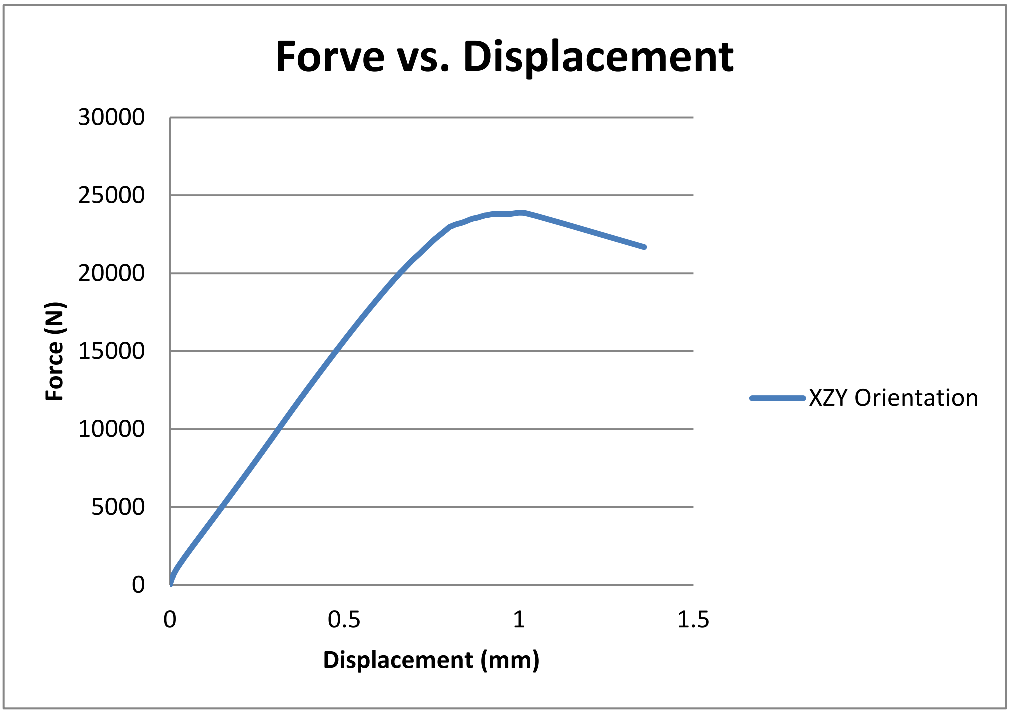

Figure 5-19: Graph of force vs. displacement for specimen EDGE – 3.

Table 5-6: Fracture toughness testing results

Specimen	Cycles to precrack (rounded off)	P_{max} (N)	P_Q (N)	P_{max}/ P_Q	Average Crack length (mm)	K_{max} at precrack (MPa.m$^{0.5}$)	**K_Q (MPa.m$^{0.5}$)
FLAT – 1	57000	21684	20078	1.08	17.29	37.26	75.63
FLAT – 2	56200	21756	20128	1.08	17.13	36.66	74.36
***FLAT – 3**	59600	23602	21830	1.08	17.82	39.71	74.82
VERTICAL – 1	53400	25218	22870	1.10	16.21	33.70	76.07
VERTICAL – 2	55900	21687	20602	1.05	17.18	37.18	75.36
VERTICAL – 3	57200	22973	20935	1.09	17.15	37.06	75.54
EDGE – 1	52700	24357	22150	1.09	16.46	34.81	78.45
EDGE – 2	58900	22041	20707	1.06	17.42	38.49	80.53
EDGE – 3	54500	23834	21615	1.10	16.91	36.53	79.74

* Invalid according to E399 section 8.2.3

**The error margin calculated on all fracture toughness values equate to 0.44 MPa.m$^{0.5}$.

The fracture toughness results of the SLM Ti-6Al-4V display acceptable results and behaviour. Each orientation display similar results to each other while the EDGE orientation repeatedly remains approximately 6% higher in fracture toughness. The fracture surface of the EDGE orientation is largely different to that of the FLAT and VERTICAL specimens, shown in Figure 5-20. This difference may be attributed to the specimen orientation, but is not understood fully at the moment and warrants further investigation at higher magnifications (which was not within the scope of the project).

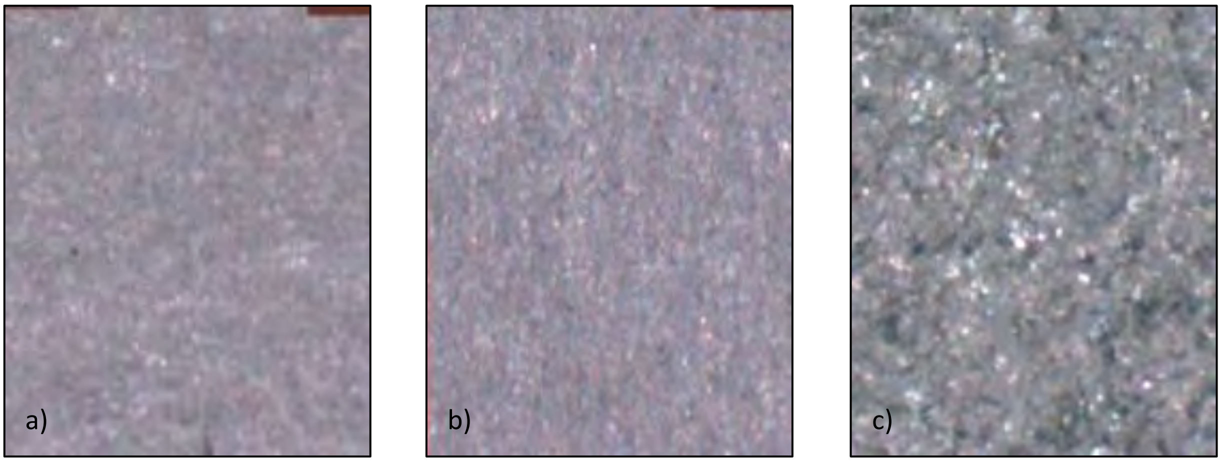

Figure 5-20: Portions of fracture surfaces of a) FLAT, b) VERTICAL and c) EDGE specimens.

5.3 Microstructure

The Microstructure obtained from the SLM Ti-6Al-4V specimens was from both the as-built and heat treated condition. The as-built microstructure contains very fine, acicular martensitic structure (α' needles) due to the high temperatures and rapid cooling, characterised by the process. This fine microstructure causes the SLM material to have a high strength but with low ductility. The signature SLM columnar grains, seen in Figure 5-21, are apparent when observing the specimen's build direction. A top view of the specimen reveals that the fine acicular martensitic structure is contained within equiaxed grains, displayed in Figure 5-22.

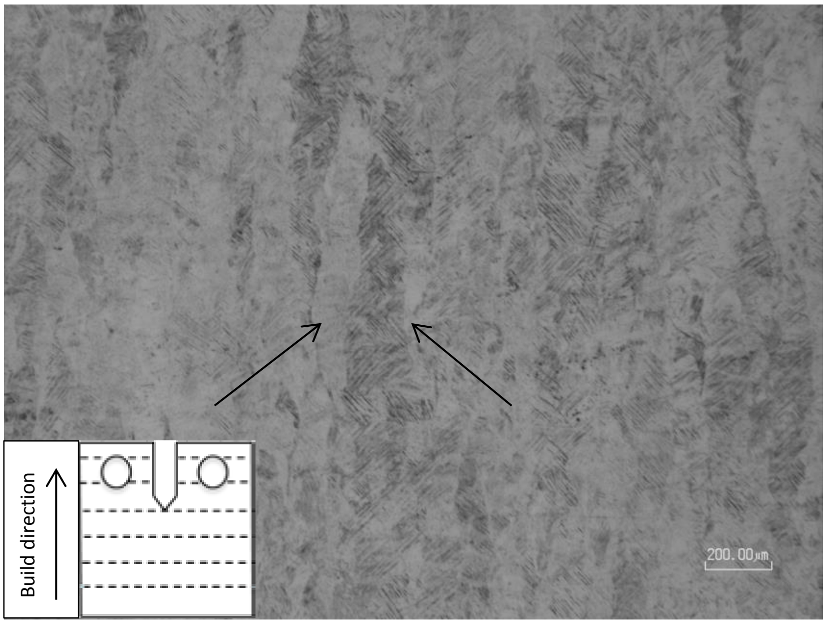

Figure 5-21: Columnar grains of SLM Ti-6Al-4V (identified by black arrows)

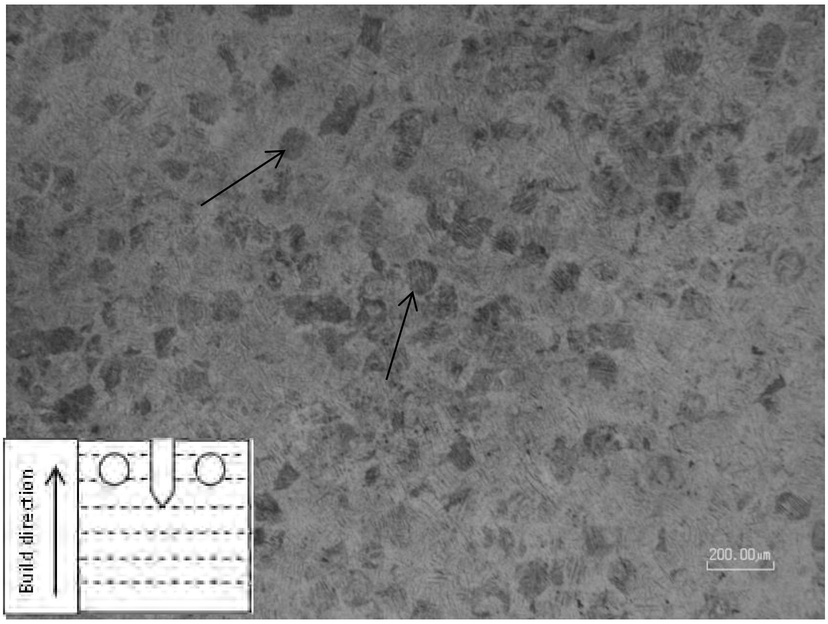

Figure 5-22: fine acicular martensitic structure is contained within equiaxed grains of SLM Ti-6Al-4V (identified by black arrows)

After the duplex anneal heat treatment, microstructural analysis shows that the microstructure of the specimens has changed when compared to the as-built microstructure. It has also been observed that the columnar grains are not as apparent after the duplex anneal heat treatment as it was before the heat treatment. Figure 5-23 and Figure 5-24 displays the microstructure at two different magnifications after the duplex anneal heat treatment has taken place which has a basket-weave like structure and consists of primary α with lamellar α and β regions.

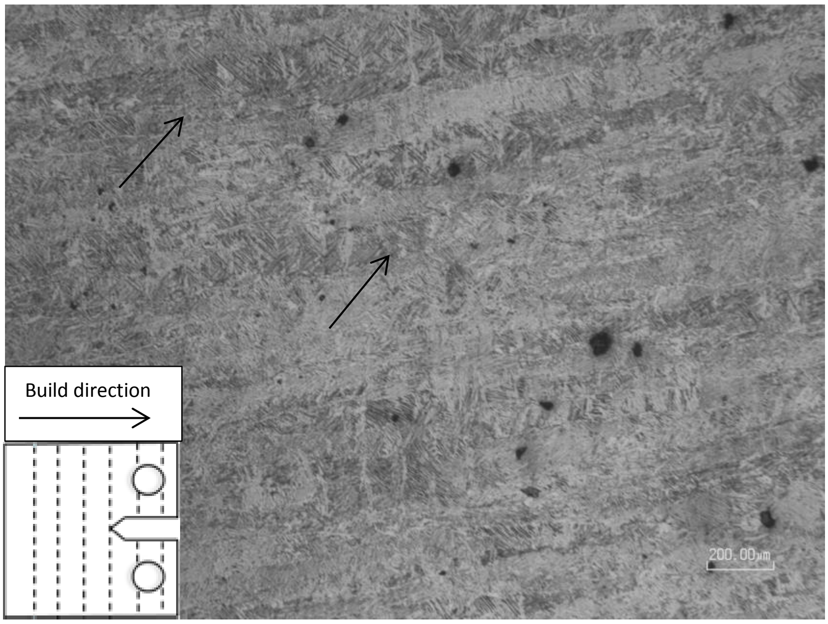

Figure 5-23: Microstructure after duplex anneal heat treatment (black arrows indicate visible columnar grains)

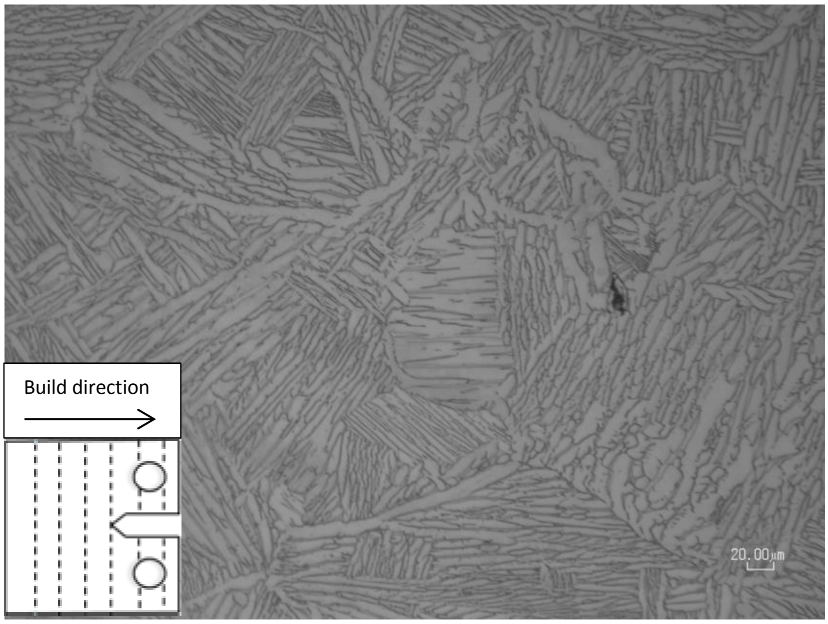

Figure 5-24: Lamellar like microstructure after duplex anneal heat treatment

This drastic change in microstructure, as compared to the as-built microstructure, indicates that a large amount of residual stress has been relieved. The strength of the heat treated material would have decreased but with an increase in ductility. The lamellar-like microstructure causes a fatigue crack to produce a torturous path, as the crack propagates, which makes crack propagation more difficult [85]. Furthermore, during fracture, the crack path is deviated which leads to an increased fracture toughness [60].

5.4 Summary

This chapter presented the fatigue crack growth rate results of SLM Ti-6Al-4V with respect to three build orientations. The fatigue crack growth rate results indicated acceptable results through all of the orientations while the largest difference found between these orientations is the amount of scatter produced. It is evident though from the raw data, that linearity (log-log) in the FLAT specimens only occurs from approximately 20 MPa.m$^{0.5}$ onwards until fast fracture occurs below 50 MPa.m$^{0.5}$. These linearity traits are also found in the VERTICAL and EDGE orientations where stability in crack growth behaviour occurs at approximately 18 MPa.m$^{0.5}$ and fast fracture occurs above 50 Mpa.m$^{0.5}$. It is therefore important to note that the Paris equations obtained in this research project is for SIF's above 18 MPa.m$^{0.5}$. Furthermore, certain anomalous behaviour which presented itself in the VERTICAL and EDGE orientations has been mentioned and will be discussed in Chapter 6. It was found that the fracture toughness of the material showed no significant difference between orientations while it was observed that the EDGE specimens displayed a different fracture surface than that displayed on the FLAT and VERTICAL fracture surfaces. The density of the material for all three orientations was typically above 99.5% of the full density. Microstructural changes were observed between the as-built microstructure and the duplex anneal heat treated microstructure. The following chapter attempts to discuss these results, in detail, in order to increase the understanding of the research on this material.

Chapter 6 – Discussion

Section 2.5 introduced the concept of assessing an engineering system on its “fitness for purpose” by using methods provided by fracture mechanics. It is through the experimental approach presented in Chapter 4 and the understanding of the results presented in Chapter 5, that the “fitness for purpose” of an engineering system may be assessed. There still exists a need for an understanding of the fatigue crack growth rates with respect to build orientation, where in literature, these differences are noticed and possible theories as to why there are these differences is given, but not yet fully understood from research. Furthermore, no significant amount of work has been published on the fracture toughness of SLM Ti-6Al-4V and whether or not the same build orientation effects noticed in the fatigue crack growth rate regime is apparent in fracture toughness testing. This thesis endeavours to contribute to the understanding of these differences, to at least rule out, or add in, possible theories as to why there is a noticeable build orientation effect on crack growth behaviour. This chapter discusses the observed results of all experimental studies and attempts to interpret the findings for the crack growth rate and fracture toughness testing with respect to build orientation.

6.1 Fatigue Crack Growth Rate Behaviour

The investigation of SLM produced parts is a complex process as there are a large number of parameters which may influence the performance of the SLM product. These parameters do not only include the laser scanning parameters i.e. laser power, laser spot diameter, laser scan speed or strategy, but also the materials properties such as viscosity, thermal conductivity, surface tension, melting temperature, particle shape, particle size, composition etc.. Furthermore, a combination of the material and processing parameters such as the absorptive/reflective properties, environmental conditions, bed temperature, material distribution, molten pool size and post processing procedures all play a large role in the performance of the SLM products. Within this MSc project, all specimen orientations have been manufactured by the same 3D printer and received the same post processing procedures i.e. the same scanning parameters and have undergone nominally the same heat treatment (duplex anneal). Thus the main differences between each orientation is the grain orientation, crack growth direction with respect to grain orientation (as well as build orientation), specimen build height and, as mentioned by Mercelis et al [61], the effect of residual stress on build height.

The observed results have demonstrated that the fatigue crack growth rate behaviour has noticeable differences in its scatter with respect to build orientation. Differences in crack growth behaviour (scatter) with respect to build orientation have been mentioned by Edwards and Ramulu [7] and is also noticed in the works of Leuder's et al [5]. Edwards and Ramulu [7] suggest that these orientations effects (scatter) may stem from porosity, microstructure and residual stress.

Porosities is an inevitable part of the SLM process as there is no mechanical pressure during the process, as well as, gas bubbles being entrapped during solidification [86]. Other factors such as Laser power, scan speed, scan strategy, energy density, unfused powder, material properties etc. all have a significant role in the formation of porosity [7], [87]. Generally, the mechanical properties of a material, such as fatigue strength, is hampered by the presence of porosities as they act as stress raisers and crack initiation sites [7], [88] . However, porosities do not have a significant impact on the monotonic tensile properties [5], [88]. It is advantageous to improve the ductility of the part (via heat treatments) in order to reduce the sensitivity of crack initiation at porosity sites [7].

It is shown within this project and some works within literature that the as-built martensitic microstructure transforms into a different structure, depending on the heat treatment. In both this project and the work of Leuder's et al [5], lamellar like microstructures were obtained, but of different sizes (due to differences in heat treatments). This not only shows a decrease in the residual stress, but also decreases the tensile strength and increases the ductility of the material. Thus decreasing the sensitivity for crack initiation compared to crack initiation in the as-built condition. Due to the inherent formation of columnar grains from the SLM process, there is a difference in mechanical performance depending on the loading alignment with the columnar grain [7]. This anisotropic behaviour showed that when specimens are loaded to align with the columnar grains, rather than loaded transversely to the columnar grain, the fatigue limit is reduced as well as the differences in tensile properties [7]. This may be due to preferentially orientated slip planes which are parallel to the columnar grains [7]. In the works of Leuder's et al [5], it is not mentioned, but it is clearly seen that there is a difference in fatigue crack growth rate behaviour (scatter) with respect to build orientation, shown in Figure 3-2 and Figure 3-3. The orientation with the greater amount of scatter is the one where the crack is grown parallel to the columnar grains. It should be noted that for the HIPed condition specimens, the orientation with the crack grown parallel to the columnar grains still had larger scatter in the crack growth behaviour than the other orientation. Suggesting that microstructure may have a larger effect than porosity on orientation effects. As mentioned before, for the work conducted within this MSc project, the fatigue crack growth rate behaviour has noticeable differences in its scatter with respect to build orientation. However, the differences between the orientations are not only restricted to the scatter present in the Paris curves but is also present on the physical specimen.

One of the differences is seen when comparing the surface crack profiles of each orientation to each other, as shown in Figure 6-1. The crack paths from the FLAT and VERTICAL specimen tend to have more deviations in its crack path, pointed out in Figure 6-1 a) and b), compared to that of the EGDE specimen. It is also evident that the VERTICAL specimen has a “wave-like” crack path, circled in Figure 6-1 b), which is not as apparent in the other orientations. Additional research is required to fully explain why the crack profiles differ from each other, but it could be associated with the type of microstructure combined with the relationship between the fatigue crack and columnar grains. It may be because of the microstructure alignment with the fatigue cracks that the amount of scatter in the different orientations differs.

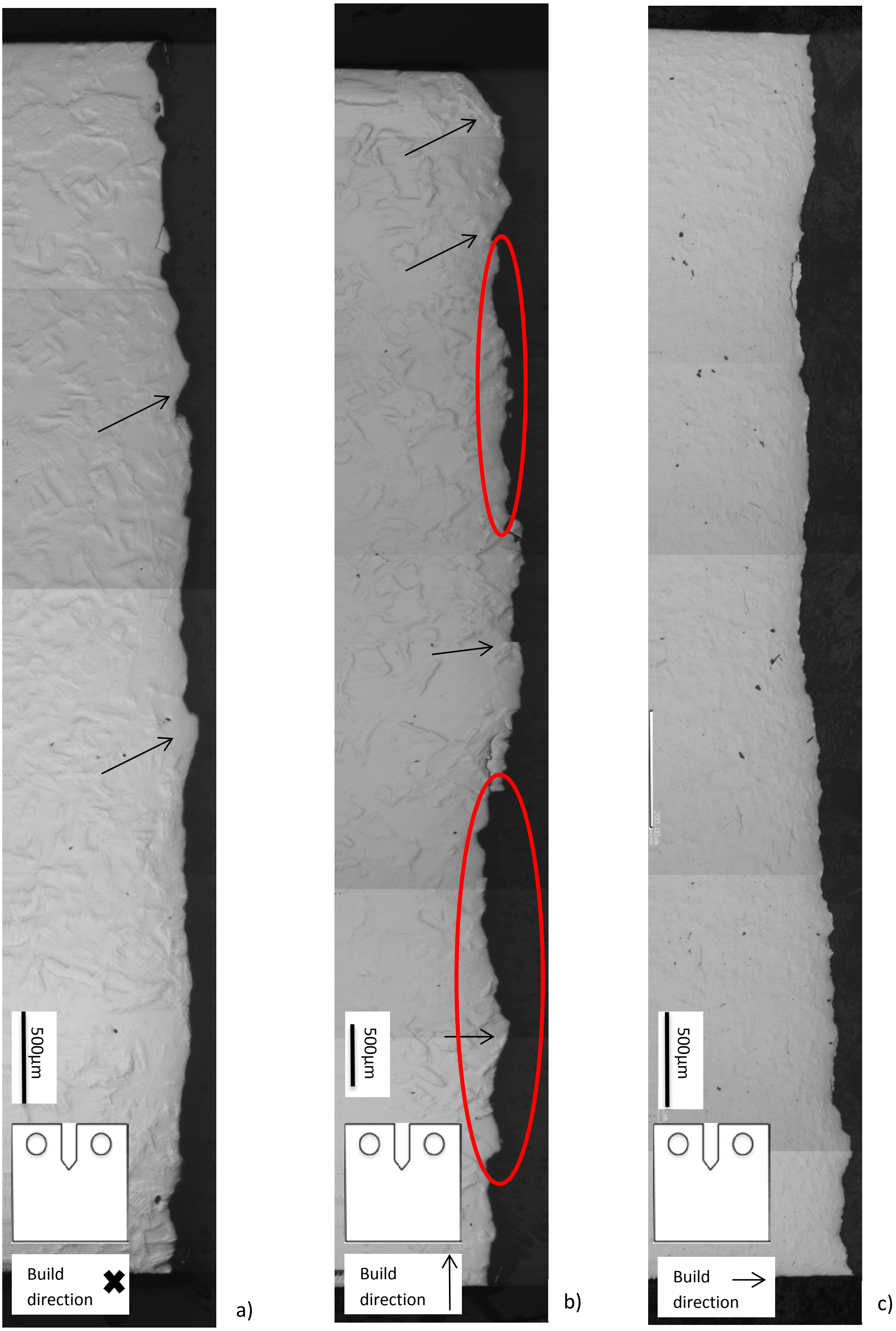

Figure 6-1: Surface crack profiles of a) FLAT b) VERTICAL and c) EDGE specimens.

The majority of the work in literature, if not all, on SLM manufacturing, mention residual stress and the need for it to be reduced. The works have shown that large residual stresses are present in the material in which stress level measurements vary due to manufacturing parameters, specimen orientation, point of residual stress measurement as well as vary through the thickness of the material [1], [5], [7], [89]. Below is a table illustrating some of the works conducted on residual stress on SLM Ti-6Al-4V.

Table 6-1: Residual stress measurement of SLM Ti-6Al-4V

	Knowles [1]	**Vranken et al** [89]	**Leuders et al [5]**	**Edwards et al [7]**
Maximum Measured Stress	≈1200 MPa	≈1000 MPa	≈775 MPa	≈550 MPa
Measurement type	Drill method	Contour method	Drill method	Drill method
Maximum Stress after heat treatment	(four heat treatments) 1. ≈ 236 MPa 2. ≈ 60 MPa 3. ≈ 82 MPa 4. ≈ 93 MPa	≈350 MPa	≈10 MPa	–

Leuders et al [5] shows in his work that porosities, microstructure and residual stress affect the fatigue limit and fatigue crack growth behaviour as the onset of crack initiation occurs earlier than in material which has lower porosities and lower residual stresses. This can be seen in Figure 3-2, Figure 3-3 and Table 3-2. Due to the varying residual stress through the thickness of a material, which can be greater than 1 GPa [89], the crack front becomes distorted as shown in Figure 6-2 [89]. This shows that under tensile fatigue conditions, part of the material will be at stress large enough for crack propagation while the mid-section of the material will be experiencing lower crack propagating stresses [89].

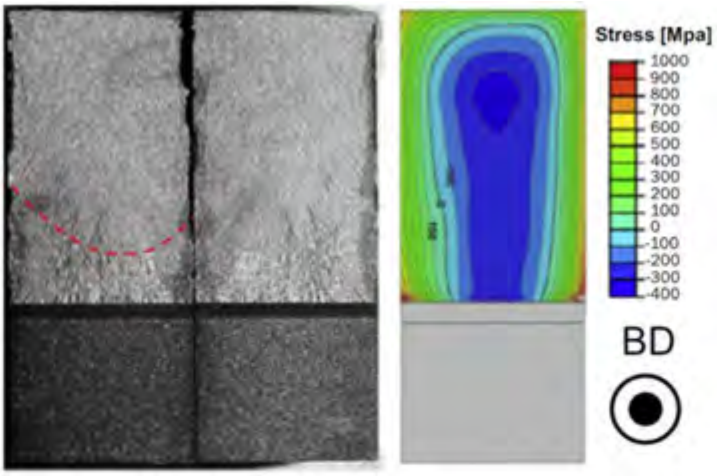

Figure 6-2: Crack front profile and stress field of fracture surface [89].

Not only does the residual stress cause the early onset of crack formation and distortion of crack front profile (figure above), but may also cause certain forms of permanent damage in the material, such as microcracking. Due to the high fabrication temperatures and rapid cooling which leads to large residual stresses, thermal-induced cracking may occur within the material as shown in Figure 6-3 and Figure 6-4 [87], [90]. Figure 6-3 also illustrates what is known as a ball formation. This happens when high laser scan speeds are used and applies more shear stress to the now liquid material which generates larger surface tensions inside the melt pool, leading to the ball formation [87]. This contributes to porosities, which act as stress raisers and in turn may lead to microcracking.

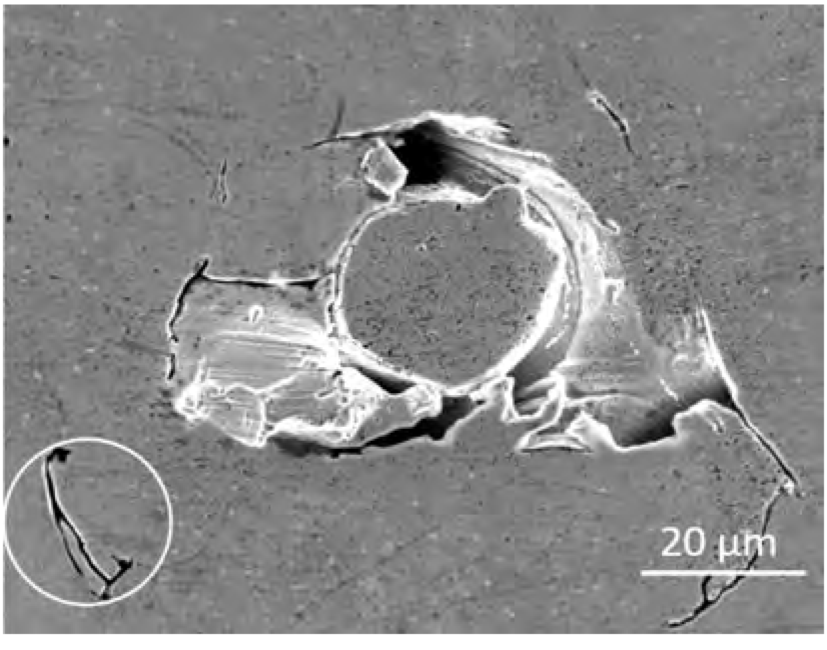

Figure 6-3: Thermal-induced cracking and balling phenomenon in SLM 17-4PH Stainless Steel [87]

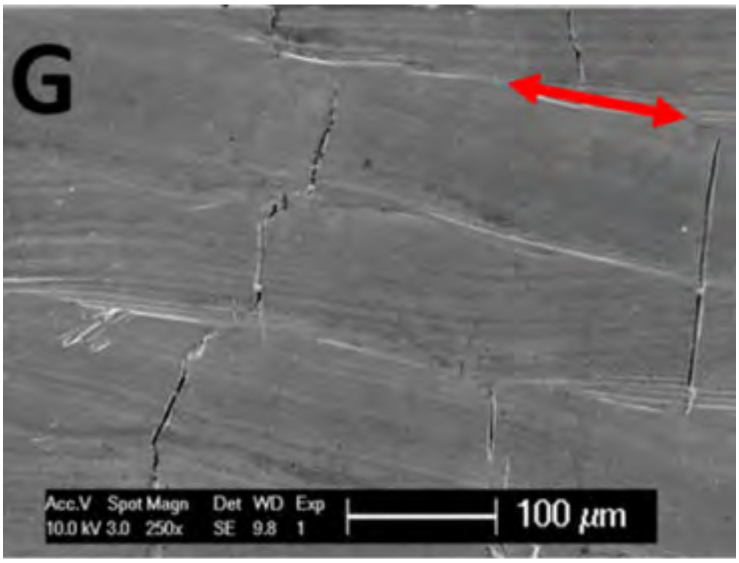

Figure 6-4: Microcracking in SLM Hastelloy C-276 [90]

Furthermore, there are certain defects that are encountered during welding with titanium alloys, which include: solidification segregation, solidification cracking, contamination cracking and ductility dip cracking [8].Although this project is concerned with SLM and not welding, due to the high temperatures and rapid cooling in both welding and SLM, the welding defects mentioned may possibly occur during the SLM manufacturing process.

One of the anomalies observed during the fatigue crack growth testing is assumed to be caused by the effects of residual stress. When under the effect of residual stress, the stresses in the EDGE orientated specimens act in a manner which would favour crack growth. After stress relieving (duplex anneal) is complete, and once the fatigue crack growth rate testing has begun, crack initiation occurs almost immediately. Within approximately 50 cycles, compared to several thousand cycles for the other orientations, a crack had initiated and opened up to approximately 0.2mm. Thereafter the fatigue crack had propagated as per normal. Suggesting that even after stress relieving, there is a significant amount of sensitivity or weakness in the notch area of the EDGE orientated specimens (if residual stress is the cause of this effect).

It is not clear to what extent porosities, microstructure and residual stress cause the orientation effects (scatter) noticed within this work, as well as in the works of Edwards and Ramulu [7], and Leuders et al [5]. It may be that a combination of these parameters causes orientation effects. Although these three points have been elaborated on, factors such as manufacturing parameters may also have a significant effect on orientation effects, which will be highlighted on later in this chapter (Chapter 6).

6.1.1 Microcracking

The main anomaly which occurred only in the VERTICAL and EDGE orientations was that of microcracks which had formed ahead of the main fatigue crack tip. These microcracks were observed to occur along the length of the crack path and intensify as the fatigue crack got larger. Figure 6-5, Figure 6-6 and Figure 6-7 depict a fatigue crack with an abundance of microcracks around the crack of specimen VERTICAL – 1. The microcracking started at approximately 6mm measured from the notch, and as the microcracks formed, it was seen to appear as far as and further than 1mm away from the main crack tip. The stress field at the crack tip was briefly examined using Eqn 2.7 to calculate the stress at various points around the crack tip. Figure 6-8 depicts this process. For simplicity, the calculation uses a measurement of 6 mm away from the notch (where microcracking was first noticed), which corresponds to a cyclic SIF of 30MPa.m$^{0.5}$, as the point of interest. At this point of interest, a radius of 1 mm, measured from the crack tip, is used to calculate the stresses within this specific stress field which caused microcracks to “initiate” and propagate. Figure 6-9 depicts the results of the crack tip stress field analysis.

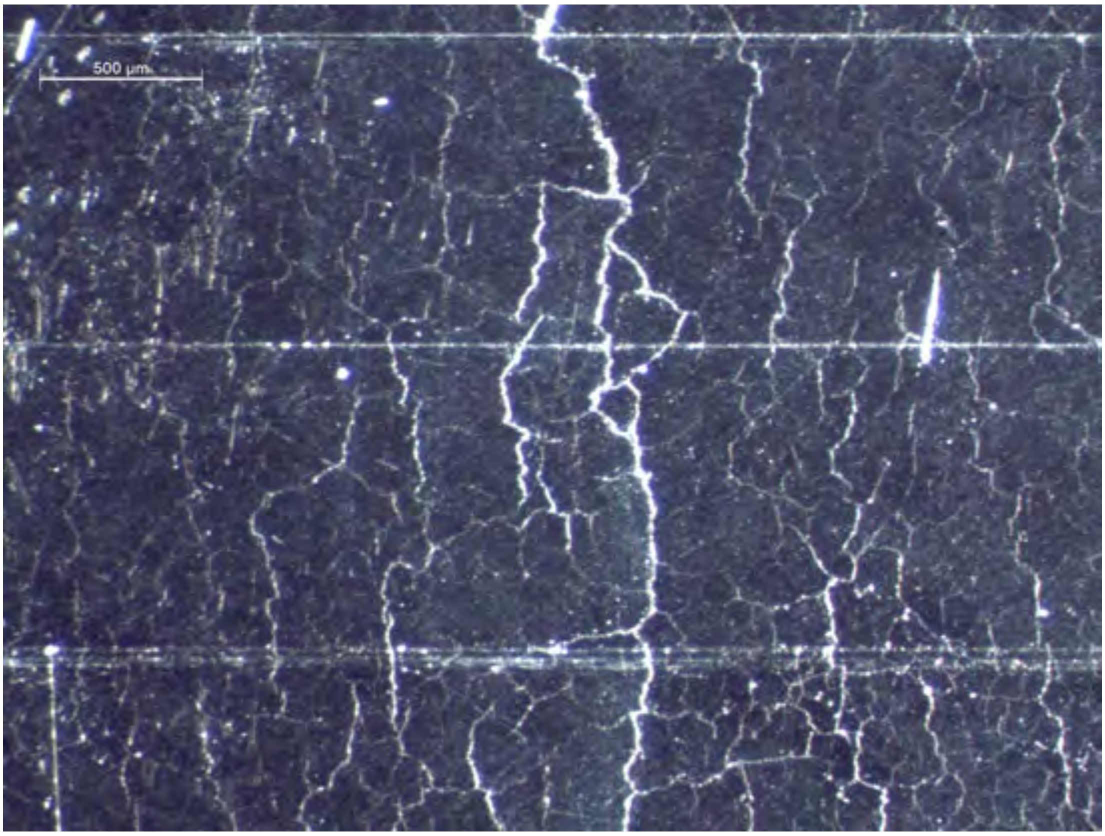

Figure 6-5: Microcracks on a VERTICAL specimen. Crack grown from top to bottom of figure

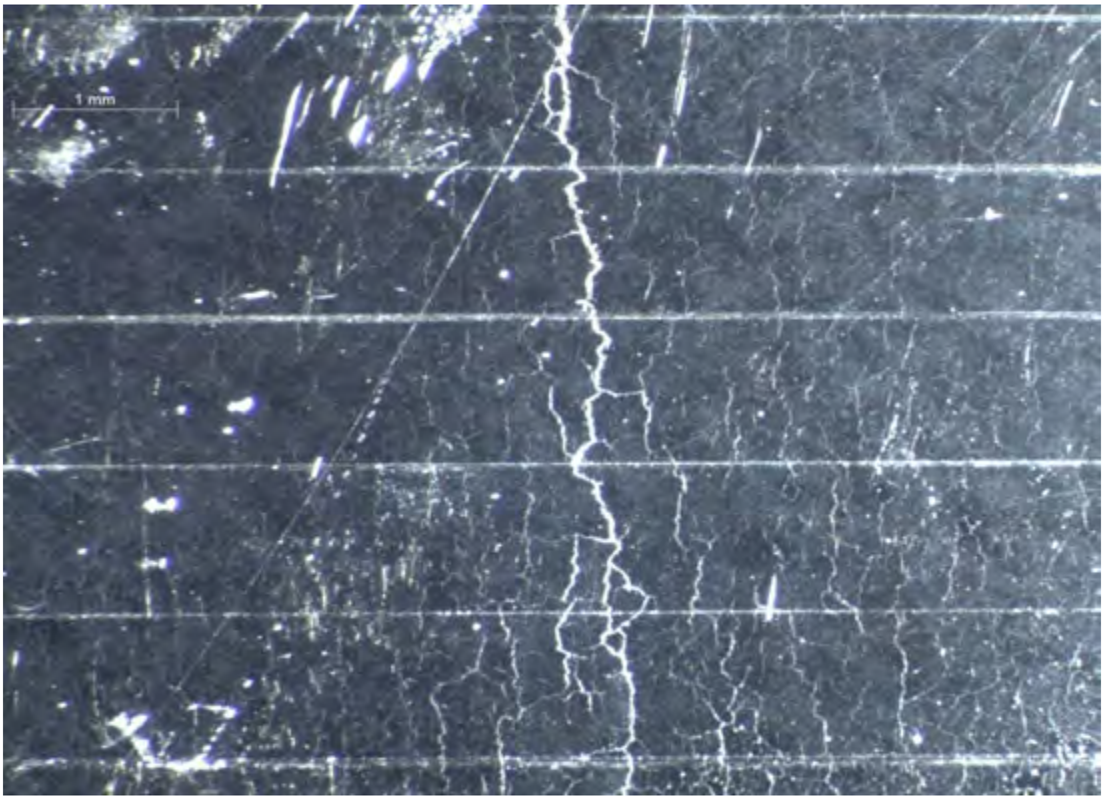

Figure 6-6: Microcracks on specimen VERTICAL – 1. Main fatigue crack in the centre, grown from top of figure.

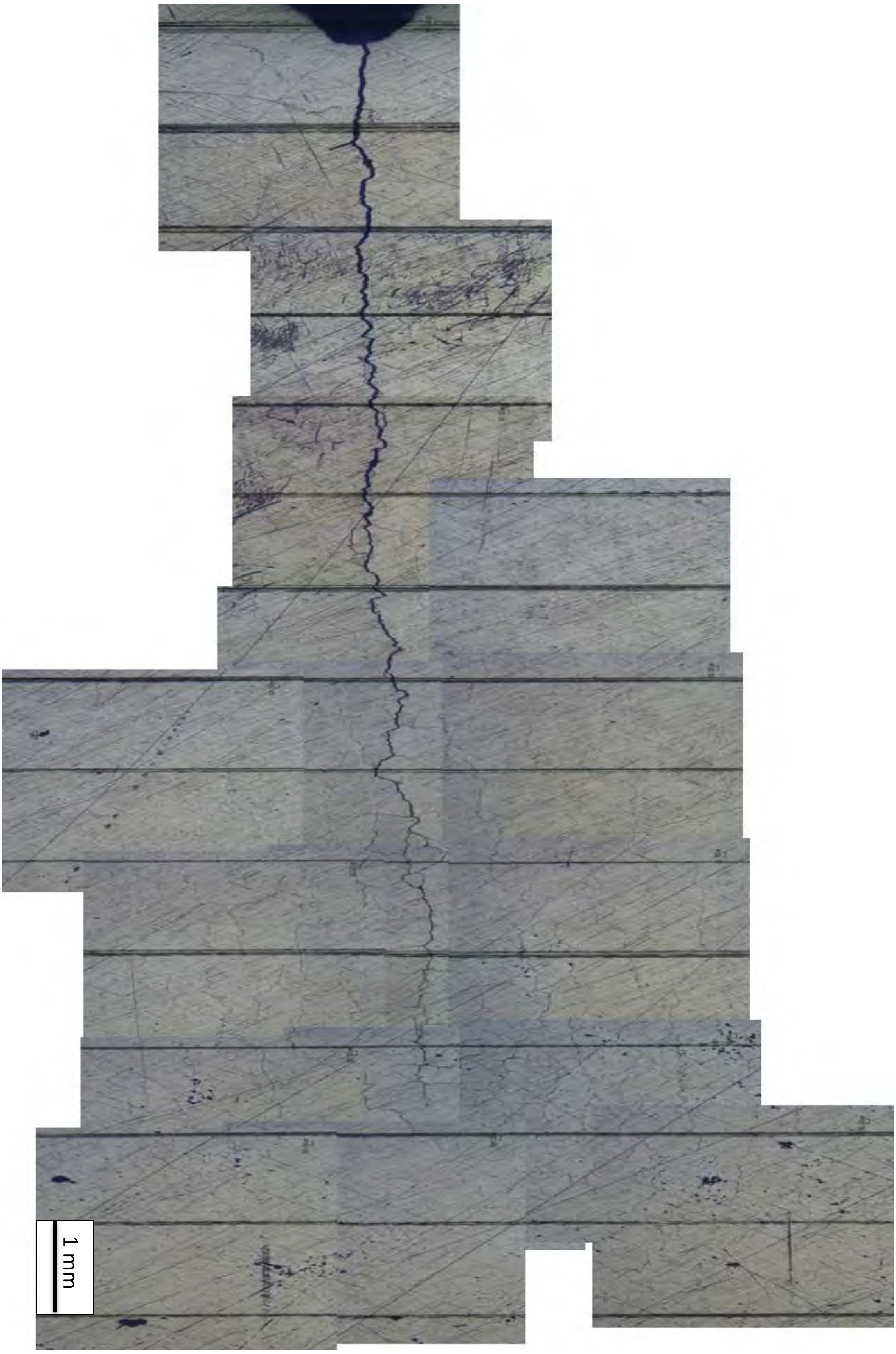

Figure 6-7: Microcracks on specimen VERTICAL – 1. Main fatigue crack in the centre, grown from top of figure.

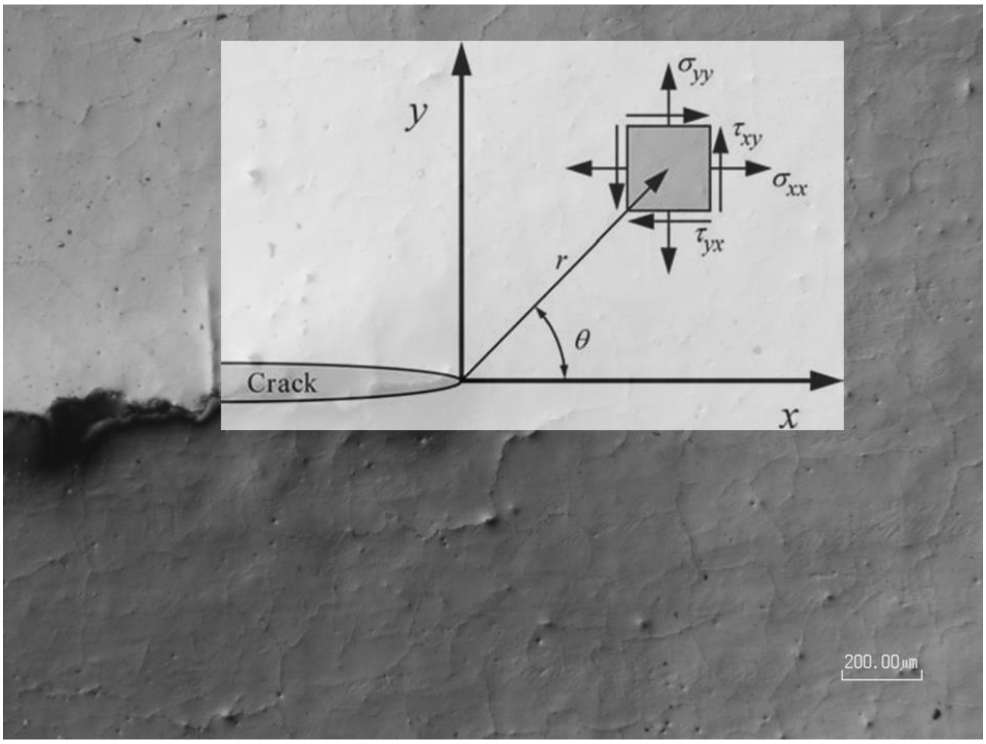

Figure 6-8: Crack tip stress analysis method [65]

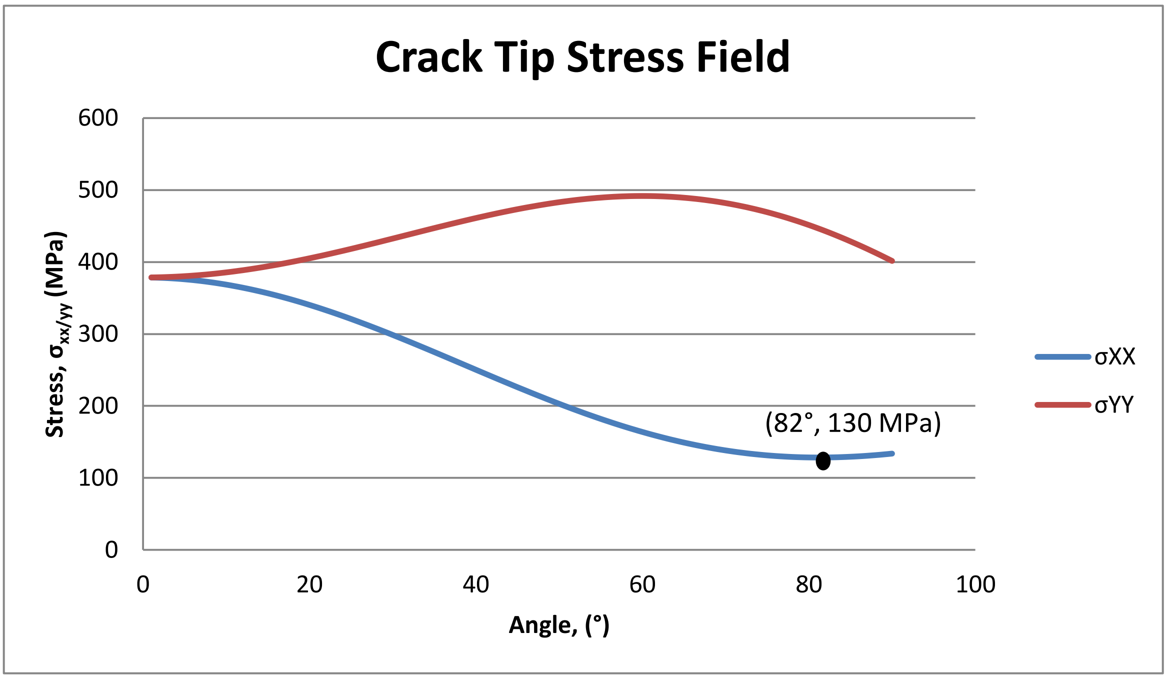

Figure 6-9: Crack tip stress field analysis

Figure 6-9 shows that the lowest σ_{xx} stress reached has a magnitude of approximately 130 MPa at 82° from the crack path direction, at a radius of 1mm ahead of the crack tip. This means that microcracks were opening at stresses as low as 130 MPa.

In Chapter 5 it was mentioned that testing on specimen EDGE – 2 could not be completed. This was due to the fact that the microcracks had become so abundant that it was virtually impossible to identify a single propagating crack tip and record the fatigue crack growth rate any further. The microcracks would appear all around the main fatigue crack, ahead of the fatigue crack as well and at times would bridge together to form larger cracks. It should also be mentioned that the results from the density testing show that specimen EDGE – 2 had a relative density of 98.53% which is approximately 1% below any other specimen within this project. Due to the lower measured density and thus larger amounts of porosity, it can be expected that larger amounts of microcracking would occur. This suggests that homogeneity in the chamber is not fully obtained, as mentioned by Edwards and Ramulu [7] that there is “a variation in porosity with location in the chamber”.

After completing the relevant calculations for the crack tip stress field, the next step was to observe the microcracks and microstructure behaviour as can be seen in Figure 6-10. The microcracks are seen to propagate through individual grains (trans-granular/cleavage fracture) as well as propagate in various directions. It is possible that due to the microcracking and possible energy dissipation away from the main crack front caused the VERTICAL and EDGE specimens to fast fracture at higher SIF’s than the FLAT specimens. In all of the VERTICAL and EDGE specimens, microcracking was observed, but only in the specimen with a rather low density compared to the rest of the specimen densities had intensified microcracking phenomena, namely specimen EDGE - 2. It may be argued that low densities exacerbate the microcracking problem. There is uncertainty on whether or not these microcracks formed as part of the manufacturing process(such as those mentioned in the previous section) and propagated when the stress in the region had increased during testing or if there are other factors which are causing these microcracks to initiate and grow.

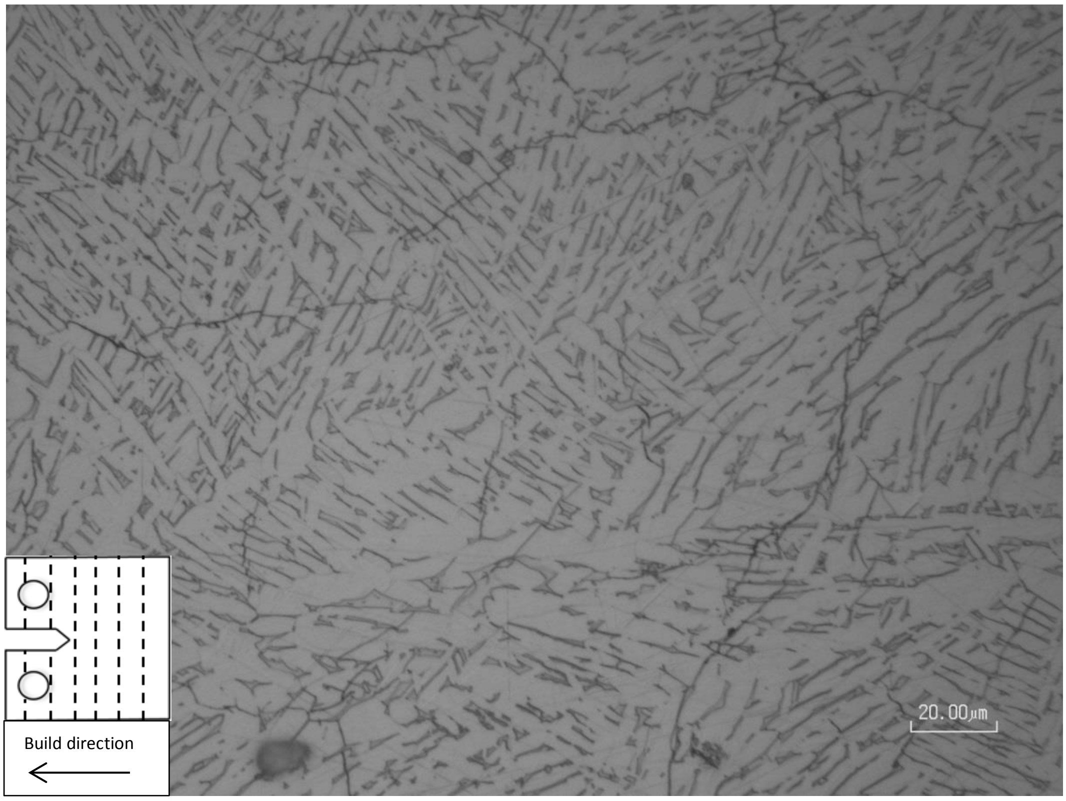

Figure 6-10: Microstructure and microcrack behaviour

It should be noted that both the VERTICAL and EDGE specimens have higher build heights than the FLAT specimens. According to Mercelis et al [61], the effect of residual stress on build height is that the higher the build height, the larger the residual stress. If the VERTICAL and EDGE specimens had larger residual stresses than the FLAT specimen, it is possible that due to the larger residual stresses during manufacture, the microcracks had formed. It is thus worth investigating the damage, if any, caused by residual stress on SLM parts after manufacture rather than only focussing on the measurement and relieving techniques.

6.1.2 Heat Treatments

This portion of the discussion focuses on the effect of different heat treatments on the fatigue crack growth rate behaviour of SLM Ti-6Al-4V. No research could be found in literature that compares different microstructures in SLM Ti-6Al-4V, i.e. lamellar, equiaxed and bi-modal, with respect to fatigue crack growth rates. However, work on this was conducted on wrought Ti-6Al-4V. To date, the only fatigue crack growth rate on SLM products found in literature is that of Van Hooreweder [6] and Leuders et al [5]. Leuders [5] describes that the microstructures of the treated specimens have a lamellar shape but of varying sizes due to the different heat treatments while the work of Van Hooreweder [6] uses as-built specimens which has a martensitic microstructure.

Although the specimens for this MSc project were not manufactured under the same scanning parameters as that of Leuders and Van Hooreweder nor have undergone the same heat treatments and possibly had not the same chemical composition of the Ti-6Al-4V powder, it is of benefit to observe the similarities and differences of these variously manufactured SLM Ti-6Al-4V with respect to fatigue crack growth rates.

The da/dN vs. ΔK used in this project has a scale for crack growth rate from 10^{-08} to 10^{-05} m/cycle and cyclic stress intensity between 10 and 100 MPa.m$^{0.5}$. The same scale will be taken from the literature graphs and superimposed onto the projects results. This may be seen in Figure 6-11 and Figure 6-12.

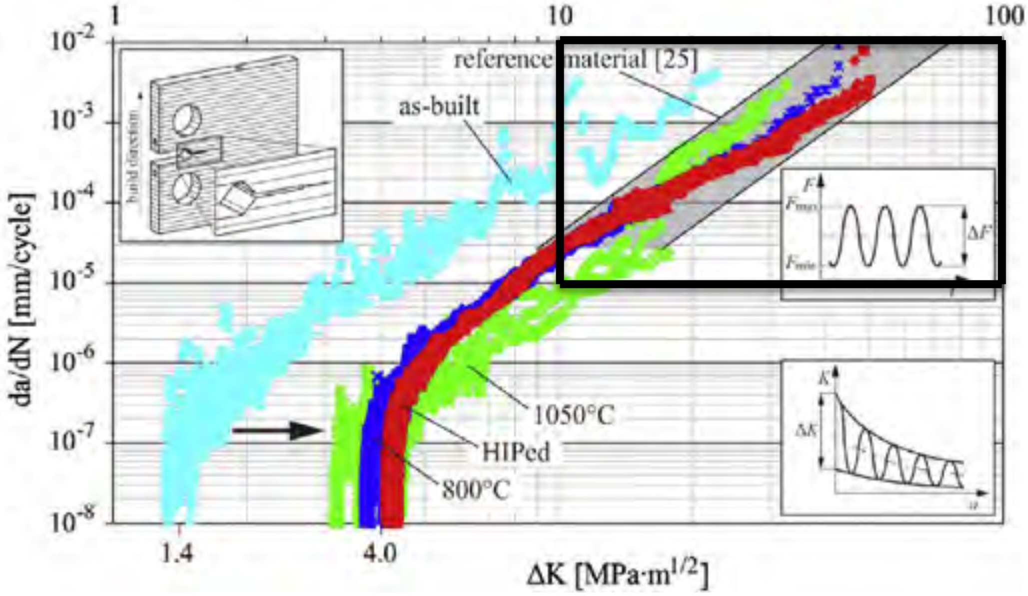

Figure 6-11: The portion of Figure 3-2 required for comparative analysis [5]

The portion of the graph contained within the black perimeter is the portion of interest. This will be superimposed onto the results obtained from this MSc research project in which the results may be compared. This comparison method will occur for the remaining orientation in the Leuders et al [5] paper as well as that of van Hooreweder [6].

Figure 6-12 compares the FLAT orientation fatigue crack growth rate specimens with that conducted by Leuders et al. [5]. The FLAT orientation and the orientation it is compared with in Figure 6-12 are not the same orientation (different crack plane), but they both have their cracks grown perpendicular to build orientation. The figure shows that the FLAT specimens behave nearly identically to the HIPed (red) processed SLM specimens and very similar to the heat treated at 800°C (blue). This reinforces the comparatively better crack growth rate of the FLAT orientation over the VERTICAL and EDGE orientations as the HIPed and heat treated at 800°C specimens behaved similarly and had minimal scatter within the Paris regime (identified by the slower crack growth rate).

Furthermore, Leuders et al [5]includes a scatter band (black diagonal parallel lines) on the Paris curve so that the SLM Ti-6Al-4V fatigue crack growth rate results may be compared with conventionally manufactured Ti-6Al-4V. It has not been specifically mentioned which conventional manufacturing methods the crack growth rate scatter band was obtained from, nor microstructural states. Typically, the fracture toughness and fatigue crack growth rate of Cast Ti-6Al-4V is superior to that of wrought Ti-6Al-4V [8]. However, this scatter band still gives confidence in the SLM results as the fatigue crack growth rate results for the FLAT specimens lie within the reference material scatter band. This result then achieves one of the main aims to the project as the fatigue crack growth rate of SLM Ti-6Al-4V has results which lie within the same regions as conventionally manufactured Ti-6Al-4V.

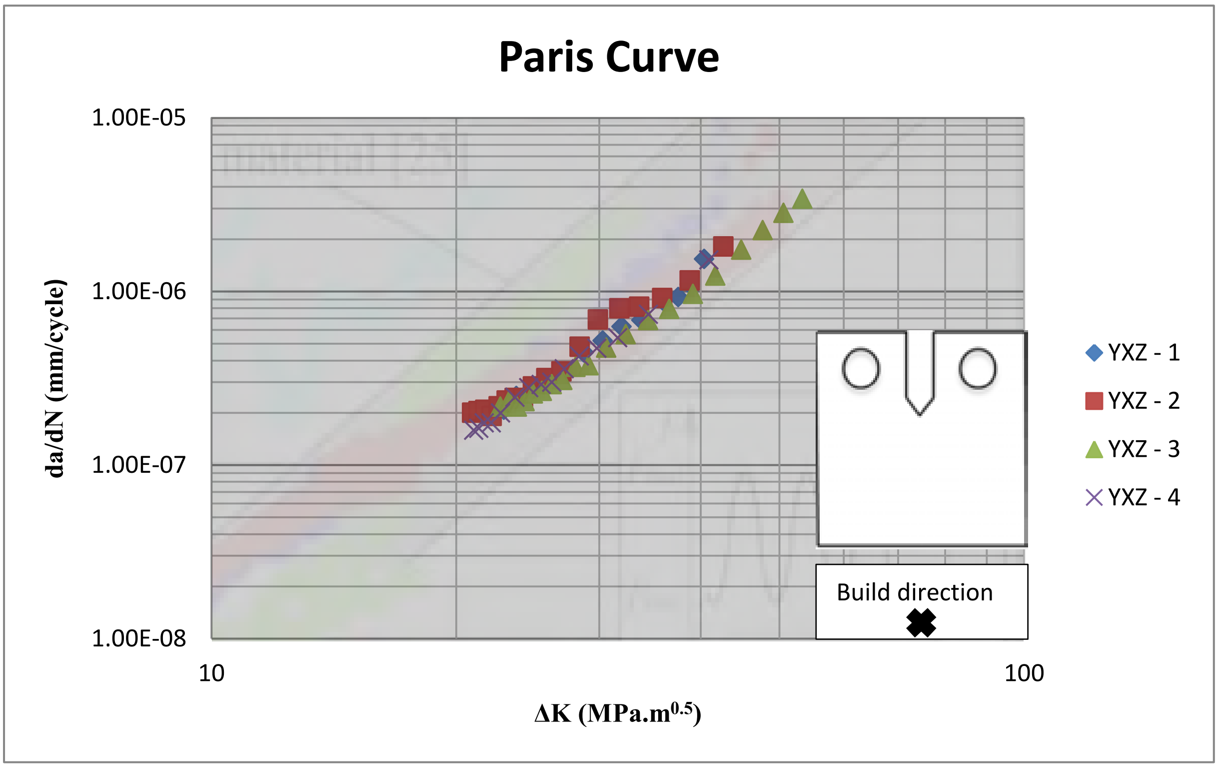

Figure 6-12: Fatigue crack growth rate comparison between FLAT specimens and Leuders et al [5] perpendicular to build direction specimens.

A better comparison between the works from this MSc project and that of Lueders et al [5] is to compare the same orientations i.e. VERTICAL with crack growth parallel to build direction and EDGE with crack growth perpendicular to build direction. The comparison made in Figure 6-13 shows that the VERTICAL specimens have a very similar behaviour to the heat treated at 1050°C specimens. As with the heat treated at 1050°C specimens, the VERTICAL specimens Paris regime lie at the boundary of the scatter band with some data points lying outside of the scatter band. This slightly decreases the confidence levels in the VERTICAL orientations fatigue crack growth rate behaviour as its behaviour is not as good as that of conventional material (for this specific scatter band). However, this does not completely eliminate the VERTICAL orientation from a fatigue crack growth rate behaviour's point of view as a closer inspection on Leuders et al's work [5] exhibits that with the HIPed and heat treated at 800°C specimens, the fatigue crack growth rate behaviour resides within the reference material scatter band. Although large scatter is prominent with this orientation, there is no real certainty as to why the scatter is so large as well as positional changes on the graphs for the same heat treatments but different build orientations, when compared to the fatigue crack growth rate data of this MSc project.

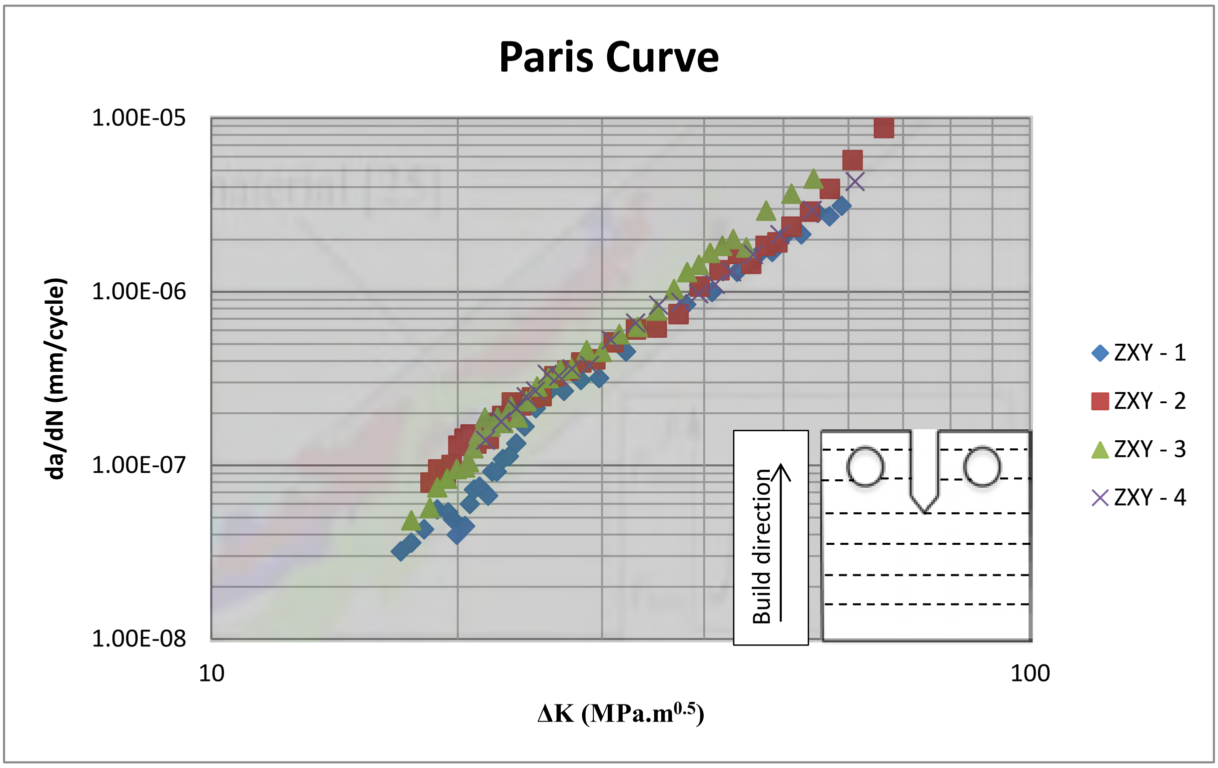

Figure 6-13: Fatigue crack growth rate comparison between VERTICAL specimens and Leuders et al [5] parallel to build direction specimens.

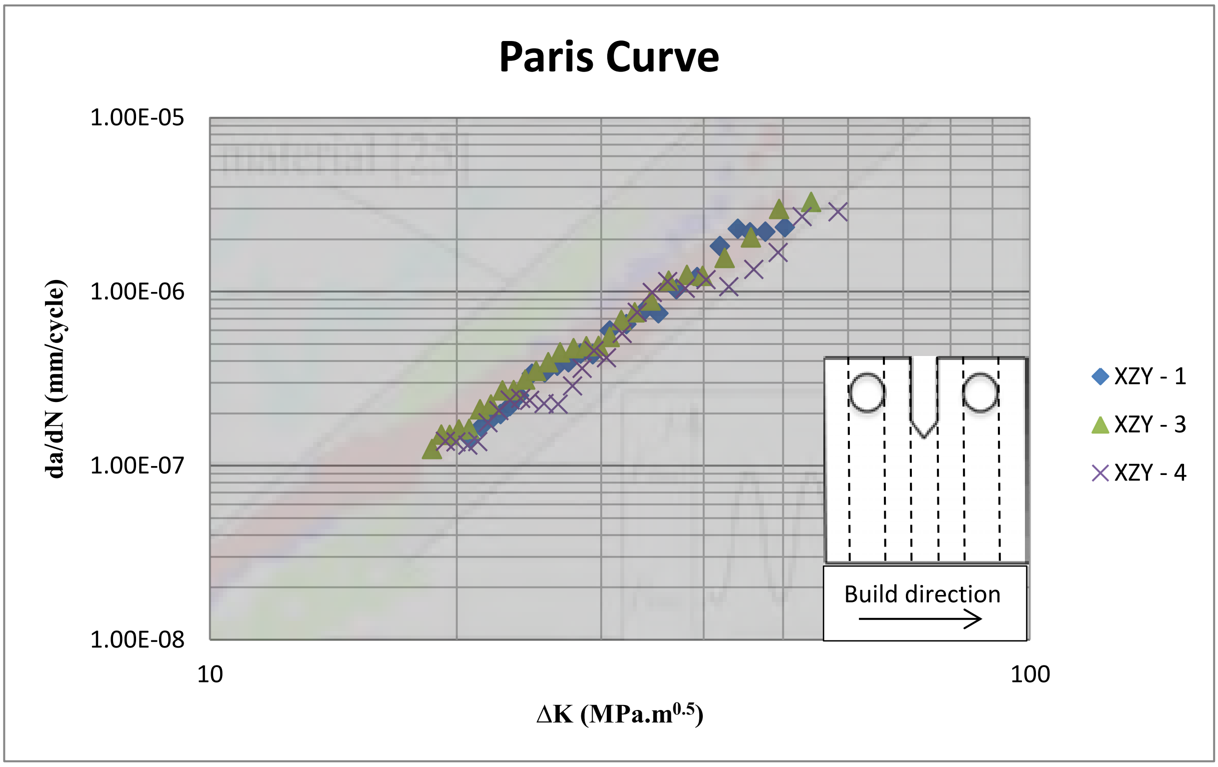

Figure 6-14: Fatigue crack growth rate comparison between EDGE specimens and Leuders et al [5] perpendicular to build direction specimens.

The EDGE specimens behaviour very closely follows that of the HIPed and heat treated at 800°C specimens, seen in Figure 6-14. It is not understood why specimen EDGE – 4 has a wave-like pattern in its crack growth behaviour, which causes some data points to lie outside of the reference material scatter band. Comparing all three orientations of this MSc research project with the works of Leuders et al [5], it shows that orientations FLAT, VERTICAL and EDGE lie in very similar regions of the scatter band (closer to the lower boundary), whereas Leuders et al's [5] specimens seems to change position within the scatter band for the same stress relieving condition but different orientation. This behaviour is not particularly understood but reasons may lie with the fact that different scanning parameters, machines, powder chemical composition and sizes were used and not only due to porosities, microstructure and residual stress. Thus requiring further investigation into orientation effects on fatigue crack growth rate behaviour.

Comparing the work of Van Hooreweder [6] with the results obtained in this research project is briefly done as superimposing the graphs onto each other seems too cluttered with its current setup. It is only the Paris parameters which will be compared. It should be noted that the work of Van Hooreweder [6] is not stress relieved as well as only in a single orientation. Indicated in Table 6-2 are the Paris parameters comparison of the work conducted by Van Hooreweder [6] and from this research project. The m-values are close to each other in all orientations but with the VERTICAL orientation having the largest spread in individual values. The C-values are in the same order of magnitude i.e. x10^{-12}, except for the EDGE orientation which has the magnitude of x10^{-11}. These spreads in C and m-values may be attributed to the orientation effects which are not fully understood.

Table 6-2: Paris parameters comparison of Van Hooreweder [6] and current project.

	Van Hooreweder [6]	FLAT	VERTICAL	EDGE
C (m/cycle)	5 x 10^{-12}	7.95 x 10^{-12} ± 0.99 x 10^{-12}	4.88 x 10^{-12} ± 5.38 x 10^{-12}	14.1 x 10^{-12} ± 5.64 x 10^{-12}
m	3.376	3.25 ± 0.02	3.52 ± 0.38	3.10 ± 0.15

Of the SLM fatigue crack growth rate behaviour that is available in literature at present, the results obtained within this research project displays similar results. Comparing these projects results with that of the reference material scatter band, a large portion of the results lie within the scatter with a few data points on the outside. This is also prevalent in the works of Leuders et al [5]. His work also suggests that with different heat treatments or HIP conditions, fatigue crack growth rate data may lie well within the reference Paris regime scatter band. Although these comparisons have shown acceptable results, it is worth comparing the results of this research project to other conventionally manufactured Ti-6Al-4V found in literature.

6.2 Fracture Toughness

The fracture toughness results have demonstrated that there is a minimal variation in fracture toughness values with respect to build orientation. The fracture toughness values for the FLAT, VERTICAL and EDGE are 74.99 ± 0.99 MPa.m$^{0.5}$, 75.66 ± 0.36 MPa.m$^{0.5}$ and 79.57 ± 1.05 MPa.m$^{0.5}$ respectively. The EDGE specimens has an approximately 5% higher fracture toughness value than the other orientations. The slightly higher fracture toughness value of the EDGE orientation may lie with the fact that there was a different fracture surface observed after testing. It is not clear as to why the EDGE orientations specimen have a very different fracture surface than the FLAT and VERTICAL orientations, but this was also observed in the fatigue crack growth profile seen in Figure 6-1. It is possible that due to the microstructure orientation and the manner in which the fatigue crack interacts with it, that it may cause the difference in fracture surface. Currently, the reason for a higher fracture toughness value remains an assumption and will require further analysis such as fractography to help understand this behaviour.

Table 6-3 summarises fracture toughness values found in literature.

Table 6-3: Fracture toughness comparison

Ti-6Al-4V Condition	**Fracture Toughness (MPa.m$^{0.5}$)**
VAR, mill annealed [6]	69.98 ± 3.53
SLM [6]	52.4 ± 3.48
SLM – FLAT	74.99 ± 0.99
SLM – VERTICAL	75.66 ± 0.36
SLM – EDGE	79.57 ± 1.05

Comparing the SLM Ti-6Al-4V of this project with that from Van Hooreweder’s [6] work, it shows that each orientation has superior fracture toughness values as well as a lower spread from the average fracture toughness value per an orientation. It is not clear why the fracture toughness of Van Hooreweder’s [6] specimens is lower than that obtained for this project. However, it is possible that due to the specimens being in the as-built condition and built under a different set of manufacturing parameters that it causes a reduced fracture toughness performance. The SLM – FLAT and VERTICAL orientation and SLM – EDGE orientation approximately has a 30% and 34% greater toughness than that quoted by Van Hooreweder [6], respectively. The VAR specimens used by Van Hooreweder [6] has similar trends that can be observed. The SLM – FLAT and VERTICAL orientation and SLM – EDGE orientation approximately has a 6% and 12% greater toughness than the VAR material.

6.3 Industrial Application

As mentioned earlier in the literature review, Ti-6Al-4V accounts for approximately 45% of the total weight of shipped titanium and will continue to be the most used alloy for many years to come [8]. As a result, wrought Ti-6Al-4V has become the standard comparison when selecting other titanium alloys for applications and when superior strength such as high ultimate tensile strength and yield strength are required for an application, cast Ti-6Al-4V is the standard comparison [8]. It then makes sense to compare the SLM Ti-6Al-4V with that of wrought and cast Ti-6Al-4V in order to understand where SLM Ti-6Al-4V stands in relation to Ti-6Al-4V used in industry already.

To compare the fatigue crack growth rate data, a scatter band was formulated for all the SLM Ti-6Al-4V orientations of this project rather than reproducing the graph three times over for the different orientations. Figure 6-15 and Figure 6-16 compares the SLM Ti-6Al-4V with that of conventional Ti-6Al-4V.

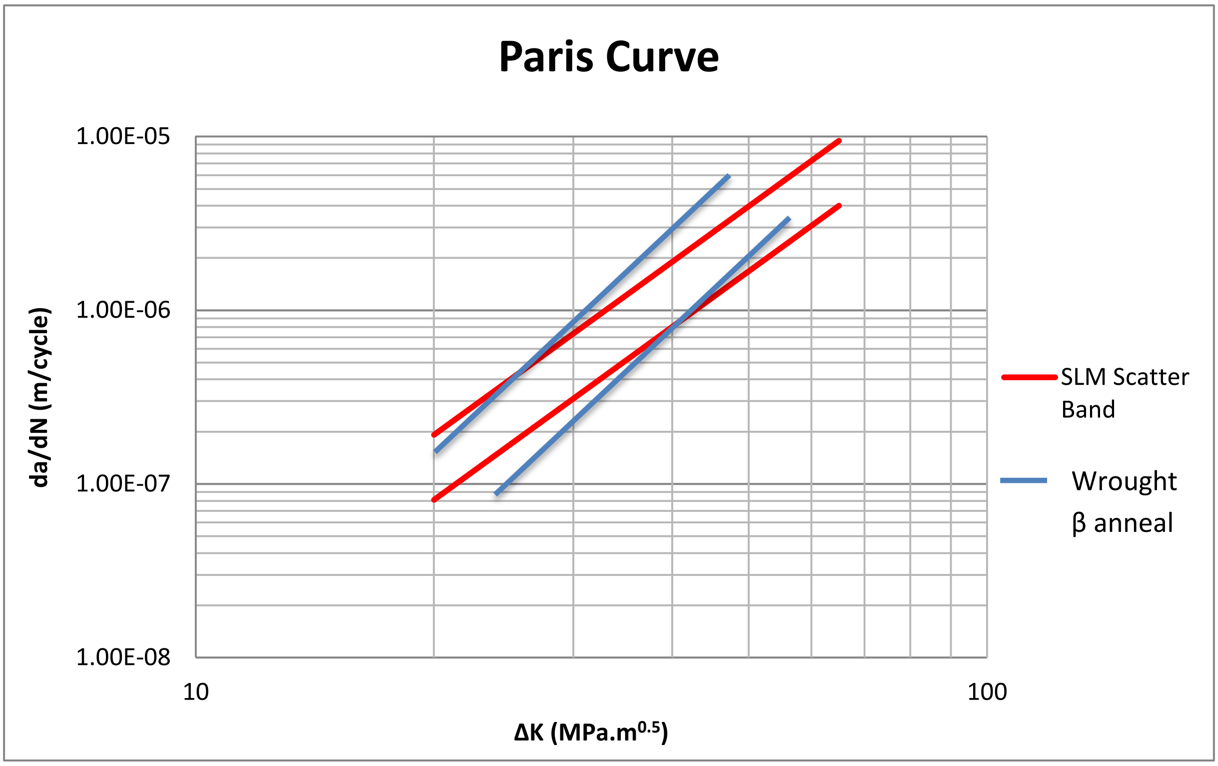

Figure 6-15: Fatigue crack growth rate comparison between SLM Ti-6Al-4V scatter band and wrought alloy [8]

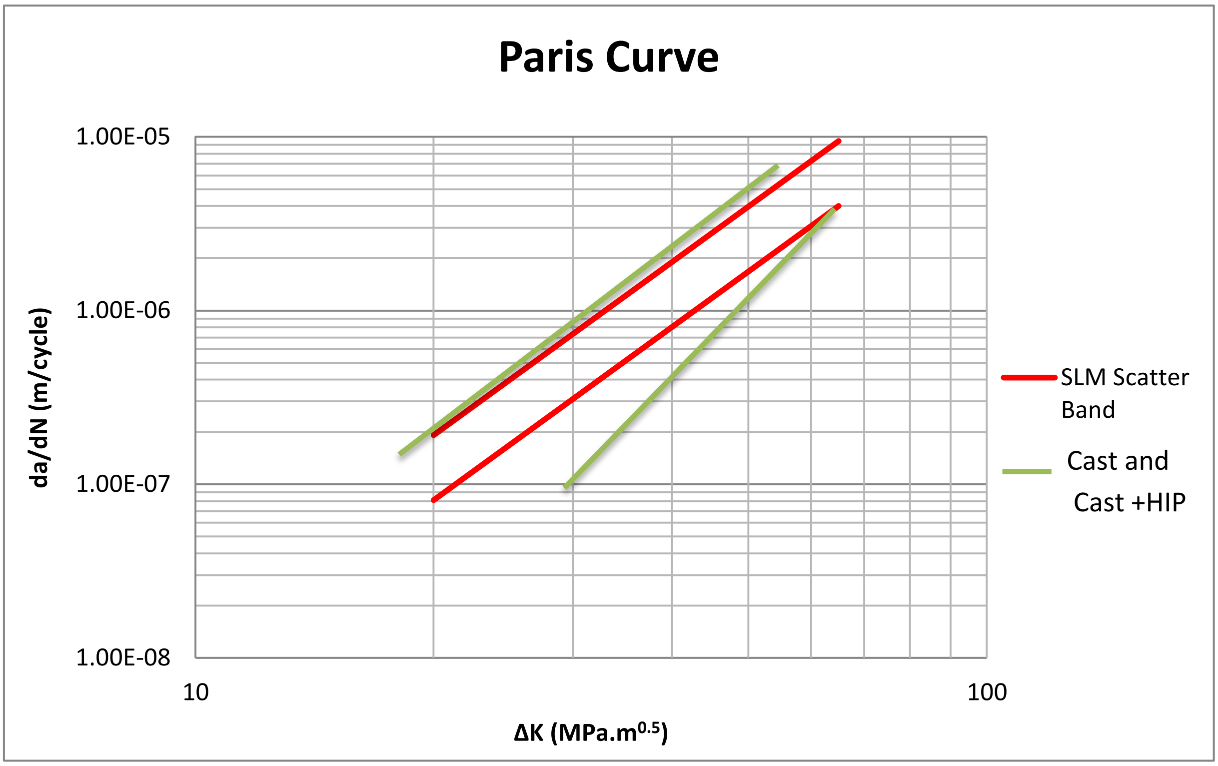

Figure 6-16: Fatigue crack growth rate comparison between SLM Ti-6Al-4V scatter band and cast and cast + HIP [8]

The SLM manufactured products again suggest having acceptable crack growth behaviour as they largely lie within wrought and cast scatter bands as seen in the above figures. In these instances, the cast and cast + HIPed scatter band envelopes the SLM Ti-6Al-4V scatter bands, which strongly reinforce the acceptable crack growth behaviour of SLM Ti-6Al-4V. The cast and cast + HIPed contain a wider range of crack growth rates for a given cyclic SIF than both wrought and SLM Ti-6Al-4V. It also has lower fatigue crack growth rates than both wrought and SLM Ti-6Al-4V. It is possible that a duplex annealed wrought Ti-6Al-4V has a fatigue crack growth rate scatter band which largely overlaps with the SLM Ti-6Al-4V scatter band, but this has not been found elsewhere in literature and so the comparison may not be made. These findings then suggest that from a purely fatigue crack growth rate point of view, SLM Ti-6Al-4V has acceptable behaviour for certain industrial applications which use wrought β-annealed, cast and cast +HIPed Ti-6Al-4V in its application. With the aerospace industry being the largest consumer of Ti-6Al-4V, it stands to benefit the most from SLM Ti-6Al-4V if it were to be accepted as a viable manufacturing option. Many of the complex components used in the aerospace industry, such as the turbine engine turbines and disks are manufactured via casting methods. As it stands presently, SLM Ti-6Al-4V does not fully match the lower fatigue crack growth rate behaviour of cast Ti-6Al-4V. Although the SLM Ti-6Al-4V has acceptable fatigue crack growth behaviour, from a design and safety aspect, this is not the case with the material as there is still a lack of understanding with respect to the orientation effect as well as microcracking propagation. The purpose of obtaining a Paris equation is to make fatigue life prediction estimates in which crack lengths are obtained from NDT methods. If the microcracking behaviour is to persist, this may hinder the crack measuring techniques used in NDT.

Comparing the fracture toughness results to that found in literature proved to be challenging as there are various quoted fracture toughness values for Ti-6Al-4V, but for which no microstructural information is given. It would be of great benefit if information such as heat treatment temperatures, heating rates, cooling rates were given and specific microstructures etc., so that testing conditions may be reproduced. This will particularly be useful when trying to compare SLM products with that of conventional (wrought and cast) material. Currently as it is, the heat treatments given in the table below are just types of heat treatments, which may be conducted at different temperatures but within a certain range, with different heating/cooling rates, and holding times etc. It is too broad to make an accurate comparison but will at least give a general idea of how SLM Ti-6Al-4V compares with that of conventional Ti-6Al-4V with respect to fracture toughness. It was then decided to compare it with the values from the Titanium textbook by Donachie [8].

Table 6-4: Fracture toughness comparison

Ti-6Al-4V Condition	Fracture Toughness (MPa.m$^{0.5}$)
Wrought bar, recrystallization anneal [8]	52
Wrought bar, beta anneal [8]	91
Cast bar, as cast [8]	107
Cast bar, annealed [8]	103
Cast bar, HIP [8]	109
SLM – FLAT (This study)	74.99 ± 0.99
SLM – VERTICAL (This study)	75.66 ± 0.36
SLM – EDGE (This study)	79.57 ± 1.05

As seen in Table 6-4, the Cast Ti-6Al-4V has superior fracture toughness values than the wrought Ti-6Al-4V. The SLM products of this project have an approximately 27% inferior toughness to that of Cast Ti-6Al-4V. However, the SLM products fall within the wrought Ti-6Al-4V range of fracture toughness values for the recrystallization and beta anneal heat treatments. One of the outcomes of using the β-anneal is a higher fracture toughness, as seen in Table 6-4, although there is a some loss in ductility [8]. Due to the duplex anneal heat treatment being used as it gives an optimum balance of ductility, fracture toughness and other properties over the β-anneal heat treatment, it would suggest that the duplex annealed SLM Ti-6Al-4V should have lower fracture toughness than the β-anneal, but higher than the recrystallization anneal. This is the case as the SLM duplex annealed Ti-6Al-4V has an approximately 32% greater fracture toughness than wrought recrystallization annealed Ti-6Al-4V and approximately 16% inferior fracture toughness than the wrought β-anneal Ti-6Al-4V. It is worth investigating the fracture toughness of SLM Ti-6Al-4V that has under gone the β-anneal and recrystallization anneal to compare it with the results of this project as well as the wrought materials under the same heat treatments. The recrystallization anneal heat treatment is also used for fracture critical airframe components and so it would be of great benefit for SLM products to be tested under this heat treatment [8].

Although this project focuses on fatigue crack growth rate and fracture toughness which are crucial for structural aircraft components, the fatigue strength, the yield strength, tensile strengths and ductility of materials are also important mechanical properties for designing a component. The fatigue, yield and tensile strength of SLM Ti-6Al-4V were not investigated in this project, but are found in literature and are shown in Table 6-5.

Table 6-5: Fatigue life of SLM Ti-6Al-4V found in literature

		Fatigue Life (cycles to failure)	Stress (MPa)
Simonelli [91]	**Stress Relieved**	24775 ± 4019.6	500
Leuders et al [5]	**As-built**	27000	600
	Stress relieve 1	93000	
	Stress relieve 2	29000	
	HIPed	2000000	
Edwards and Ramulu [7]	**X – orientation (as-built)**	≈ 200000	240
	Y - orientation (as-built)	≈ 200000	170
	Z – orientation (as-built)	≈ 200000	100

The table above shows that when considering the as-built conditions of SLM Ti-6Al-4V, the fatigue life of the material is at its weakest state when compared to that of the stress relieved conditions. This is due to the large as-built residual stresses, microstructure and porosities which all favour crack initiation. Once the material is stress relieved, the crack initiation sensitivity is reduced and increases the fatigue strength. Due to the stress relieving techniques, the fatigue strength of SLM Ti-6Al-4V performs as well as conventionally manufactured Ti-6Al-4V while the as-built conditions do not obtain satisfactory performance, as shown in Figure 6-17.

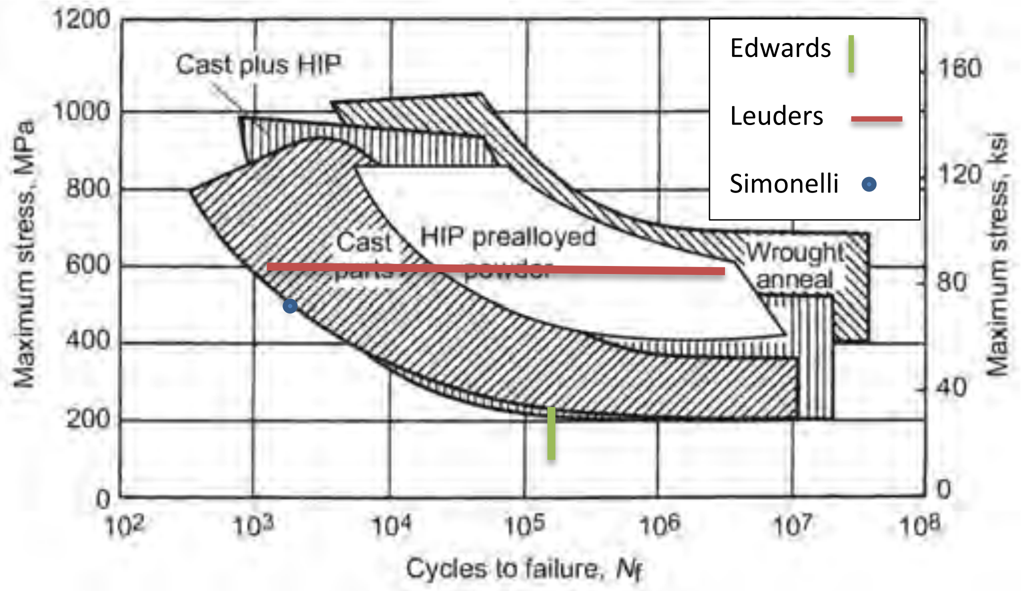

Figure 6-17: Fatigue life comparison [8].

The SLM tensile properties are compared with results found in the Donachie textbook as well as the ASTM F1108 and F1472 which are the specifications for Ti-6Al-4V of casting and wrought surgical implants respectively. The F1472 has a range of tensile values depending on the size and whether or not the material is a sheet, plate, strip, bar etc.

Table 6-6: Comparison of mechanical properties

		σ_y (MPa)	UTS (MPa)	ε Fracture (%)	Fracture Toughness (MPa.m$^{0.5}$)
Simonelli [91]	**xz – as built**	978 ± 5	1143 ± 6	11.8 ± 0.5	-
	zx – as built	967 ± 10	1117 ± 3	8.9 ± 0.4	-
	xy – as built	1075 ± 25	1199 ± 49	7.6 ± 0.5	-
	xz – stress relieved	958 ± 6	1057 ± 8	12.4 ± 0.7	-
	zx – stress relieved	937 ± 9	1052 ± 11	9.6 ± 0.9	-
	zx – stress relieved	974 ± 7	1065 ± 21	7.0 ±	-
SLM (This project)	**FLAT**	-	-	-	74.99 ± 0.99
	VERTICAL	-	-	-	75.66 ± 0.36
	EDGE	-	-	-	79.57 ± 1.05
Van Hooreweder [6]	**-**	-	-	-	52.4 ± 3.48
Leuders et al [5]	**As-built**	1008	1080	1.6	-
	Stress relieve 1	962	1040	5	-
	Stress relieve 2	798	945	11.6	-
	HIPed	912	1005	8.3	-
Edwards and Ramulu [7]	**As-built**	910 ± 9.9	1035 ± 29	3.3 ± 0.76	-
Donachie [8]	**Mill annealed**	945	1069	10	-
	Duplex annealed	917	965	18	-
	Solution treated and aged	1103	1151	13	-
	Wrought bar	-	-	-	52
	Wrought bar	-	-	-	94
	Cast bar	-	-	-	103-109
ASTM	**Cast implants – F1108**	> 758	> 860	> 8	-
	Wrought implants – F1472	> 825 – 869	> 895 – 930	> 6 – 10	-

Table 6-6 shows that the as built specimens have higher yield and tensile properties while typically having lower ductilities than the stress relieved specimens. Depending on the manufacturing parameters, the as-built mechanical properties may differ, as seen by the difference in ductility of Simonelli [91], Leuders et al's [5], and Edwards and Ramulu [7] specimens. However, when the as-built martensitic acicular microstructure is transformed into structures such as lamellar, bi-modal or equiaxed, there is an increase in ductility of the material which leads to better crack initiation resistance thus increasing the required threshold stress for crack propagation [8]. Simonelli's work [91] shows that there is anisotropic behaviour present, which is particularly noticed in the ductility of the material, in both the as-built and stress relieved condition. The results also show that the yield, tensile strengths and ductility of SLM Ti-6Al-4V are higher than most and in a similar range to that of conventional manufactured material as well as that required by the ASTM standards for surgical implants. Simonelli [91] explains that the reason for the higher yield and tensile strength of the as-built SLM Ti-6Al-4V is due to the smaller α colony size in the microstructures which delays the onset of plastic deformation. These colony sizes are equal to the width of a single α lath.

Overall, the SLM Ti-6Al-4V displays mechanical properties that are as good as and in certain cases better than conventionally manufactured Ti-6Al-4V. These results show great promise for SLM Ti-6Al-4V as the post manufacture heat treatments prove to be of great benefit and produce acceptable mechanical properties. Based on the findings i.e. fatigue crack growth rate, fracture toughness as well as the yield and tensile properties, SLM Ti-6Al-4V which has been post-build heat treated demonstrates that the SLM process may be a viable manufacturing option for certain applications. However, due to the current lack of understanding of orientation effects, from a design and safety aspect, further investigation is required into these behaviours before any form of major manufacturing takes place.

Future Work

When considering the three regions in a fatigue crack growth rate curve, which are divided into crack initiation (threshold), crack propagation (Paris regime) and fast fracture (fracture toughness), this MSc research project analysed the Paris regime (log-log linear region) and fracture toughness. It is of great interest to carry out research on SLM Ti-6Al-4V in order to analyse the crack propagation threshold which will then complete the investigation into the fatigue crack growth rate curve of SLM Ti-6Al-4V. A further aspect which requires investigation is that of the microcracking behaviour common in the VERTICAL and EDGE orientation.

Since the SLM process inherent flaws in its products such as porosities which may act as crack initiation sites, it is of utmost importance that the critical level of microstructural flaws which may cause failure be identified [92]. Ritchie et al [92] mentions that short crack (dimensions comparable to microstructure or plastic zone size) can grow faster than large cracks which experience the same applied force, as depicted in Figure 6-18. Some reasons that are mentioned as to why the small cracks behave differently to large cracks are: “1. Microstructural size scales, where biased statistical sampling of the microstructure leads to accelerated crack advance along ‘weak’ paths, i.e., microstructural features oriented for easy crack growth (a continuum or homogeneity limitation). 2. The extent of local plasticity *ahead* of the crack tip, where the assumption of small-scale yielding implicit in the use of the stress intensity SIF is not strictly valid (a linear-elastic fracture mechanics limitation). 3. The extent of crack-tip shielding (e.g. crack wedging by crack closure) *behind* the crack tip, where the reduced role of shielding leads to a higher *local* driving force than the corresponding large crack at the same SIF levels (a similitude limitation).” Ritchie et al [92] reports that no small cracks have been observed below 2.9 MPa.m$^{0.5}$. Since SLM Ti-6Al-4V behaves very similar to conventionally manufacture Ti-6Al-4V in the Paris regime, the question then arises on whether or not SLM Ti-6Al-4V would behave in the same manner in the small cracks regime as it does in the work conducted by Ritchie. Furthermore, with the orientation effects and microcracking behaviour observed in specific orientations, the question arises what impact that would have on threshold behaviour.

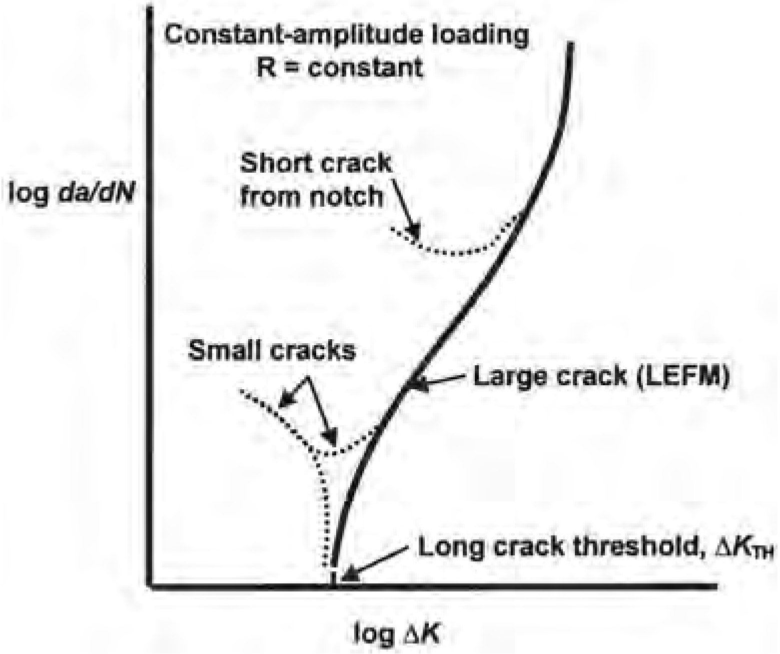

Figure 6-18: A schematic comparison of typical growth-rate behaviour for small and large cracks [92]

A study conducted by Piotrowski [93] investigated the effect of heterogeneous microstructure and residual porosity on fatigue threshold for powder metallurgy Fe-0.85Mo-2Ni-0.6C steel. Although this MSc project is not concerned with steels, the findings of Piotrowski [93] shows that the heterogeneous microstructure has a significant influence on the fatigue crack behaviour in which there are areas within the microstructure which causes crack arrest, deflection and branching. If this is the case for a powder metallurgy heterogeneous microstructure, it is possible that at threshold values, a similar behaviour may be witnessed in SLM Ti-6Al-4V as well as what effect build orientation has on fatigue threshold. Furthermore, a comparison of fatigue threshold with respect to microstructure i.e. equiaxed, lamellar and bi-modal should be analysed to observe any difference in fatigue resistance.

The next point of interest is to understand the microcracking behaviour of the VERTICAL and EDGE orientations. A relatively new analysing technique, known as digital image correlation (DIC), measures the deformation on the surface of a material by comparing images of the deforming material with an initial non-deformed state [94]. The material of interest is required to have speckled pattern applied to its surface, in order for the DIC system to track the deformation by following the movement of the speckled pattern, as seen in Figure 6-19 [95], [96].

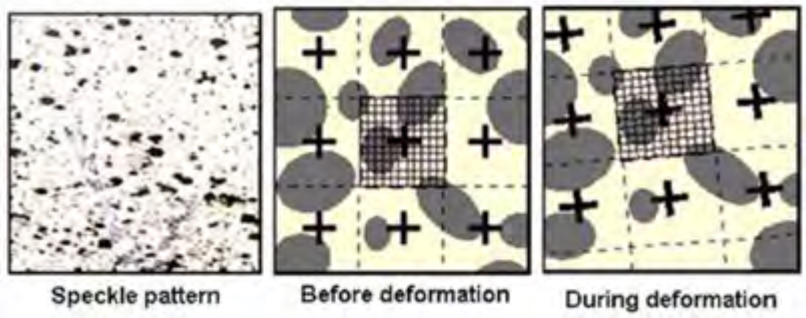

Figure 6-19: Manner in which the DIC system tracks deformation via the speckled pattern [96].

By measuring the deformation, the DIC system can be used to calculate strains, crack tip intensity and crack opening displacements, as seen in Figure 6-20 [97]. One may also apply principal stress theories such as von mises in order to calculate what the stresses are at the crack tip region and compare it to calculated values. This is also useful with the microcracking phenomena of the VERTICAL and EDGE orientations to measure if there is any energy dissipation due to the microcracking as well as measure accurately what the stress are which cause the microcracks to appear and propagate.

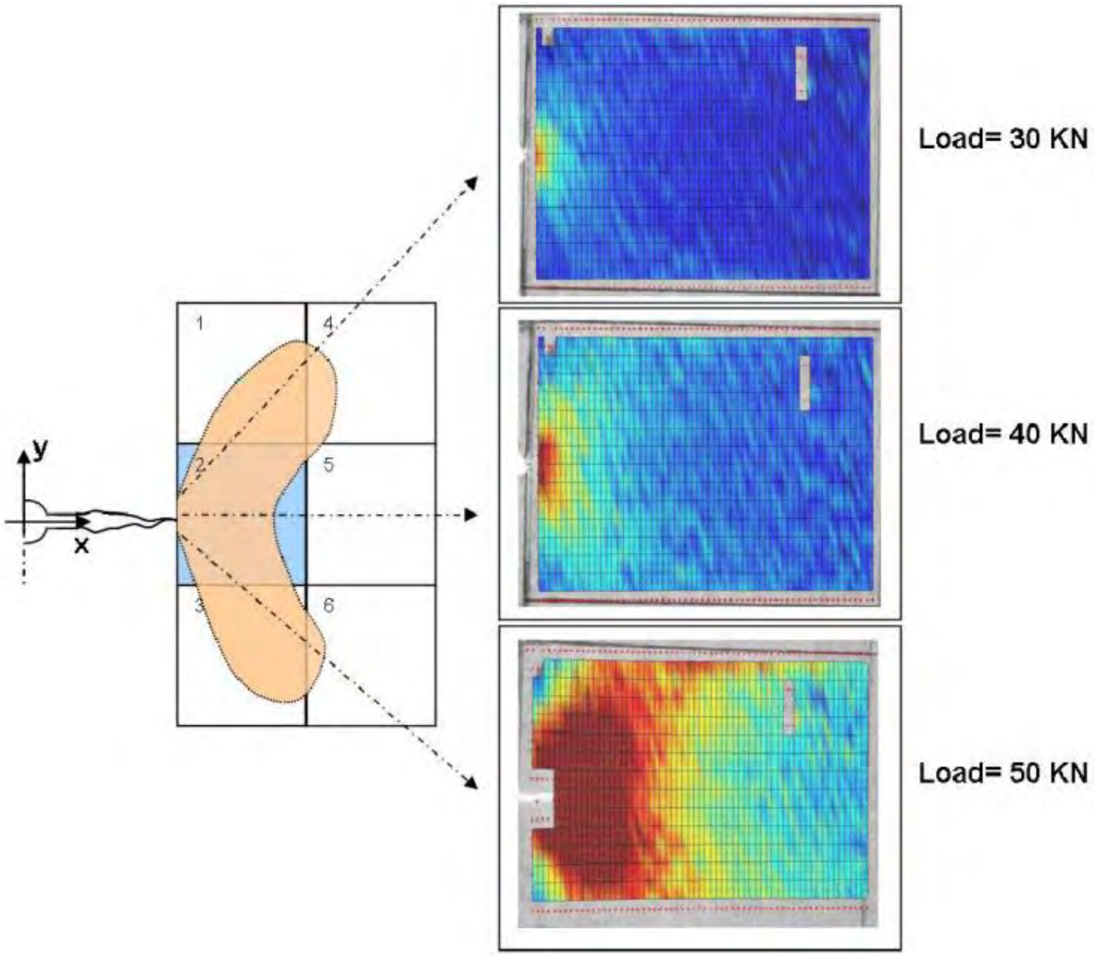

Figure 6-20: Strain field for different load levels [98]

6.4 Summary

The analysis showed that the fatigue crack growth rate of SLM Ti-6Al-4V, after stress relieving (duplex anneal), had acceptable performance although orientation effects (scatter) were noticed. It was argued that the inherent porosity, microstructure and residual stress result in orientation effects, as well as numerous manufacturing parameters. The tendency for microcracks to form and propagate in the VERTICAL and EDGE specimens may be caused by a combination of manufacturing defects, parameters and microstructure orientation.

The fracture toughness results, after stress relieving, did not show any clear anisotropic behaviour such as that displayed in the fatigue crack growth rate results. However, a clear difference on the fracture surfaces of the EDGE specimens as compared to the FLAT and VERTICAL orientation fracture surfaces were noticed. This difference may be the result of the specimen orientation, but has not been further investigated in this project.

When comparing the SLM Ti-6Al-4V mechanical properties with that of the conventional Ti-6Al-4V material, there is great promise in the material as its performance is as good as and in certain cases better than that which is required by conventional Ti-6Al-4V.

The following chapter attempts to list these key points and conclude this project.

Chapter 7 - Conclusions

This MSc research project set out to investigate the fatigue crack growth rate behaviour and fracture toughness behaviour of SLM Ti-6Al-4V titanium alloy with respect to build orientation. This research is a continuation of earlier work conducted by Knowles [1] where residual stress measurement and stress relieving was conducted and also serves as a comparison to other works in literature on SLM and Ti-6Al-4V. The key conclusions are summarised below:

- After a duplex anneal heat treatment, the fatigue crack growth rate results of SLM Ti-6Al-4V exhibited acceptable behaviour when compared to that of literature. The SLM Ti-6Al-4V behaves very similarly to conventional Ti-6Al-4V and lies within the crack growth scatter bands.

- A noticeable variation in scatter of the crack growth behaviour is observed with the various build orientations in which the FLAT has the most stable crack growth behaviour of the orientations. Variations in scatter may be caused by the crack growth interaction with the microstructure.

- The VERTICAL and EDGE orientations produced significant amounts of microcracks during fatigue crack growth rate testing.

- After a duplex anneal heat treatment, the fracture toughness behaviour of SLM Ti-6Al-4V lies within the range of wrought material. The SLM duplex annealed Ti-6Al-4V has an approximately 32% greater fracture toughness than wrought recrystallization annealed Ti-6Al-4V and approximately 16% inferior fracture toughness than the wrought β-anneal Ti-6Al-4V

- SLM Ti-6Al-4V has minimal variation in fracture toughness with respect to build orientation. The EDGE specimens have an approximately 6% higher fracture toughness value than the other orientations.

In addition to the future work discussed in Chapter 6:

- Further analysis into the build orientation effects on fatigue crack growth rate behaviour should be investigated.

- Investigating the extent of damage caused, if any, by residual stress and if there is any relation to build height.

- The EDGE specimens fracture surface should undergo fractography to analyse and understand why its fracture surface is different to the FLAT and VERTICAL specimens fracture surface.

Chapter 8 – References

[1] C. R. Knowles, “Residual Stress Measurement and Structural Integrity Evaluation of SLM Ti-6Al-4V,” University of Cape Town, 2012.

[2] S. Mellor, L. Hao, and D. Zhang, “Additive manufacturing: A framework for implementation,” *Int. J. Prod. Econ.*, vol. 149, pp. 194–201, Mar. 2014.

[3] The Economist, “Solidprint: making things with a 3D printer changes the rules of manufacturing,” *Economist*, London, Apr-2012.

[4] J. Holstrom, J. Partanen, J. Tuomi, and M. Walter, “Rapid manufacturing in the spare parts supply chain: alternative approaches to capacity development,” *J. Manuf. Technol. Manag. 21*, vol. 6, pp. 687–697.

[5] S. Leuders, M. Thöne, a. Riemer, T. Niendorf, T. Tröster, H. a. Richard, and H. J. Maier, “On the mechanical behaviour of titanium alloy TiAl6V4 manufactured by selective laser melting: Fatigue resistance and crack growth performance,” *Int. J. Fatigue*, vol. 48, pp. 300–307, Mar. 2013.

[6] B. Van Hooreweder, D. Moens, R. Boonen, J.-P. Kruth, and P. Sas, “Analysis of Fracture Toughness and Crack Propagation of Ti6Al4V Produced by Selective Laser Melting,” *Adv. Eng. Mater.*, vol. 14, no. 1–2, pp. 92–97, Feb. 2012.

[7] P. Edwards and M. Ramulu, “Fatigue performance evaluation of selective laser melted Ti–6Al–4V,” *Mater. Sci. Eng. A*, vol. 598, pp. 327–337, Mar. 2014.

[8] M. J. Donachie, *Titanium: A Technical Guide*, 2nd Editio. ASM International, 2000.

[9] D. J. De Beer, “Establishment of rapid prototyping / additive manufacturing in South Africa,” *J. South African Inst. Min. Metall.*, vol. 111, no. MARCH, pp. 27–29, 2011.

[10] T. Wohler, “Tooling and Manufacturing State of the Industry Annual Worldwide Progress Report,” *Rapid Prototyp. J.*, 2003.

[11] R. Campbel, D. De Beer, and E. Pei, “Additive Manufacturing in South Africa: Building on the Foundations,” *Rapid Prototyp. J.*, vol. 17, no. 1, pp. 156 – 162, 2011.

[12] M. Peters and C. Leyens, *Titanium and Titanium Alloys*. Wiley-VCH Verlag, 2003.

[13] V. André, R. Henriques, P. Paulo, D. Campos, C. Alberto, A. Cairo, and J. Carlos, “Production of Titanium Alloys for Advanced Aerospace Systems by Powder Metallurgy,” *Mater. Res.*, vol. 8, no. 4, pp. 443–446, 2005.

[14] R. Henriques, H. Sandim, G. C. Coelho, and C. da Silva, “Microstructural evolution during hot pressing of the blended elemental Ti-6% Al-7% alloy,” vol. 347, pp. 315–324, 2003.

[15] G. Lütjering, J. . Williams, and A. Gysler, “MICROSTRUCTURE AND MECHANICAL PROPERTIES OF TITANIUM ALLOYS,” *Microstruct. Prop. Mater.*, vol. 2, pp. 1–74, 2000.

[16] Arcam, “Ti6Al4V Titanium Alloy Ti6Al4V Titanium Alloy.” [Online]. Available: http://www.arcam.com/CommonResources/Files/www.arcam.com/Documents/EBM Materials/Arcam-Ti6Al4V-Titanium-Alloy.pdf. [Accessed: 14-Sep-2014].

[17] G. Lutjering and J. Williams, *Titanium*, 2nd ed. Springer US, 2007, pp. 203–250.

[18] H. J. Rack and J. I. Qazi, “Titanium alloys for biomedical applications,” *Mater. Sci. Eng. C*, vol. 26, no. 8, pp. 1269–1277, Sep. 2006.

[19] J. S. Tiley, “Modeling of Microstructure Property Relationship in Ti-6Al-4V,” PhD Thesis, The Ohio State University, 2002.

[20] B. Gaspar, “Microstructural Characterization of Ti-6Al-4V and its Relationship to Sample Geometry,” U.G Thesis, Deptartment of Material Engineering., California Polytechnic State University., California, USA, 2012.

[21] M. Benedetti and V. Fontanari, “THE ROLE OF BI-MODAL AND LAMELLAR MICROSTRUCTURES OF Ti-6Al-4V ON THE BEHAVIOR OF FATIGUE CRACKS EMANATING FROM EDGE-NOTCHES,” *Eur. Struct. Integr. Soc.*, vol. ECF15.

[22] L. E. Murr, S. a Quinones, S. M. Gaytan, M. I. Lopez, a Rodela, E. Y. Martinez, D. H. Hernandez, E. Martinez, F. Medina, and R. B. Wicker, “Microstructure and mechanical behavior of Ti-6Al-4V produced by rapid-layer manufacturing, for biomedical applications.,” *J. Mech. Behav. Biomed. Mater.*, vol. 2, no. 1, pp. 20–32, Jan. 2009.

[23] CustomPartNet, “Investment Casting,” 2009. [Online]. Available: http://www.custompartnet.com/wu/investment-casting. [Accessed: 02-Nov-2014].

[24] E. C. Santos, M. Shiomi, K. Osakada, and T. Laoui, “Rapid manufacturing of metal components by laser forming,” *Int. J. Mach. Tools Manuf.*, vol. 46, no. 12–13, pp. 1459–1468, Oct. 2006.

[25] C. Achillas, D. Aidonis, E. Iakovou, M. Thymianidis, and D. Tzetzis, “A methodological framework for the inclusion of modern additive manufacturing into the production portfolio of a focused factory,” *J. Manuf. Syst.*, Aug. 2014.

[26] J.-P. Kruth, P. Mercelis, J. Van Vaerenbergh, L. Froyen, and M. Rombouts, “Binding mechanisms in selective laser sintering and selective laser melting,” *Rapid Prototyp. J.*, vol. 11, no. 1, pp. 26–36, 2005.

[27] P. 3D Printers, “Selective Laser Melting,” 2013. [Online]. Available: http://www.popular3dprinters.com/selective-laser-melting-slm/. [Accessed: 03-Sep-2014].

[28] D. L. Bourell, J. J. Beaman, M. C. Leu, and D. W. Rosen, “A Brief History of Additive Manufacturing and the 2009 Roadmap for Additive Manufacturing : Looking Back and Looking Ahead,” 2009.

[29] J. J. Beaman, “Solid Freeform Fabrication : An Historical Perspective,” *12th, Solid Free. Fabr. Symp.*, pp. 584–595, 2001.

[30] J. Blanther, “Manufacture of contour relief-maps,” US Patent #473,901,1892.

[31] E. . Zang, “Vitavue Relief Model Technique,” US Patent #3,137,080,1964.

[32] T. Gaskin, “Earth Science Teaching Device,” US PATENT #3,751,827,1973.

[33] K. Matsubara, “Molding Method of Casting Using Photocurable Substance,” Japenese Kokai Patent Application, Sho 51 [1976]-108131974.

[34] D. Bourell, “Additive Manufacturing History , Current Applications and Where We are Headed,” *SIMTech Annu. Manuf. Forum 2013 next 20 years beyond*, no. October, pp. 5–6, 2013.

[35] P. DiMatteo, “Method of Generating and Constructing Three-Dimensional Bodies,” US Patent #3,932,923,1976.

[36] J. J. Beaman, J. Barlow, D. Bourell, R. Crawford, H. Marcus, and K. McAlea, *Solid Freeform Fabrication: A New Direction in Manufacturing*. Boston: Kluwer Academic Publishers, 1997, pp. 7–9.

[37] C. Baese, “Photographic Process for the Reproduction of Plastic Objects,” US Patent #774,549,1904.

[38] O. Munz, “Photo-Glyph Recording,” US Patent #2,775,758,1956.

[39] W. Swainson, “Method, Medium and Apparatus for Producing Three-Dimensional Figure Product,” US Patent #4,041,476,1977.

[40] P. Ciraud, “Process and Device for Manufacture of any Objects Desired from any Meltable Material,” FRG Disclosure Publication 2263777 ,1972.

[41] R. Housholder, “Molding Process,” US Patent #4,247,508,1981.

[42] H. Kodama, “Automatic method for fabricating a three-dimensional plastic model with photo-hardening polymer,” *Rev. Sci. Instrum.*, vol. 52, no. 11, pp. 1770–1773, 1981.

[43] M. Shellabear and O. Nyrhilä, “DMLS – DEVELOPMENT HISTORY AND STATE OF THE ART,” *4th Laser Assist. Net Shape Eng.*, vol. 1, pp. 393 – 404, 2004.

[44] C. Hull, “Method and apparatus for production of three-dimensional objects by stereolithography,” US Patent # 4,575,330,1986.

[45] C. Deckard, “Method and apparatus for producing parts by selective sintering,” US Patent #4,863,538,1989.

[46] J. Ramos-grez, J. Sanz-guerrero, T. Larraín, and A. Ramírez, “Direct Metal Laser Fabrication of Cu slabs from powder precursor : surface depth of melt and furnace temperature issues,” *Solid Free. Fabr. Proc.*, pp. 246–260, 2006.

[47] J. Yang, H. Ouyang, and Y. Wang, “Direct metal laser fabrication: machine development and experimental work,” *Int. J. Adv. Manuf. Technol.*, vol. 46, no. 9–12, pp. 1133–1143, 2010.

[48] L. S. Bertol, W. K. Júnior, F. P. Da Silva, and C. Aumund-Kopp, “Medical design: Direct metal laser sintering of Ti–6Al–4V,” *Mater. Des.*, vol. 31, no. 8, pp. 3982–3988, Sep. 2010.

[49] L. MNN HOLDING COMPANY, “TreeHugger,” 2014. [Online]. Available: http://www.treehugger.com/sustainable-fashion/3d-printing-your-party-shoes-hit-or-miss.html.

[50] H. Burger, “Seeing South Africa through a manufacturing LENS,” 2013. [Online]. Available: http://www.csir.co.za/lasers/docs/43_pdfsam_Sciencescope Vol 6 No 2 April 2012_3.pdf.

[51] D. Hu, H. Mei, G. Tao, and R. Kovacevic, “CLOSED LOOP CONTROL OF 3D LASER CLADDING BASED ON INFRARED SENSING,” *Solid Free. Fabr. Symp.*, pp. 129–137, 2001.

[52] L. T. LTD, “Laser Metal Deposition,” 2014. [Online]. Available: http://www.lpwtechnology.com/technical-information/laser-metal-deposition/.

[53] J.-P. Kruth, G. Levy, F. Klocke, and T. H. C. Childs, “Consolidation phenomena in laser and powder-bed based layered manufacturing,” *CIRP Ann. - Manuf. Technol.*, vol. 56, no. 2, pp. 730–759, Jan. 2007.

[54] D. Gu and Y. Shen, “Balling phenomena in direct laser sintering of stainless steel powder: Metallurgical mechanisms and control methods,” *Mater. Des.*, vol. 30, no. 8, pp. 2903–2910, Sep. 2009.

[55] SLM Solutions, “Securities prospectus,” 2014. [Online]. Available: http://www.stage.slm-solutions.com/download.php?f=3e833e0c5635e30d7b57457f39194372. [Accessed: 30-Sep-2014].

[56] R. Noe, “Productions Methods,” *Core 77*, 2014. [Online]. Available: http://www.core77.com/blog/materials/production_methods_whats_the_difference_between_selective_laser_sintering_direct_metal_laser_sintering_laser_melting_and_lasercusing_26457.asp. [Accessed: 02-Nov-2014].

[57] Concept Laser, “LaserCusing,” *Concept Laser*. [Online]. Available: http://www.concept-laser.de/en/technology/lasercusingr.html. [Accessed: 02-Nov-2014].

[58] L. Thijs, F. Verhaeghe, T. Craeghs, J. Van Humbeeck, and J.-P. Kruth, “A study of the microstructural evolution during selective laser melting of Ti–6Al–4V,” *Acta Mater.*, vol. 58, no. 9, pp. 3303–3312, May 2010.

[59] L. Facchini, E. Magalini, P. Robotti, A. Molinari, S. Höges, and K. Wissenbach, “Ductility of a Ti-6Al-4V alloy produced by selective laser melting of prealloyed powders,” *Rapid Prototyp. J.*, vol. 16, no. 6, pp. 450–459, 2010.

[60] B. Vrancken, L. Thijs, J. Kruth, and J. Van Humbeeck, “Heat treatment of Ti6Al4V produced by Selective Laser Melting : Microstructure and mechanical properties,” *J. Alloys Compd.*, vol. 541, pp. 177–185, 2012.

[61] P. Mercelis and J.-P. Kruth, “Residual stresses in selective laser sintering and selective laser melting,” *Rapid Prototyp. J.*, vol. 12, no. 5, pp. 254–265, 2006.

[62] M. Shiomil, T. Yamashital, and E. Materials, “Residual Stress within Metallic Model Made by Selective Laser Melting Process,” *CIRP Ann. - Manuf. Technol.*, vol. 53, no. 1, pp. 195–195, 2004.

[63] D. Roylance, “Introduction to Fracture Mechanics,” Class Lecture, Department of Material Science and Engineering., Massachusetts Institute of Technology., Cambridge, USA, 2001.

[64] B. Karihaloo and Q. Z. Xiao, “Linear and Nonlinear Fracture Mechanics,” *Compr. Struct. Integr.*, vol. 2, pp. 81–212, 2003.

[65] T. L. Anderson, *Fracture Mechanics: Fundamentals and Applications*, Third Edit. CRC Taylor & Francis Group, 2004.

[66] A. Liu, “Summary of Stress-Intensity Factors,” Class Lecture, Department of Mechanical Engineering, University of Colorado., Colorado, USA, 2004.

[67] D. Broek, *The Practical Use Of Fracture Mechanics*, First Edit. Dordrecht: Kluwer Academic Publishers, 1988, pp. 23–27.

[68] ASM International, “Fatigue,” *Elem. Metall. Eng. Alloy.*, pp. 244–264, 2008.

[69] Z. Suo, “Fracture Mechanics Lecture Notes: ES 247 Fracture Mechanics,” 1998.

[70] R. Ritchie, D. Davidson, B. Boyce, J. Campbell, and O. Roder, “High-cycle fatigue of Ti-6Al-4V,” *Fatigue Fract. Eng. Mater. Struct.*, vol. 22, no. 7, pp. 621–631, Jul. 1999.

[71] D. Roylance, “Fatigue,” Lecture notes., Department of Materials Science and Engineering., Massachusetts Institute of Technology., Cambridge, USA, 2001.

[72] G. E. Totten, “SPOTLIGHT FATIGUE CRACK,” *Adv. Mater. Process.*, no. May, pp. 39–41, 2008.

[73] NDT Resource Centre, “Fatigue Crack Initiation.” [Online]. Available: https://www.nde-ed.org/EducationResources/CommunityCollege/Materials/Structure/fatigue.htm. [Accessed: 01-Nov-2014].

[74] A. Ekberg, “Fatigue crack propagation,” Lecture notes., Department of Solid Mechanics., Chalmers University of Technology., Gothenburg, Sweden, 2004.

[75] A. Fatemi, “FUNDAMENTALS OF LEFM AND APPLICATIONS TO FATIGUE CRACK GROWTH,” Class Lecture., Department of Mechanical, Industrial and Manufacturing Engineering., University of Toledo., Ohio, USA, 2006.

[76] O. E. Solutions, “Fatigue/Fracture Mechanics,” *brandblocks*. [Online]. Available: http://www.origen.co.za/fatigueFractureMechanics.html. [Accessed: 11-May-2014].

[77] R. Tait, “Fatigue/Fracture Mechanics,” Class Lecture., Department of Mechanical Engineering., University of Cape Town., Cape Town, South Africa.

[78] ASTM International, “ASTM E647-13a Standard Test Method for Measurement of Fatigue Crack Growth Rates 1,” pp. 1–50, 2013.

[79] ASTM International, “E399-12 Standard Test Method for Linear-Elastic Plane-Strain Fracture Toughness K Ic of,” pp. 1–33, 2012.

[80] ASTM International, “ASTM F2921 - 11 StandardTerminology for Additive Manufacturing — Coordinate Systems and Test,” pp. 1–13, 2014.

[81] D. Sher, “Fraunhofer-slm-machine,” 2014. [Online]. Available: http://3dprintingindustry.com/2014/12/01/fraunhofer-slm-machine/. [Accessed: 27-Mar-2015].

[82] EOS GmbH, “Technical data for the EOS Gmbh M270 Direct Metal Laser Sintering machine.” Electro Optical Systems.

[83] EOS GmbH, “Material data sheet EOS Titanium Ti64 for EOSINT M 270 Systems (Titanium Version),” vol. 49, no. 0, pp. 1–3.

[84] R. Tait, “Tiny tots guide to the operation of the E.S.H universal servo hydraulic testing fascility,” Operation manual., Department of Mechanical Engineering., University of Cape Town., Cape Town, South Africa.

[85] T. Udomphol, “Titanium and Titanium alloys,” Lecture notes., Department of Metallurgy and Materials., Suranaree University of Technology., Nakhon Ratchasima, Thailand, 2007.

[86] J. Kruth, M. Badrossamay, E. Yasa, J. Deckers, L. Thijs, and J. Van Humbeeck, “Part and material properties in selective laser melting of metals,” *Proc. 16th Int. Symp. Electromachining*, 2010.

[87] H. Gu, H. Gong, D. Pal, K. Rafir, T. Starr, and B. Strucker, “Influence of Energy Density on Porsity and Microstructure of Selective Laser Melted 17-4PH Stainless Steel,” *Int. Solid Free. Fabr. Symp.*, pp. 474–489, 2013.

[88] N. Moscovitch, G. Gertsberg, N. Nagar, M. Lautzker, N. Fantetti, and B. Bronfin, “The Effect of Porosity on the Microstructure and Mechanical Properties of Die Cast Mg Alloys,” pp. 1–6, Apr. 2006.

[89] B. Vrancken, V. Cain, R. Knutsen, and J. Van Humbeeck, “Residual stress via the contour method in compact tension specimens produced via selective laser melting,” *Scr. Mater.*, vol. 87, pp. 29–32, Sep. 2014.

[90] B. Vrancken, R. Wauthle, J.-P. Kruth, and J. Van Humbeeck, “STUDY OF THE INFLUENCE OF MATERIAL PROPERTIES ON RESIDUAL STRESS IN SELECTIVE LASER MELTING,” *Proc. solid Free. Fabr. Symp.*, p. 393, 2013.

[91] M. Simonelli, “Microstructure evolution and mechanical properties of selective laser melted Ti-6Al-4V,” Ph.D dissertation., Department of Materials., Loughborough University., Leicestershire, UK, 2014.

[92] R. O. Ritchie, “Thresholds for high-cycle fatigue in a turbine engine Ti – 6Al – 4V alloy,” *Int. J. Fatigue*, vol. 21, no. 1999, pp. 653–662, 1999.

[93] G. Piotrowski, X. Deng, and N. Chawla, “Fatigue crack growth of Fe-0.85Mo-2Ni-0.6C steels with a heterogenous microstructure,” *Int. J. Powder Metall.*, vol. 41, pp. 31–41, 2004.

[94] N. McCormick and J. Lord, “Digital Image Correlation,” *Mater. Today*, vol. 13, no. 12, pp. 52–54, 2010.

[95] A. T. Zehnder, *Fracture Mechanics*, 1st ed. Springer Netherlands, 2012, pp. 1–226.

[96] P. Sztefek, M. Vanleene, R. Olsson, R. Collincon, A. . Pitsillides, and S. Shefelbine, “Using digital image correlation to determine bone surface strains during loading and after adaptation of the mouse tibia,” *J. Biomech.*, vol. 43, no. 4, pp. 599–605, 2010.

[97] G. Catalanotti, P. Camanho, P, J. Xavier, G. Davila, C, and T. Marques, A, “Measurement of resistance curves in the longitudinal failure of composites using digital image correlation,” *Compos. Sci. Technol.*, vol. 70, no. 13, pp. 1986–1993, 2010.

[98] H. J. K. Lemmen and R. C. Alderliesten, “The power of Digital Image Correlation for detailed elastic-plastic strain measurements,” *EMESEG*, pp. 73–89, 2008.

Appendix A - Drawings

Fatigue crack growth rate CT specimen

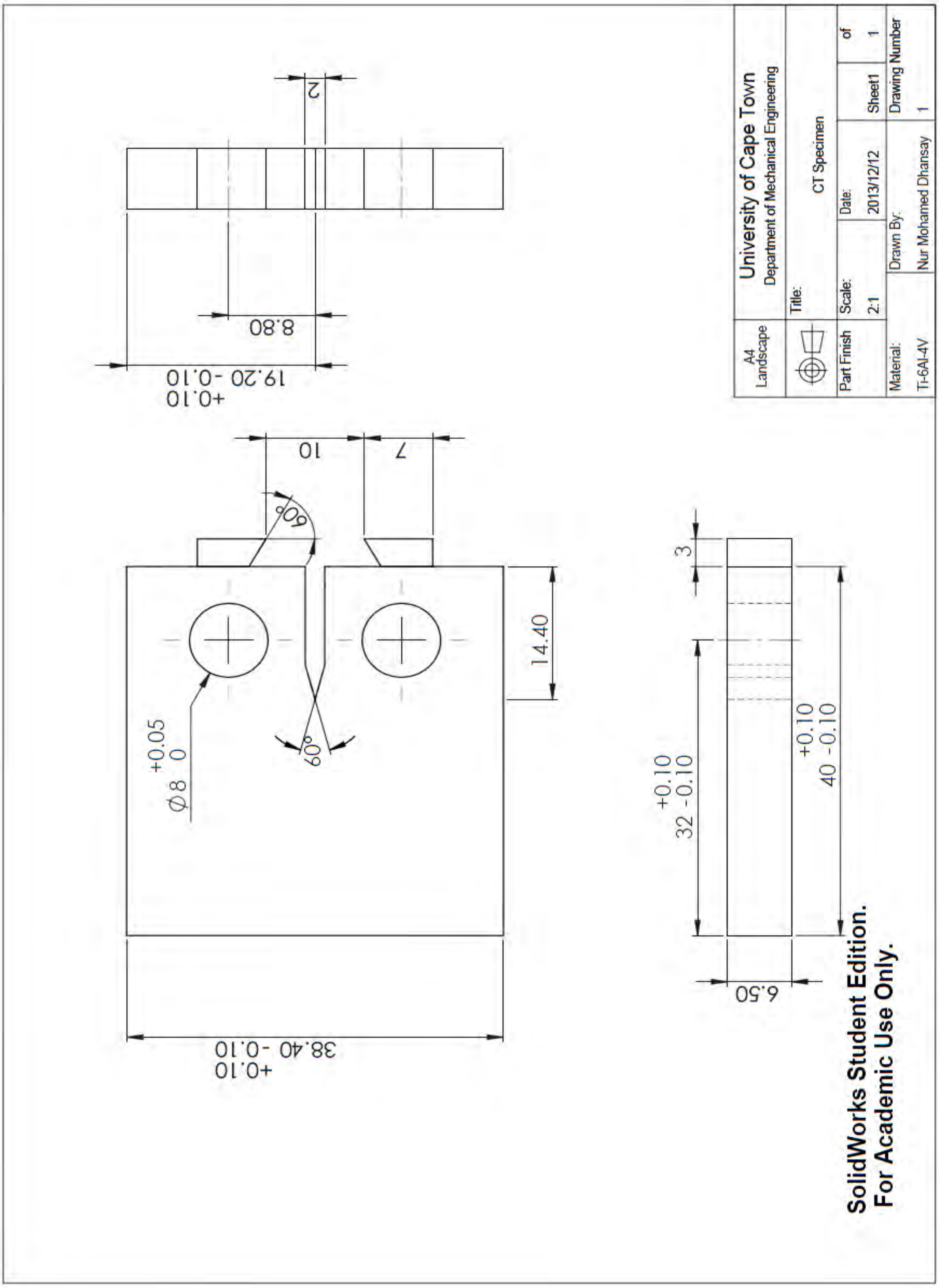

Fracture Toughness CT specimen

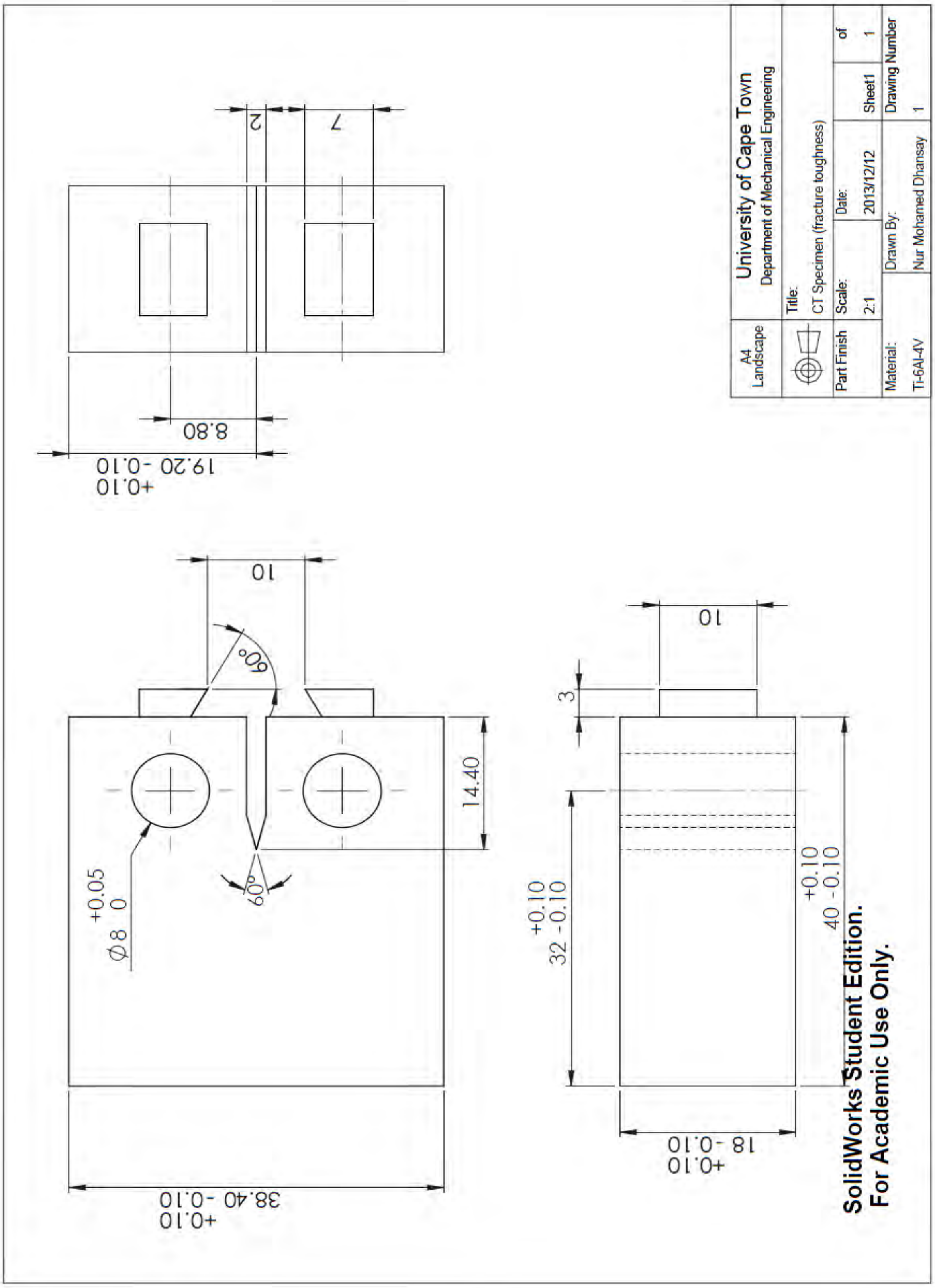
University of Cape Town
Department of Mechanical Engineering
A4 Landscape
Title:
CT Specimen (fracture toughness)
Part Finish
Scale:
2:1
Date:
2013/12/12
Sheet1
of
1
Material:
Ti-6Al-4V
Drawn By:
Nur Mohamed Dhansay
Drawing Number
1
2
7
8.80
19.20 -0.10 +0.10
10
60°
14.40
+0.05 Ø8 0
60°
38.40 -0.10 +0.10
3
10
+0.10 32 -0.10
+0.10 40 -0.10
18 -0.10 +0.10
SolidWorks Student Edition.
For Academic Use Only.

Appendix B – Fracture Surfaces

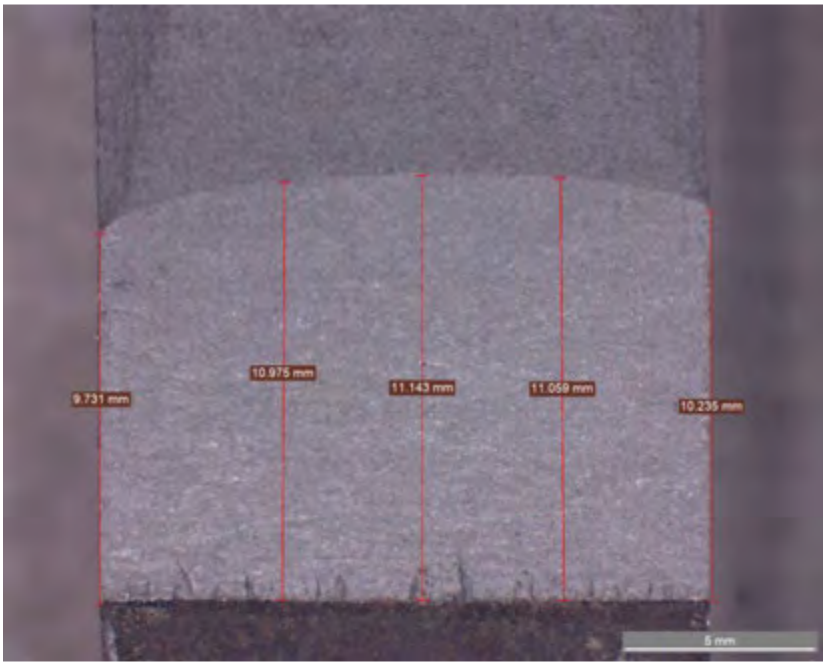

Figure 8-1: Crack length measurement of fracture surface of specimen FLAT – 1

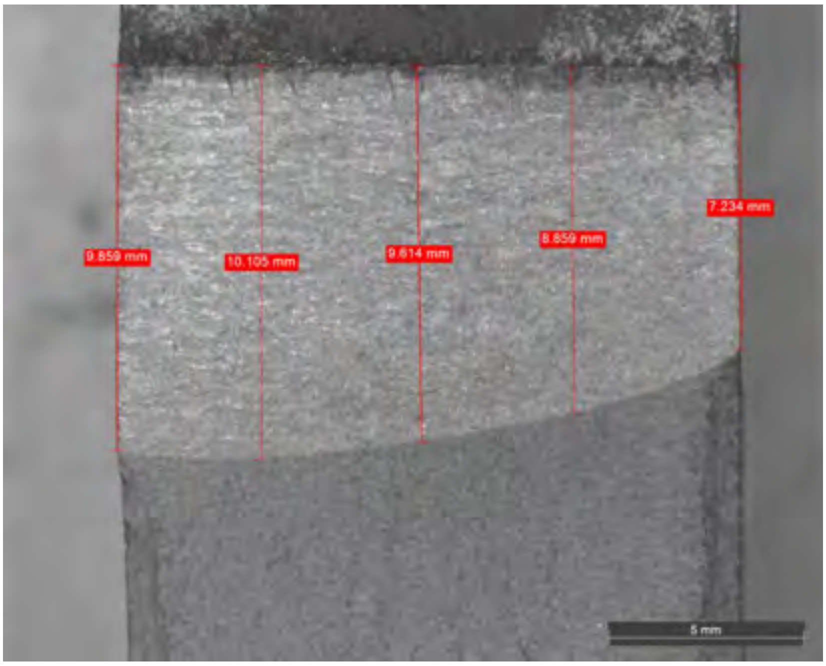

Figure 8-2: Crack length measurement of fracture surface of specimen FLAT – 3

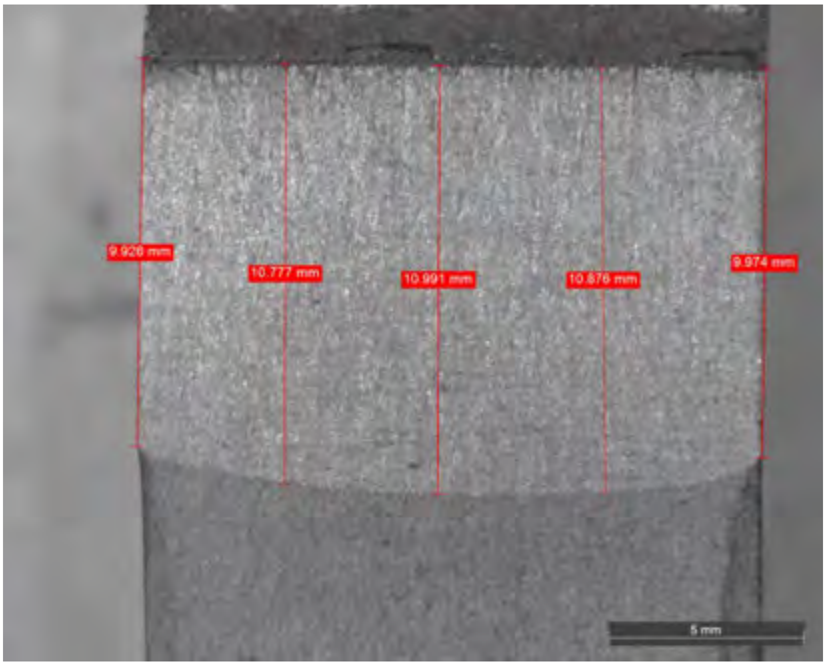

Figure 8-3: Crack length measurement of fracture surface of specimen VERTICAL – 1.

Figure 8-4: Crack length measurement of fracture surface of specimen VERTICAL – 2.

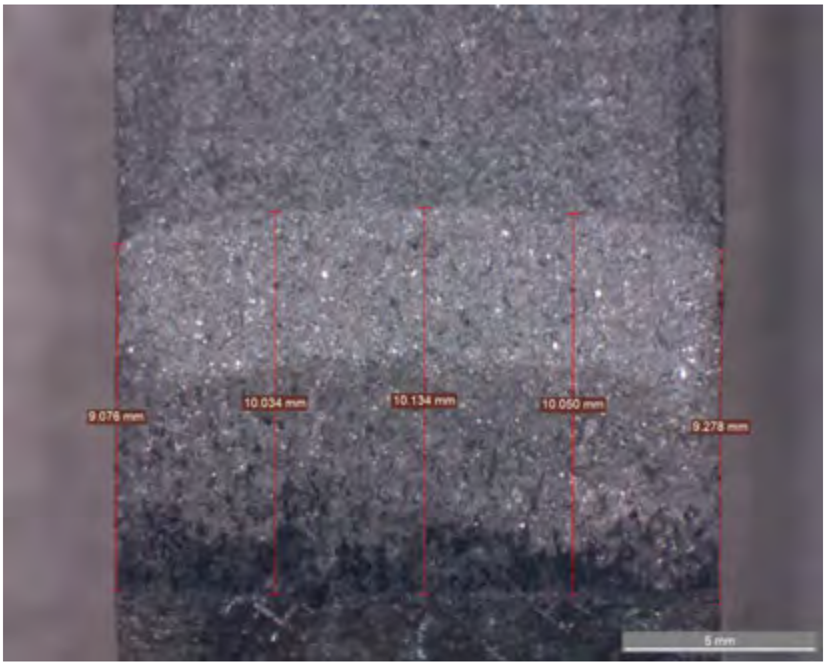

Figure 8-5: Crack length measurement of fracture surface of specimen EDGE – 1.

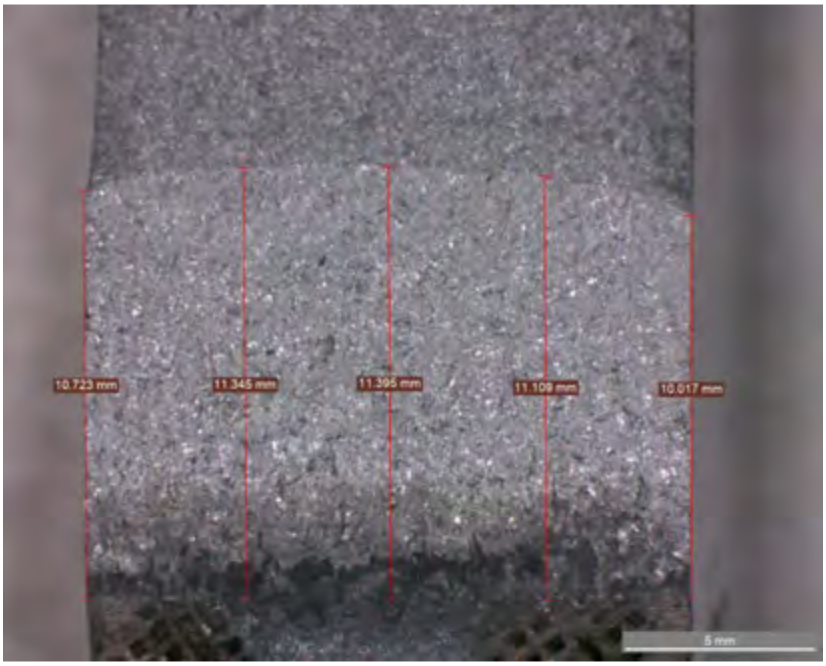

Figure 8-6: Crack length measurement of fracture surface of specimen EDGE – 2.

Appendix C – Raw Fatigue Crack Growth Rate Data

Table 8-1: Raw fatigue crack growth rate data of FLAT specimens

FLAT – 1		FLAT – 2		FLAT – 3		FLAT – 4	
ΔK	**da/dN**	**ΔK**	**da/dN**	**ΔK**	**da/dN**	**ΔK**	**da/dN**
22.21527	1.75E-07	20.5499	1.63E-07	22.11803	1.75E-07	20.73663	1.37E-07
22.90863	2.25E-07	20.89893	1.88E-07	22.66638	2.75E-07	21.05308	1.75E-07
23.64008	2.25E-07	21.37873	2.5E-07	23.28935	2E-07	21.35461	1.63E-07
24.67899	3E-07	21.72457	1.75E-07	23.77384	2.25E-07	21.6395	1.5E-07
25.70017	2.75E-07	22.1301	2E-07	24.27351	2.25E-07	22.0529	2.12E-07
26.79249	2.75E-07	22.54689	2E-07	24.84706	2.5E-07	22.65852	1.62E-07
28.8628	4.75E-07	23.09521	2.55E-07	25.56194	3E-07	23.42607	2.25E-07
30.55193	5.83E-07	23.65201	2.5E-07	26.18105	2.5E-07	24.84281	3.5E-07
31.58506	5E-07	24.17027	2.25E-07	27.01979	3.25E-07	25.47438	2.62E-07
33.81148	8E-07	24.76629	2.5E-07	27.9694	3.5E-07	26.13005	2.62E-07
36.1084	7.5E-07	25.70319	3.75E-07	29.19402	4.25E-07	27.11366	3.75E-07
37.93267	1.1E-06	27.11125	3.25E-07	30.26836	3.5E-07	28.33386	4.37E-07
38.6271	9.35E-07	28.08367	3.38E-07	32.44666	6.5E-07	29.72203	4.62E-07
39.88387	1.27E-06	30.00542	7.75E-07	34.41069	7E-07	31.39865	5.13E-07
42.76361	2.42E-06	31.65818	9.5E-07	36.59398	7E-07	33.7714	6.5E-07
		33.73196	6.75E-07	38.8523	9.75E-07	38.34438	1.05E-06
		35.49378	8.25E-07	42.06257	1.23E-06	50.79449	2.86E-06
		38.49468	1.25E-06	44.26548	1.5E-06		
		42.41966	1.4E-06	48.40518	2.5E-06		
		47.06706	2.8E-06	50.43534	2.75E-06		
				53.01814	3.25E-06		
				56.72381	4.25E-06		

Table 8-2: Raw fatigue crack growth rate data of VERTICAL specimens

VERTICAL – 1		VERTICAL – 2		VERTICAL – 3		VERTICAL – 4	
ΔK	da/dN	ΔK	da/dN	ΔK	da/dN	ΔK	da/dN
16.36777	3.23E-08	18.18067	6.67E-08	16.06962	4.06E-08	20.7645	1.25E-07
17.29958	3.33E-08	18.55779	1.13E-07	18.02609	4.09E-08	21.23456	1.25E-07
17.44341	3E-08	18.8598	5.83E-08	18.5543	6.25E-08	22.88826	1.67E-07
17.93793	4.39E-08	19.39546	1.13E-07	18.89277	6.66E-08	23.69006	2.42E-07
19.20121	5.42E-08	19.71858	8.75E-08	19.21937	9.38E-08	24.20871	2.25E-07
19.51967	6.87E-08	19.90682	1E-07	20.15851	9E-08	24.86554	2.75E-07
19.69735	3.75E-08	20.4877	2E-07	20.44653	1E-07	25.61251	3E-07
19.99994	4E-08	20.7371	1.25E-07	20.64195	1E-07	26.7296	4.25E-07
20.15436	4.17E-08	20.99098	1.25E-07	20.8651	1.13E-07	27.4219	2.5E-07
20.46964	5E-08	21.51265	1.5E-07	21.19373	1.63E-07	28.58982	4E-07
20.63059	4.17E-08	21.88934	1.75E-07	21.55621	1.75E-07	30.92519	4.75E-07
20.99272	8.75E-08	22.10903	1E-07	22.03579	2.25E-07	32.82681	7E-07
21.22911	8.75E-08	22.67307	2.5E-07	22.254	1E-07	35.2653	8E-07
21.57511	5E-08	23.19979	2.25E-07	22.78531	2.37E-07	37.55526	0.000001
21.78754	7.5E-08	23.99509	2.13E-07	23.21834	1.88E-07	39.5851	8E-07
22.0037	7.5E-08	24.57153	2.25E-07	23.75473	2.25E-07	41.09579	1.1E-06
22.3725	1.25E-07	25.37609	3E-07	24.12303	1.5E-07	43.16899	1.4E-06
22.59905	7.5E-08	26.00878	2.25E-07	24.95254	3.25E-07	45.42781	1.4E-06
23.1436	1.25E-07	27.35792	4.5E-07	25.96821	3.75E-07	49.20754	2.1E-06
23.58775	1.38E-07	28.32646	3.75E-07	26.53812	2.5E-07	53.9639	2.88E-06
24.04688	1.37E-07	29.26864	3.44E-07	27.58772	4.37E-07	59.46815	3.83E-06
24.83217	2.25E-07	30.74231	5E-07	28.58667	3.91E-07	70.1931	6.17E-06
25.85289	2.75E-07	32.99668	6.87E-07	30.09583	5.47E-07		
27.0489	3E-07	35.3129	6.25E-07	31.31092	4.06E-07		
28.00678	2.25E-07	36.71064	5.5E-07	33.14415	7.5E-07		
29.84983	4E-07	39.65634	1.05E-06	35.11742	7.22E-07		
31.49108	3.25E-07	42.1746	1.6E-06	36.78558	8.52E-07		
35.05436	6.25E-07	43.53223	1.33E-06	38.38722	1.52E-06		
37.99244	9E-07	46.36683	2E-06	39.23333	1.5E-06		
41.08994	0.000001	47.14477	1E-06	40.71531	1.25E-06		
43.69051	1.08E-06	49.17843	2.5E-06	42.1305	2.25E-06		
46.84876	1.81E-06	51.12258	2.25E-06	43.45737	2E-06		
48.59593	1.88E-06	53.18106	2.34E-06	44.67461	1.75E-06		
49.92888	1.37E-06	57.40426	4.05E-06	47.08345	1.63E-06		
53.26148	3.25E-06	60.38813	5.29E-06	51.20043	5.38E-06		
54.61418	1.76E-06	64.49533	7.78E-06	55.13564	3.97E-06		
57.29805	3.49E-06	74.22398	1.32E-05	56.88341	4.07E-06		
58.92232	2.86E-06						
60.44526	2.98E-06						

Table 8-3: Raw fatigue crack growth rate data of EDGE specimens

EDGE – 1		EDGE – 3		EDGE – 4	
ΔK	**da/dN**	**ΔK**	**da/dN**	**ΔK**	**da/dN**
20.08668	1.5E-07	18.15748	1.09E-07	18.82389	9.45E-08
20.584	1.42E-07	18.71433	1.27E-07	19.30282	1.3E-07
21.67359	1.36E-07	19.15091	1.38E-07	20.01015	1.89E-07
21.99286	2.22E-07	19.63586	1.87E-07	20.6173	9.1E-08
22.70004	2.05E-07	20.05229	1.25E-07	21.28475	1.12E-07
23.19012	1.66E-07	20.7042	1.7E-07	21.8001	2.09E-07
23.79943	2.87E-07	21.40064	1.92E-07	22.46382	2.06E-07
24.54178	3.04E-07	21.96838	2.71E-07	23.33894	2.06E-07
25.78401	4.21E-07	22.69253	2.1E-07	23.96215	3.01E-07
26.50461	3.02E-07	23.56841	3.32E-07	24.55675	2.2E-07
27.323	4.01E-07	24.16092	2.72E-07	25.17138	1.9E-07
28.32033	4.72E-07	24.98377	3.34E-07	26.97787	2.72E-07
29.37983	4.48E-07	25.84771	4.43E-07	27.68227	2.15E-07
30.27635	3.9E-07	26.75698	4E-07	28.4151	3.73E-07
32.55862	9.51E-07	27.59345	4.96E-07	29.30889	5E-07
33.81218	6.06E-07	28.99366	5.21E-07	30.5253	4.97E-07
35.34906	7.94E-07	29.80617	4.37E-07	31.60262	2.53E-07
36.58192	8.5E-07	30.58413	4.99E-07	33.42123	9.73E-07
39.2802	1.45E-06	31.85426	7.05E-07	34.63232	1.05E-06
42.06617	1.34E-06	32.80475	8.57E-07	35.87351	9.43E-07
44.31035	2.68E-06	34.23549	7.12E-07	37.98292	1.44E-06
45.81794	2.84E-06	36.44377	1.09E-06	40.20168	7.45E-07
46.60448	1.04E-06	38.10697	1.66E-06	42.71287	1.33E-06
50.35111	2.74E-06	40.01773	9.9E-07	45.91868	1.12E-06
53.80772	3.24E-06	41.54589	1.03E-06	49.63648	1.57E-06
		45.76452	2.67E-06	52.46697	2.35E-06
		49.76002	2.43E-06	56.16278	4.17E-06
		52.88548	3.85E-06	66.53799	2.1E-06
		59.77216	3.54E-06		